

ENHANCEMENT OF LIGHT OUT-COUPPLING FROM SOLID STATE LIGHTING  
DEVICES

By

PURUSHOTTAM KUMAR

A DISSERTATION PRESENTED TO THE GRADUATE SCHOOL OF THE  
UNIVERSITY OF FLORIDA IN PARTIAL FULFILLMENT OF THE  
REQUIREMENTS FOR THE DEGREE OF DOCTOR OF PHILOSOPHY

UNIVERSITY OF FLORIDA

2009

© 2009 Purushottam Kumar

## ACKNOWLEDGMENTS

I would like to express my heartiest gratitude to Prof. Rajiv K. Singh for his support and guidance through out my academic pursuit at University of Florida. His encouragements and suggestions made the research more interesting and challenging. His constant focus on application-oriented research and numerous ideas thereof added a new dimension to my theory oriented thinking process. I would like to acknowledge my supervisory committee: Prof. S. J. Pearton, Prof. D. Norton, Prof. Fan Ren and Prof. V. Craciun for serving on my supervisory committee, for their time and suggestions.

Special thanks go to Jennifer for all the help she gave during the last four years. She has been my go-to person for all things, be it ordering supplies, printing posters, doctors, pharmacy, etc. With her 7:30 AM in the office routine, she regularly inspired me to be systematic and regular. If I could come to office at 9:00 AM only a few days in four years speaks of me, since there was no dearth of inspiration with Jennifer around. I would also like to thank the guys at Steamers and Buddha Belly; it was at these places where I had the most fruitful discussions with Dr. Singh on research, academia, industry, economy, politics, etc. I would like to thank all past and present lab mates Dr. Karthik Ramani, Dr. Seung-Young Son, Dr. Feng-Chi Chang, Dr. Sejin Kim, Dr. Arul C. Arjunan, Siddharth Tanawade and would be doctors Jaeseok (the handsome), Sushant, Aniruddh, Taekon and Myoung-Hwan for their help and numerous intellectually stimulating discussions, academic or otherwise.

I am grateful to my former and present roommates and friends in Gainesville for a very enjoyable four years. I was fortunate to have very good and enthusiastic cooks around me, starting with Madhu Bhai, Ashish, Akash, Neetu, Sushant, Toral, and

Aniruddh. I was fortunate to have friends, who despite my habit of saying ‘NO’, never got tired of asking me for a game of pool, tennis, ping-pong, poker and lately monopoly! It’s a privilege to have friends, who would hunt you down to even your lab to celebrate your birthday. I am also grateful to them for coping with my weird and stupid ideas and endless chatter on...well...every topic under the sun but mostly....hmm ...better not say anything more here. I hope I was as valuable to them as they were to me.

This acknowledgment would not be complete without thanking my kids back home, Deepak, Monu, Pinku and Mansi. Asking them of their academic performances always made me aware of my own lacking and drove me to do better. I am grateful to my brother and sister for being very understanding and supportive of my aims. My sister never stops worrying about me; something which she has been doing since I was an infant, a doctoral degree hopefully would change that! I am indebted to my parents and the elders of my family, for their support and blessings and innumerable sacrifices. My academic pursuits have bereft them of my company, among their greatest desire; their blessings were the most important factor leading to the completion of this work.

# TABLE OF CONTENTS

	page
ACKNOWLEDGMENTS .....	3
LIST OF TABLES .....	8
LIST OF FIGURES .....	9
ABSTRACT .....	12
CHAPTER	
1 INTRODUCTION .....	14
Snell's Law .....	14
Total Internal Reflection .....	15
Escape Cone .....	15
Light Extraction Efficiency .....	16
Angular Distribution of Light .....	16
Extraction through Multiple Layers .....	17
Increasing Light Out-coupling .....	19
Increasing the Number of Escape Cones .....	19
Directionality of Photons .....	20
Photon Recycling .....	20
Photon Scattering .....	20
2 LITERATURE REVIEW .....	25
Device Shaping .....	25
Light Scattering .....	26
Surface Roughening: Photon Randomization .....	26
Photonic Crystals .....	30
Other Periodic Patterns .....	32
Patterned Substrates .....	33
External Out-couplers: Microlens .....	35
3 OUTLINE OF RESEARCH .....	43
4 EXPERIMENTAL PROCEDURE .....	45
Ray Tracing Simulations .....	45
Simulation Software .....	45
Device Simulated .....	45
Simulation Parameters .....	46

Microstructure Formation.....	46
Lithography .....	46
Etching.....	46
Chemical Mechanical Polishing.....	48
Out-Coupling Measurements.....	48
Total Out-coupling: Integrating Sphere.....	49
Angular Intensity Measurement.....	49
5 ANALYTICAL TREATMENT OF LIGHT EXTRACTION FROM TEXTURED SURFACES USING CLASSICAL RAY OPTICS.....	54
Introduction.....	54
Analysis of Ray Dynamics .....	55
Ray Incidence in Region I.....	56
Ray Incidence in Region II.....	58
Discussion of Ray Dynamics.....	59
Ray Tracing Simulations .....	60
Summary.....	63
6 ANALYSIS OF LIGHT OUT-COUPLING FROM MICROLENS ARRAY .....	69
Introduction.....	69
Device and Simulation Parameters.....	71
Results and Discussion .....	72
Effect of Microlens contact angle and substrate refractive index .....	72
Angular Distribution of Intensity .....	75
Photon Dynamics.....	77
Effect of Absorption.....	78
Conclusions.....	79
7 TIME DEPENDENT CURVATURE CONTROL USING CHEMICAL MECHANICAL POLISHING.....	83
Introduction.....	83
Experimental Procedure.....	85
Results and Discussion .....	86
Effect of Pressure .....	86
Effect of Pad.....	88
Effect of Time.....	88
Discussion.....	89
Conclusions.....	92
8 MICROLENS ARRAY FABRICATION BY CHEMICAL MECHANICAL POLISHING .....	98
Introduction.....	98
Experimental Procedure.....	100

Results and Discussion .....	101
Conclusions.....	103
9 ENHANCED LIGHT OUT-COUPPLING FROM CONICAL, PYRAMIDAL AND MICROLENS ARRAY.....	107
Introduction.....	107
Simulations .....	108
Experimental Procedure.....	110
Sample Preparation.....	110
Out-Coupling Measurements.....	111
Results and Discussion .....	112
Conclusions.....	114
10 CONCLUSIONS .....	119
LIST OF REFERENCES .....	121
BIOGRAPHICAL SKETCH .....	127

## LIST OF TABLES

<u>Table</u>		<u>Page</u>
1-1	Refractive index, critical angle and solid angle of escape cone of typical LED materials.....	22

## LIST OF FIGURES

<u>Figure</u>		<u>Page</u>
1-1	Total internal reflection when light travels through materials with different optical densities ( $n_2 < n_1$ ).....	23
1-2	Wave-guiding of rays traveling beyond the critical angle.....	23
1-3	Refraction and internal reflection of rays traveling through multiple layers with different optical density ( $n_3 < n_2 < n_1$ ).....	24
2-1	Light emitting diode (LED) chip shaping to increase light out-coupling.....	39
2-2	Photon randomization by surface roughening.....	40
2-3	Types of two-dimensional photonic crystals.....	41
2-4	Other periodic patterns used to enhance light extraction.....	41
2-5	Patterned sapphire substrates for epi-layer growth.....	42
2-6	Microlens as external out-coupler for enhanced light extraction.....	42
4-1	Schematic of the devices simulated in this study.....	51
4-2	Characteristics of red light emitting SunLED XSUG62D LED used for out-coupling measurements.....	51
4-3	Integrating sphere setup for measurement of total out-coupling efficiency.....	52
4-4	Measurement set-up for angular distribution of emission from various substrates.....	53
5-1	Surface texture analyzed by geometrical optics in this work.....	64
5-2	Ray dynamics after 1 <sup>st</sup> reflection from region I.....	64
5-3	Various out-coupling zones in region I.....	65
5-4	Ray dynamics after reflection from region II.....	65
5-5	Various out-coupling zones in region I and II.....	66
5-6	The different regions of out-coupling for surface inclined towards left from the perspective of angular distribution in the substrate layer.....	67
5-7	Substrates with different top surface textures simulated in our study.....	67

5-8	Two dimensional ray tracing simulation on a substrate with prismatic structure on top and an isotropic planar light source.....	68
5-9	Three-dimensional ray tracing simulation on substrates with conical, pyramidal and prismatic structures on top surface.....	68
6-1	Device used for ray tracing simulations.....	80
6-2	Out-coupling efficiency with increase in microlens contact angle for different substrate refractive index.....	80
6-3	Enhancement relative to the substrate mode photons for different refractive index substrates.....	80
6-4	Angular distribution of intensity for a device with 80% back surface reflectance.....	81
6-5	Angular distribution of intensity when the back surface is optically transparent.....	81
6-6	Out-coupling efficiency vs. directionality of photons in the substrate.....	82
6-7	Out-coupling efficiency for hemispherical lens as a function of back absorption different substrate refractive index.....	82
7-1	Atomic force microscopy (AFM) image of the surface before and after chemical mechanical polishing (CMP).....	93
7-2	Surface profile and corresponding radius of curvature after 1 min of CMP using Politex™ pad.....	94
7.3	Surface profile and corresponding radius of curvature after 2 min of CMP using Politex™ pad.....	95
7-4	Surface profile and corresponding radius of curvature after 2 min of CMP using IC1000/Suba IV stacked pad.....	96
7-5	Theoretical steady state curve derived from the contact mechanics model.....	97
8-1	Evolution of a step feature and contact pressure along a step profile with progression of CMP.....	104
8-2	AFM image of features before and after CMP.....	104
8-3	AFM line profile along the center of feature before and after CMP.....	105
8-4	AFM line profile and theoretical circular fit of CMP fabricated microlens. ....	105

8-5	AFM line profile obtained from deflection image of initial feature and feature after CMP.....	105
8-6	Scanning electron microscope (SEM) image of microlens array formed after CMP.....	106
9-1	Simulated out-coupling from conical, pyramidal and microlens array with increase in contact angle and substrate refractive indices.....	115
9-2	Variation in out-coupling with back absorption from conical array.....	115
9-3	Angular intensity distribution from conical and microlens array of contact angle 15° and back absorption of 20%, 40% and 100%.....	116
9-4	Measured out-coupling from planar, conical and microlens array with increase in LED drive current.....	116
9-5	Summary of measured out-coupling enhancement from different substrates.....	117
9-6	Measured angular intensity distribution from different reflective substrates normalized to maximum intensity from a bare LED.....	117
9-7	Comparison of measured angular intensity distribution of reflective and absorbing substrates. ....	118
9-8	Ratio of angular intensity of reflective and absorbing substrates along with the simulation curve for a device with structures of contact angle 15° and 40% back absorption.....	118

Abstract of Dissertation Presented to the Graduate School  
of the University of Florida in Partial Fulfillment of the  
Requirements for the Degree of Doctor of Philosophy

ENHANCEMENT OF LIGHT OUT-COUPLING FROM SOLID STATE LIGHTING  
DEVICES

By

Purushottam Kumar

May 2009

Chair: Rajiv K. Singh

Major: Materials Science and Engineering

External efficiency of LEDs, OLEDs and other thin film light emitting devices is limited primarily by the out-coupling/extraction efficiency of the device. Large difference in the optical density of active material and surrounding media gives rise to total internal reflection and wave-guiding, which leads to absorption of a large portion of generated photons. This work studies the application of periodic surface textures e.g. microlens, conical and pyramidal arrays on the surface of these devices to reduce wave-guiding, thereby increasing efficiency. A two-dimensional geometrical analysis of changes in ray dynamics in the presence of periodically inclined topography instead of a planar surface was carried out. The ray dynamics of inclined wall structures enhances the probability of out-coupling after every reflection, making it a better alternative to surface roughening which completely relies on photon randomization. Surface inclination of  $45^\circ$  leads to wave guiding, where as for two-dimensional conical or pyramidal structures maximum out-coupling would be achieved with an inclination  $\sim 50^\circ$ . Ray dynamics in the presence of microlens, conical and pyramidal arrays was also studied using ray tracing simulations. The efficacy of these structures with different aspect ratios, the effect of absorption and

substrate refractive index was studied. Microlens arrays enhance efficiency both by extracting rays lying outside the escape cone and also by redirecting a portion within the escape cone at subsequent reflection. The number of back reflection required for out-coupling reduced with increase in aspect ratio. The reduced reflection leads to less absorption of rays and hence increased efficiency for hemispherical microlenses.

The formation of these periodic structures particularly microlens arrays has been plagued by the lack of a versatile fabrication method applicable to a wide range of inorganic materials. Most of the surface structures used for light out-coupling have been made from polymeric materials, limiting its efficacy because of its low refractive index. A novel method for formation of curved surfaces using chemical mechanical polishing (CMP) is demonstrated. The phenomenon of edge rounding was investigated for its potential for creation of different topographies. Microlenses with H/D ratio of  $\sim 1/10$  and radius of curvature of  $27.5 \mu\text{m}$  were obtained by CMP of hexagonally arranged  $20 \mu\text{m}$  diameter cone shaped structures, prepared by wet etching of Corning 2496 glass. The surface evolution dynamics during polishing was studied and discussed based on contact mechanical model for CMP.

Light out-coupling measurement from conical and microlens array prepared on glass was studied using illumination from a red LED. Conical array was found to be more effective in light out-coupling than microlens array for similar contact angle. Light extraction was found to increase by 23% and 18% by conical and microlens arrays of contact angle of  $17^\circ$ , respectively. The increase in out-coupling was shown by angular intensity measurement, to come from extraction of rays at higher angles.

## CHAPTER 1 INTRODUCTION

Solid state lighting refers to the technology of generation of white light using semiconductor light emitting diodes (LEDs) and Organic light emitting diodes (OLEDs). These devices have high theoretical efficiency because of direct conversion of electrical power to light with little or no heat generation. It is projected that high efficiency of such sources when used for generation of white light will reduce the electricity requirement for lighting by as much as 33% by 2025.<sup>1</sup> Light output from LEDs, and OLEDs depends on the internal quantum efficiency of the active layers and the light extraction efficiency of the device. Internal quantum efficiency depends on and is limited by material quality, crystallinity, impurity concentrations etc. Internal quantum efficiencies of today's LED and OLED devices are reasonably high. Despite high quantum efficiency, the luminous efficiency of these devices remains poor because of low extraction efficiency of photons out of the device.

The primary reason behind poor light extraction is the large ratio of refractive indices of the active layer and the surrounding media which leads to total internal reflection and wave guiding of a majority of generated photons, as explained below.

### **Snell's Law**

When light travels from one medium to another with a different optical density, it experiences a change in directionality. Light traveling from an optically denser to a lighter media bends away from the surface normal. The bending is given by Snell's law

$$\frac{\sin \theta_1}{\sin \theta_2} = \frac{n_2}{n_1} \quad (1-1)$$

where  $\theta_1$  is the angle of incidence,  $\theta_2$  is the angle of refraction,  $n_1$  and  $n_2$  are the refractive indices of medium 1 and 2 respectively. The bending of light rays is schematically illustrated in Figure 1-1.

### **Total Internal Reflection**

As can be deduced from Equation 1-1, with increase in the angle of incidence in medium 1 there would be a higher increase in angle of refraction. For a particular value of incident angle known as critical angle, the resolved sine value for refraction would be greater than 1, at which point Snell's law cannot be used to calculate the angle of refraction. All rays beyond this incident angle are reflected back in the incident medium. The critical angle for internal reflection is given by

$$\theta_c = \text{Sin}^{-1}\left(\frac{n_2}{n_1}\right) \quad (1-2)$$

The larger the difference in the refractive indices the smaller is the critical angle for total internal reflection. Rays within the critical angle is extracted where as the rest are reflected back into the medium.

### **Escape Cone**

As shown in Figure 1-2, critical angle defines an escape cone in three-dimensions, all rays within this cone are extracted out of the medium where as rest experience total internal reflection. In a planar device, since the angle of incidence never change these rays experience repeated total internal reflection till absorbed in the media. The repeated internal reflection of photons in a medium lead to confinement of rays within the medium, called wave-guiding.

The solid angle subtended by the escape cone is given by

$$\Omega = 2\pi[1 - \cos\theta_c] \quad (1-3)$$

$$= 2\pi \left[ 1 - \sqrt{1 - \left(\frac{n_2}{n_1}\right)^2} \right] \quad (1.4)$$

### **Light Extraction Efficiency**

Assuming an isotropic emission from the active layer of a device, the fraction of solid angle of an escape cone represents the maximum fraction of light that can be out-coupled per escape cone in a planar device. The fraction of light extraction in such a case per escape cone is given by

$$\eta = \frac{1 - \sqrt{1 - \left(\frac{n_2}{n_1}\right)^2}}{2} \quad (1-5)$$

Table 1-1 presents the refractive index, critical angle with air, the solid angle of the corresponding escape cone and the fraction of light extraction of several materials used in LED and OLED devices. The smaller values  $\eta$  show the extent of internal reflection and light entrapment in these optical devices.

### **Angular Distribution of Light**

The refraction of light at the interface of an optically different media changes the angular distribution of intensity. In case of light emitting devices e.g. LEDs, OLEDs, the angular distribution of the generated photons in the active layer is usually isotropic.

Assuming the directional intensity in the active layer as  $I_l$

$$I_1(\theta_1, \varphi) = I_1 = \text{Constant} \quad (1-6)$$

where  $\varphi$  is the azimuthal angle in polar co-ordinate system. If  $I_2(\theta_2)$  is the directional intensity in medium 2, then from energy conservation

$$I_1(\theta_1) \sin \theta_1 \partial \theta_1 \partial \varphi = I_2(\theta_2) \sin \theta_2 \partial \theta_2 \partial \varphi \quad (1-7)$$

$$I_2(\theta_2) = I_1 \frac{\sin \theta_1 \partial \theta_1}{\sin \theta_2 \partial \theta_2} \quad (1-8)$$

Differentiating Snell's law (Equation 1-1) gives

$$\cos \theta_1 \partial \theta_1 = \left( \frac{n_2}{n_1} \right) \cos \theta_2 \partial \theta_2 \quad (1-9)$$

$$\frac{\partial \theta_1}{\partial \theta_2} = \left( \frac{n_2 \cos \theta_2}{n_1 \cos \theta_1} \right) \quad (1-10)$$

Substituting Equation 1-10 in Equation 1-8 yields

$$I_2(\theta_2) = I_1 \left( \frac{n_2}{n_1} \right)^2 \frac{\cos \theta_2}{\cos \theta_1} \quad (1-11)$$

$$I_2(\theta_2) = I_1 \left( \frac{n_2}{n_1} \right)^2 \frac{\cos \theta_2}{\sqrt{1 - \left( \frac{n_2}{n_1} \right)^2 \sin^2 \theta_2}} \quad (1-12)$$

This is the actual angular distribution of light from a planar device, usually approximated to a Lambertian distribution of light given by

$$I_2(\theta_2) = F \cos \theta_2 \quad (1-13)$$

### **Extraction through Multiple Layers**

In most light emitting devices, active layer and substrate have different optical densities. Hence in most cases, photons experience change in refractive index multiple times before final out-coupling. The angular distribution of intensity and the total out-coupling from two layers is solved below using classical ray optics. Figure 1-3 shows schematically the light extraction from three layers of different refractive indices.

Equation 1-12 gives the angular intensity of light in layer 2. Using Equation 1-12 the intensity in layer 3 in terms of angular intensity in layer 2 is given by

$$I_3(\theta_3) = I_2(\theta_2) \frac{\sin \theta_2 \partial \theta_2}{\sin \theta_3 \partial \theta_3} \quad (1-14)$$

Using Snell's law at the interface of layer 2 and 3 gives

$$\frac{\partial \theta_2}{\partial \theta_3} = \left( \frac{n_3 \cos \theta_3}{n_2 \cos \theta_2} \right) \quad (1-15)$$

Substitution of Equation 1-15 and Equation 1-12 in Equation 1-14 gives

$$I_3(\theta_3) = I_1 \left( \frac{n_2}{n_1} \right)^2 \frac{\cos \theta_2}{\sqrt{1 - \left( \frac{n_2}{n_1} \right)^2 \sin^2 \theta_2}} \times \left( \frac{n_3}{n_2} \right)^2 \frac{\cos \theta_3}{\sqrt{1 - \left( \frac{n_3}{n_2} \right)^2 \sin^2 \theta_3}} \quad (1-16)$$

$$I_3(\theta_3) = I_1 \left( \frac{n_3}{n_1} \right)^2 \frac{\cos \theta_2 \cos \theta_3}{\sqrt{1 - \left( \frac{n_2}{n_1} \right)^2 \sin^2 \theta_2} \sqrt{1 - \left( \frac{n_3}{n_2} \right)^2 \sin^2 \theta_3}}$$

(1-17)

Converting  $\theta_2$  to  $\theta_3$

$$I_3(\theta_3) = I_1 \left( \frac{n_3}{n_1} \right)^2 \frac{\cos \theta_3}{\sqrt{1 - \left( \frac{n_3}{n_1} \right)^2 \sin^2 \theta_3}} \quad (1-18)$$

The above equation shows that the angular intensity is dependent only on the optical density of the active layer and the final ambient environment. Angular intensity is independent of the optical density of the intermediate layers and can be approximated to Lambertian distribution even with multiple intermediate layers. Integrating the intensity will give the total out-coupled power

$$P = \int_0^{2\pi} \int_0^{\pi/2} I_3(\theta_3) \sin \theta_3 \partial \theta_3 \partial \varphi \quad (1-19)$$

$$= 2\pi I_1 \left( 1 - \sqrt{1 - \left( \frac{n_3}{n_1} \right)^2} \right) \quad (1-20)$$

The fractional efficiency would be given by

$$\eta = \frac{P}{4\pi I_1} \quad (1-21)$$

$$\eta = \frac{1 - \sqrt{1 - \left(\frac{n_3}{n_1}\right)^2}}{2} \quad (1-22)$$

According to classical ray optics, both the total out-coupling and angular distribution of intensity is independent of the optical density of intermediate layers for a planar device. It can therefore be inferred that there would not be any effect of continuous grading of refractive index on either out-coupling or angular distribution. It should be noted here that the above calculations are totally classical in nature and does not take into account phenomena such as Fresnel reflections, and diffuse scattering of light caused by rough surfaces.

### **Increasing Light Out-coupling**

#### **Increasing the Number of Escape Cones**

Escape cone is defined around a surface perpendicular. All emissions from a point source at the center of a sphere will be emitted out because of the presence of infinite escape cones. This approach is used by hemispherical shaping of LED chips. Shaping of chips has several issues; among them is the requirement of thick layers and issues relating to cost and technology. Today, mostly the packaging epoxy is shaped into a hemisphere to decrease reflection at epoxy-air interface. For a rectangular device, a maximum of six escape cones are present, each for four lateral and two vertical directions. These escape cones can be opened by use of thick transparent substrates or superstrates, use of a back reflector e.g. Bragg reflector, Ag mirror etc. This approach is limited by the LED

material, availability and feasibility of transparent substrates, back reflector, cost associated with growth of thick layers and device design issues.

### **Directionality of Photons**

We know that rays only within the escape cone are out-coupled. Many researchers have tried to manipulate the directionality of photon emission so as to increase the proportion of photons within critical angle. This approach also termed as photon density of state engineering is achieved in resonant cavity LEDs,<sup>2</sup> and surface Plasmon-enhanced LEDs<sup>3</sup>.

### **Photon Recycling**

Photons that are not out-coupled are wave-guided and finally absorbed in the device. The non-emissive absorption is mostly in the substrate and the contact areas. Absorption can also occur in the active area of the device. Photons absorbed in the active layer might be reemitted, in which case will get another opportunity to find an escape cone. This is called photon recycling.<sup>4</sup> Photon recycling depends on the internal quantum efficiency of the device. Multiple recycling can occur in a highly efficient device. Photon recycling is very sensitive to the material quality and non-emissive losses in substrate and contacts. Photon recycling can be increased by use of thick active layer with high quantum efficiency. Internal efficiency however high, is less than 100% and decreases with aging. The absorption in practical LEDs is usually considered non-emissive and therefore thin active layer is used.

### **Photon Scattering**

Scattering reduces wave-guiding by providing multiple chances to photons to escape by changing photon directionality upon every reflection. Photon randomization is

achieved by modification of various interfaces in the device. One of the simplest technique for randomization is surface roughening.<sup>5</sup> Surface roughening also increases the diffuse scattering of photons; the resultant reduction in specular reflection reduces the wave-guiding of photons. Surface roughening has been achieved by techniques like natural lithography,<sup>6</sup> anodization<sup>7</sup> and growth of a rough diamond layer<sup>8</sup>. Various other structures like Bragg gratings,<sup>9</sup> micro-ring,<sup>10</sup> and even photonic crystals<sup>11</sup> have also led to scattering of photons. Escape cone engineering has also been done using external out-couplers like encapsulating dome, anti-reflection coatings, reflectors and array of microlenses<sup>12</sup> and other structures like micro-pyramids,<sup>13</sup> prism,<sup>14</sup> etc.

Chapter 2 presents the literature survey of photon scattering methods used to enhance light extraction from LEDs, OLEDs and thin film Phosphor devices.

Table 1-1. Refractive index, critical angle and solid angle of escape cone of typical LED materials.

Materials	Refractive Index	$\theta_c$ with air	Solid Angle ( $\Omega$ )	Efficiency ( $\eta$ )
Glass/ SiO <sub>2</sub>	1.4-1.5	41.8	1.6	0.13
ITO	1.8-1.9	33.7	1.1	0.09
SiN <sub>x</sub>	1.95	30.9	0.9	0.07
YAG	1.83	33.1	1.0	0.08
Eu:Y <sub>2</sub> O <sub>3</sub>	1.93	31.2	0.9	0.07
ZnS:Mn	2.5	23.6	0.5	0.04
GaN	2.5	23.6	0.5	0.04
SiC	2.8	20.9	0.4	0.03

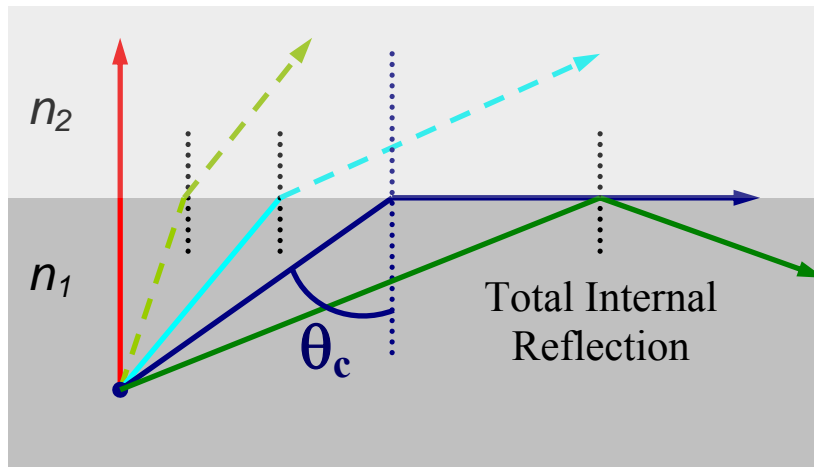


Figure 1-1. Total internal reflection when light travels through materials with different optical densities ( $n_2 < n_1$ ).

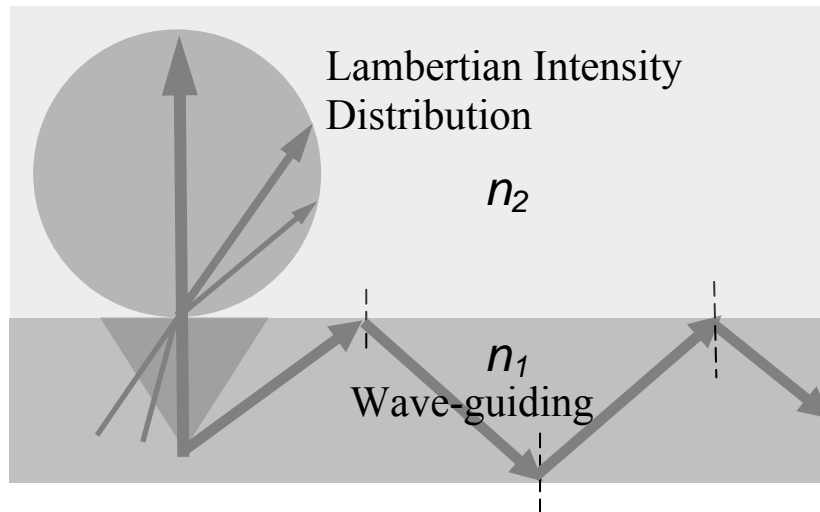


Figure 1-2. Wave-guiding of rays traveling beyond the critical angle. It also shows the angular distribution of light, isotropic in medium 1, and Lambertian in medium 2 upon travel from medium 1 ( $n_2 < n_1$ ).

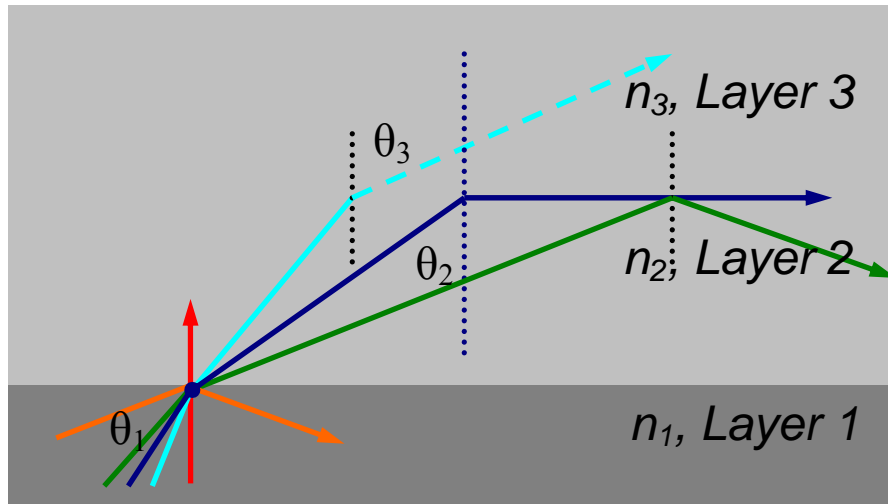


Figure 1-3. Refraction and internal reflection of rays traveling through multiple layers with different optical density ( $n_3 < n_2 < n_1$ ).

## CHAPTER 2 LITERATURE REVIEW

An LED based on primitive design with planar structure and absorbing substrate can have efficiency as low as 4%. Soon after the invention of red LEDs by Holonyak and Bevacqua,<sup>15</sup> this limitation in extraction efficiency because of total internal reflection and wave-guiding was realized. Over the years many techniques has been used to overcome this limitation. The following section describes some of the techniques which relies on light scattering by either device shaping or interface modification for increasing light output.

### **Device Shaping**

Among the earliest effort to increase light output was the shaping of thick GaAs wafer to a hemispherical shape by polishing.<sup>16</sup> Hemispherical shaping was applied to high power infrared AlGaAs LEDs giving an external efficiencies of ~40%.<sup>17,18</sup> Subsequently light extraction from other shapes like truncated sphere, truncated ellipsoid, truncated cone and paraboloid was also studied.<sup>19</sup> Apart from radially symmetric shapes, geometrically deformed (non-rectangular) chips with plane walls also improve efficiency. Rhomboidal and triangular chips with parallel bases were considered by Lee and Song.<sup>20</sup> Non-perpendicular faces leads to change in the incident angle after each internal reflection. All rays in the horizontal plane can escape from such a chip. Rhombohedral and triangular chips when combined with slanted walls can provide escape cone to photons in every direction after multiple internal reflections. Figure 2-1 shows the device shaping using (A) slanted walls and (B) triangular chip to improve efficiency. Recently, some of these slanted walls and triangular chip has been implemented on devices. TiO<sub>2</sub>/SiO<sub>2</sub> omnidirectional reflector was deposited on to a 50° inclined side walls of an

LED.<sup>21</sup> The trapezoidal shaping led to an enhancement of 15% compared to vertical wall LED. Kim et al. fabricated a LED with triangular chip with an angle of 60° and vertical side walls for comparison with a conventional rectangular LED.<sup>22</sup> The triangular geometry increased the efficiency by 48% at 20 mA and 24% at 100 mA input current. As pointed out earlier, triangular geometry with slanted walls would have been more efficient in light extraction. Moreover, Masui et al. through analytical ray tracing found equiangular polygons to increase extraction of only a finite number of rays.<sup>23</sup> In case of triangular chips, isosceles shape with acute angle less than twice the critical angle would provide out-coupling chances to maximum rays.<sup>23</sup> Lee et al. slanted the walls of sapphire substrates by anisotropic chemical wet etching to form an inclination of 60° on the bottom side of substrate of a rectangular chip.<sup>24</sup> The efficiency increased 55% by shaping the substrate. Shaping of chips improves efficiency however, the polishing and shaping of semiconductor chips is a costly and inconvenient technology.

## **Light Scattering**

### **Surface Roughening: Photon Randomization**

Apart from chip shaping techniques for redirection of photons, many photon scattering techniques has been used at various interfaces particularly the top surface of LEDs to enhance efficiency. Photon randomization was first proposed by Bergh and Saul in form of surface roughening to increase emission from LEDs.<sup>25</sup> Rough surface leads to randomization of photons and hence facilitates its escape after multiple reflections. Schnitzer et al. first demonstrated the enhancement in light extraction using surface roughening on an AlGaAs LED reporting an external efficiency of ~30%.<sup>26,27</sup> The idea of chaotization of photon trajectory was employed by randomly nano-texturing surface with

a mirror at the back. The techniques used for nano-texturing/roughening was called natural lithography. The surface was coated with a polystyrene spheres, then etched to form randomly distributed cylindrical pillars.<sup>28</sup> This method is also known as non-resonant cavity LEDs. Lee et al. estimated the increase in efficiency by photon randomization to an extent that compensates approximately for internal losses due to absorption.<sup>29</sup> Windisch et al. studied the effect of surface texturing parameters e.g. the diameter, distribution of polystyrene and the etch depth on the extraction efficiency of AlGaAs LED.<sup>30-34</sup> In the absence of any theory to predict scattering from textured surface it was believed that the efficient structure would have feature size in the order of wavelength of light. Accordingly Windisch et al. studied features with diameter in the range 300-700 nm. The study found the optimized structure to be 300 nm in diameter and 180 nm in depth for a GaAs/AlGaAs LED, however no explanation was given for the observed results.<sup>33</sup> Smaller structures were said to scatter light poorly where as bigger features lead to more specular reflection. Surface texturing was observed to out-couple light from outside the escape cone ( $\theta > \theta_c$ ) though at the expense of some loss in emission of the normal radiations. Presence of a back reflector more than compensates for this loss hence an overall increase in efficiency is observed.

Over the period of time different researchers have applied surface texturing on various LEDs e.g. GaN, InGaN, GaP etc. on different substrates e.g. GaN, SiC, sapphire and used numerous texturing techniques. Huh et al. roughened the surface of GaN by wet etching using rapid thermal anneal (RTA) nucleated Pt as etch mask.<sup>35</sup> Pt mask of 300-500 nm diameter and thickness in the range of 50-100 nm upon wet etching in phosphoric acid formed a surface with RMS roughness of 5-6 nm. This micro-roughened surface

increased the efficiency by 62%. Fujii et al. used photochemical etching in KOH solution to roughen the N-face of GaN surface in an InGaN/GaN LED.<sup>36</sup> Etching resulted in hexagonal cone like features, the dimensions of which were varied by changing the etching time. LEDs with 500 nm features showed an increase in efficiency by almost 100%. Kasugai et al. demonstrated increase in efficiency of GaN based LED grown on SiC substrate by roughening of SiC front surface.<sup>37</sup> Moth eye structure was formed on SiC surface by dry etching using naturally formed Au masks. A 3.8 fold improvement in out-coupling was observed from moth-eye structures of conical shape of height 400 nm and separation 170 nm for radiation of wavelength 478.5 nm. Kim et al. formed nanoporous surface of anodized alumina on GaN surface of InGaN/GaN LED.<sup>38</sup> The nanopores formed by anodization were of diameter  $\sim 30$  nm with a separation of  $\sim 90$  nm. The device in which the nano-pores extended into the GaN layer showed the highest enhancement for emission wavelength of 470 nm. In GaN based LEDs texturing has been done on mostly p-GaN layers. Kim et al. textured n-GaN layer using selective etching by  $H_3PO_4$  at high temperature to form hexagon shaped etch pits.<sup>39</sup> Upon use of a highly reflective Al scheme as n-type electrode, an enhancement of 54% was observed over conventional LED. Hwang et al. developed an electrodeless photo-electrochemical etching for forming nano-porous n-GaP surface.<sup>40</sup> Pores of 300-700 nm in diameter with a density of  $1.2 \times 10^8 \text{ cm}^{-2}$  were created on the surface of an AlInGaP LED which led to an enhancement of 30-50%. Fang et al. enhanced the efficiency of blue LED by photo-enhanced chemical etching of n-GaN surface.<sup>41</sup> The N-face etched using the process formed hexagonal cone pits consistent with the GaN crystal structure. Lee et al. grew ZnO nano rods ( $n = 2$ ) on top of GaN ( $n = 2.5$ ) surface to increase the extraction

efficiency.<sup>42</sup> High refractive index of ZnO along with the rod shape, increased the out-coupling by 60%. Kim et al. fabricated GaN LED on patterned sapphire substrate.<sup>43</sup> One LED had textured ITO layer on top where as other had textured p-GaN on top with smooth ITO layer. The device with textured p-GaN showed an enhancement of 21% compared to 10% for the device with textured ITO over the conventional LED. The layer with highest refractive index ( $n_{\text{GaN}}=2.5$ ,  $n_{\text{ITO}}\sim 1.9$ ) traps most of the light, texturing this layer will led to the highest improvement in efficiency as in the above work. Bao et al. used laser lift off process to pattern the n-GaN layer during separation of sapphire substrate from the GaN layer.<sup>44</sup> The pattern with high roughness had an underlying 4  $\mu\text{m}$  diameter holes with 1  $\mu\text{m}$  separation and a depth of around 100 nm. The roughening increased the efficiency by approximately 100% with the use of an Ag mirror at the back surface. Figure 2-2 shows few roughened surfaces from different LED devices used by different researchers to enhance out-coupling.

In organic LEDs, the low refractive index of glass ( $n\sim 1.5$ ) substrate enables more techniques of light scattering than just surface roughening. Cheng et al. deposited polydimethyl siloxane (PDMS,  $n=1.45$ ) nanowires on to glass substrate which formed micro mesh to out-couple light.<sup>45</sup> An enhancement of 46% was observed using these textured PDMS films. Bathelt et al. used a scattering film made of polymer dispersed in acrylate based resist matrix, on top of glass substrate.<sup>46</sup> Polymer sphere acted as a light scattering center. The efficiency was found to decrease above an optimum number of scattering centers. The efficiency also decreased with both the film thickness and number of polymer micro-spheres. Li et al. used mono-dispersed silica  $\sim 400$  nm and 1000 nm in diameter embedded into polyvinylalcohol on top of glass substrate to enhance

efficiency.<sup>47</sup> 400 nm diameter mono-dispersed silica enhanced efficiency by around 60%. Kim et al. utilized a porous alumina film of different pore diameter prepared by anodizing electrochemical process to enhance efficiency.<sup>48</sup> The optimum pore diameter of 70 nm, enhanced efficiency by 9% over OLED without a porous film.

In LEDs and OLEDs roughening of multiple interfaces is difficult to implement with epilayer and organic film growth requiring planar surface. Moreover, the advantage of multiple interface roughening is not very clear unless there is a mismatch in the optical density at each interface such as for hetero-epitaxy of GaN on sapphire. Multiple interfaces were roughened in an InGaN-GaN flip-chip LED by Lee et al.<sup>49</sup> The roughened interface included both sides of sapphire substrate in addition to the p-GaN layer. GaN epilayer was grown on a patterned sapphire substrate with bump pattern of 3  $\mu\text{m}$  diameter and 3  $\mu\text{m}$  spacing, the top side of sapphire was textured by ICP-RIE etching using naturally formed Ni islands as hard mask and, the p-GaN side had naturally textured surface grown by MOCVD. These triple light scattering surfaces led to an increase in light extraction by ~60% at 350 mA injection current. In thin film phosphor devices, roughening of the substrate prior to phosphor film deposition leads to a high roughness phosphor film and improved extraction efficiency. Cho et al. used a poly-diamond coating to increase the roughness of silicon substrate.<sup>8</sup> Electrochemical etching was also used to achieve different levels of roughness on silicon substrates.<sup>7</sup>

### **Photonic Crystals**

Over the time, researchers have also used more regular/periodic surface structures to out-couple wave-guided modes from the device. The most notable among these is the use of Photonic crystals (PC). Photonic crystals which are periodically patterned different

refractive index materials, effects photons in a way similar to electron in crystals. In photonic crystals, photon modes disappear for certain frequencies and directions where as it increases for others. The periodic variation in refractive index can be done in one, two or three dimensions. Typically 2D photonic crystals are periodic array of parallel cylindrical rods or cylindrical holes in a layer. Numerous studies have shown increase in light out-coupling by use of photonic crystals of different periodicity in various semiconductor LEDs,<sup>50-61</sup> OLEDs<sup>62-64</sup> and thin film phosphor<sup>65-70</sup> devices. Fan et al. predicted an increase of 90% due to elimination of guided modes by use of air holes in the top cladding layer.<sup>50</sup> Boroditsky et al.<sup>51</sup> demonstrated out-coupling enhancement by varying the period of hexagonally arrayed holes where as Baba et al.<sup>52</sup> demonstrated enhancement using 2D array of micro-pillars. Wierer et al. formed hexagonal lattice photonic crystal array by dry etching on top of GaN layer of an InGaN/GaN quantum well LED.<sup>53</sup> They reported a change in angular intensity distribution with variations in lattice constant and hole diameter. Lattice constants in the range 270-340 nm and hole diameter in the range of 200-250 nm were studied. Photonic crystal with lattice constant of 340 nm and hole diameter of 250 nm showed a maximum enhancement of 1.5 times over planar LEDs. The enhancement was reportedly from the effect of PC on guided modes and not because of creation of any photonic band gap or enhancement of spontaneous emission. Figure 2-3 shows both types of photonic crystals (A) cylindrical holes and (B) cylindrical pillars used on device surfaces.

Apart from the efforts to use PCs in the cladding layer to improve the light extraction, PC has also been used in and around the active layer to improve spontaneous emission or reduce guided modes in the active layer. First few attempts using photonic

crystals were with infrared LEDs mostly because of the ease of forming PC in that size range. Boroditsky et al. surrounded a 20  $\mu\text{m}$  wide hexagonal active region with several rows of 2D photonic crystals.<sup>51</sup> Photonic crystals enhanced light extraction by reducing wave-guided mode by coherent scattering of the internally trapped light. 2D photonic crystals with lattice spacing of 900 nm showed 6.5 fold improvement in efficiency of an optically pumped InGaAs/InP LED emitting in infra red wavelength range of 1500-1700 nm. Ryu et al. observed a 30 fold increment by use of 2D photonic crystal in the active layer of an optically pumped InGaAs quantum dots.<sup>54</sup>

Structures similar to photonic crystal but much larger in size has also been used to enhance extraction. Han et al. formed 1D (linear) and 2D (square) patterns on the bottom side of a sapphire substrate in a flip chip LED (emission through sapphire).<sup>55</sup> The patterns had periodic distance of 13  $\mu\text{m}$  for 1D and 17  $\mu\text{m}$  for 2D structures and depth of 0.2-0.4  $\mu\text{m}$ . The efficiency was found to improve with etch depth. A maximum improvement of ~ 40% was observed for 2D structures with a depth of 0.4  $\mu\text{m}$ .

### **Other Periodic Patterns**

Many other regular periodic patterns have been used in LEDs and OLEDs to enhance out-coupling. Baba et al. fabricated 2D arranged high aspect ratio microcolumns of GaInAsP/InP on InP wafers by ICP etching.<sup>52</sup> The micro-columns arranged in honeycomb arrangement had diameter in the range 0.3-2.0  $\mu\text{m}$  and pitch 1.15-7.75  $\mu\text{m}$ . The structure was optically pumped and photoluminescence spectrum measured. The extraction enhancement after taking into account the filling factor was found to be around ten times higher. The enhancement was suggestively not caused by the photonic band gap but by strong diffraction and scattering of lateral modes. Choi et al. hypothesized that a

higher ratio of emission surface area to light-generation area is required to improve efficiency.<sup>10</sup> They formed an array of micro-disk of 20  $\mu\text{m}$  diameter and micro-rings with an external diameter of 20  $\mu\text{m}$  and an internal diameter of 10  $\mu\text{m}$  onto the top surface to increase the emission surface area. The efficiency of micro-ring LED with area ratio 1.8 was found to be 54% higher than that of micro-disk LED with area ratio of 1.4, both being higher than the conventional flat LED. Su et al. used circular Bragg grating along the periphery of a light emitting region to enhance light extraction.<sup>71</sup> Hsu et al. used a 1D array of Au nano-wire 100 nm wide with different periodicity beneath ITO layer in an OLED device to enhance out-coupling.<sup>72</sup> Metallic nano-structures have large scattering cross-section due to localized electromagnetic enhancements.<sup>73</sup> Nano-wire with a periodicity of 450 nm almost doubled the brightness. Apart from increasing the out-coupling, nano-wires with different periodicity also acted as narrow band color filters. Figure 2-4 shows the cylindrical micro pillars and circular Bragg gratings used to improve light out-coupling.

### **Patterned Substrates**

A planar substrate was favored for growth of LEDs because of the need of high quality epitaxial layer. Tadatomo et al. used patterned sapphire with parallel groves of 3  $\mu\text{m}$  diameter and 1.5  $\mu\text{m}$  depth along  $\langle 1\bar{1}00 \rangle$  direction to grow InGaN-GaN multiple quantum well (MQW) LED.<sup>74</sup> The idea was to reduce the density of dislocations by selected area growth and epitaxial layer overgrowth. The dislocation density in the GaN grown on patterned sapphire substrate was found to reduce to  $1.5 \times 10^8 \text{ cm}^{-2}$  compared to  $4 \times 10^8 \text{ cm}^{-2}$  for conventionally grown GaN film. The increase in efficiency of the LED was attributed to the reduced dislocation density. Yamada et al. used a patterned sapphire

substrate with hexagonal structure of side 2  $\mu\text{m}$ , separation 1  $\mu\text{m}$  and height 0.85  $\mu\text{m}$  to grow MQW LED.<sup>75</sup> The enhancement in external efficiency to 22 mW and 35% at 20 mA injection current was attributed to the light scattering at the patterned sapphire and GaN interface. Wu et al. and Wang et al. used circular holes patterned on sapphire to grow InGaN-GaN MQW LED.<sup>76,77</sup> The (0001) patterned sapphire substrate (PSS) had hole diameter of 3  $\mu\text{m}$ , spacing of 3  $\mu\text{m}$  and height varied from 0.5 to 1.5  $\mu\text{m}$ . PSS with a depth of 1.5  $\mu\text{m}$  showed the lowest dislocation density. The enhancement in efficiency was reported to be ~63% over a conventional LED. It was shown through light output pattern (angular distribution) that the enhancement was mainly due to light scattering at the PSS/GaN interface despite reduction in dislocation density. The internal quantum efficiency for PSS LED was 38% which was very close to 36% found for conventional LED. Cheong et al. formed V-shaped grooves on sapphire substrate by wet etching with  $\text{H}_2\text{SO}_4\text{-H}_3\text{PO}_4$  solution using  $\text{SiO}_2$  strips as hard mask.<sup>78</sup> The V-grooves in  $\langle 11\bar{2}0 \rangle$  direction on (0001) sapphire had a width of 5  $\mu\text{m}$  and spacing of 3  $\mu\text{m}$ . The V-grooves resulted in lower threading dislocation density of  $2\text{-}4 \times 10^7 \text{ cm}^{-2}$ . Both the internal and external efficiency was reported to significantly increase over conventional substrate. Gao et al. used pyramidal pattern sapphire substrate to grow InGaN/GaN LED.<sup>79</sup> The patterning was done at both micro- and nano-scale. For micro-scale patterning, patterns with 3  $\mu\text{m}$  diameter and 3  $\mu\text{m}$  spacing was used to form  $\text{SiO}_2$  hard mask. Mixture of  $\text{H}_2\text{SO}_4\text{-H}_3\text{PO}_4$  solution was then used to form pyramidal shapes on sapphire substrate. For nano-scale patterning, Ni layer was deposited on to  $\text{SiO}_2$ /sapphire layer. Ni nano-islands formed on annealing acted as hard mask for  $\text{SiO}_2$  etching, which in turn formed mask for sapphire etching. In comparison to planar substrates, the micro-patterned and

nano-patterned sapphire substrate improved efficiency by 29% and 48% respectively at an injection current of 20 mA. The enhancement was attributed to both better quality of epitaxial film and improvement in light scattering. Figure 2-5 shows the most common patterned sapphire substrate with cylindrical holes and also a substrate with protruding prismatic pattern.

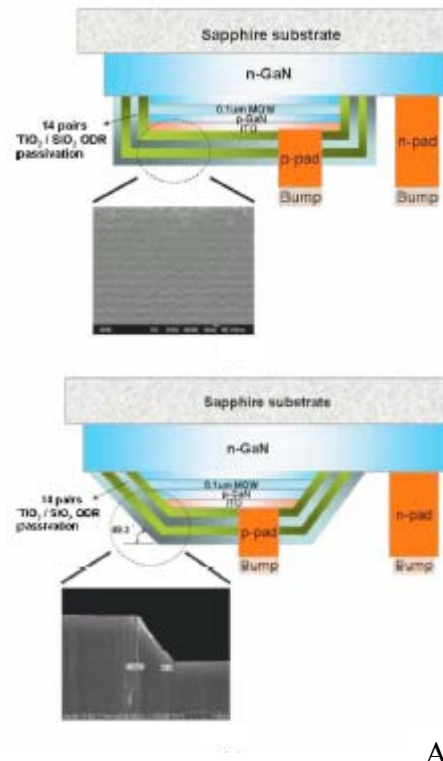
### **External Out-couplers: Microlens**

External out-couplers refers to any structure on the light emitting side of devices which helps in light extraction be it epoxy hemispherical dome, anti-reflection coatings, or micro-structures. Among the most widely studied external out-couplers are micro-structures like microlens arrays. Madigan et al. reported an improvement of 300% by application of spherically shaped macro-lens on the back side, at the center of which was placed an OLED.<sup>12</sup> But in most applications it is not possible to use these relatively larger spherical domes without having an index mismatch issue. Recently arrays of microlenses, on the light emitting face, have been looked into to increase the coupling efficiencies. Figure 2-6 shows microlens arrays attached to the light emitting side of an OLED. An increase of 1.5 times in external efficiency was observed by Möller et al. by attaching a square array of polymeric microlenses of 10  $\mu\text{m}$  diameter to the glass substrate in an OLED.<sup>80</sup> In comparison, two-dimensional ray tracing simulation predicted an increase of 2.3 times. The discrepancy in the experimental and computed values was attributed to imperfect microlenses and less than 100% area coverage by the microlenses. Increase in emission was more pronounced at high angles upon use of microlens arrays. Wei and Su observed an improvement in out coupling of 56% with square shaped microlenses of size 100  $\mu\text{m}$  and 80% area coverage.<sup>81</sup> An empirical relation between the area coverage and

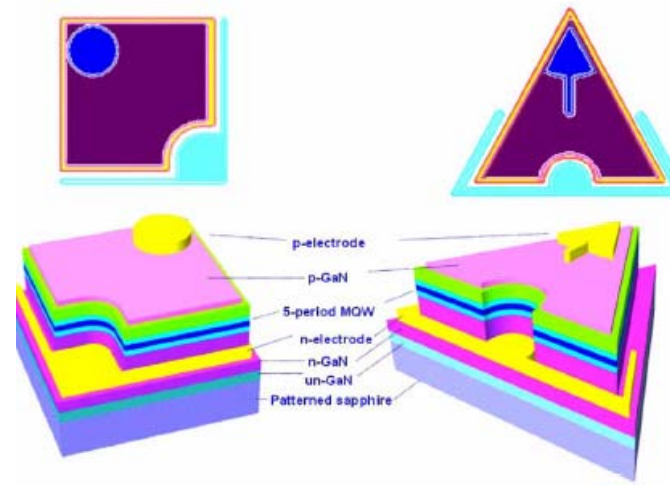
efficiency enhancement for various diameter lenses (100 – 190  $\mu\text{m}$ ) was derived. Peng et al. predicted an improvement of 85% using microlens arrays based on ray tracing simulations.<sup>82</sup> Simulation of out-coupling with different lens shape showed highest out coupling for a perfect hemispherical lens and was found to be independent of lens diameter. A maximum increase of 70% for 10  $\mu\text{m}$  diameter hemispherical lens was observed. 5, 15 and 20  $\mu\text{m}$  diameter microlens arrays showed improvements between 20-40% which was attributed to the deviation in shape from a hemisphere and area coverage for different diameter lenses. Choi et al. used microlenses on GaN micro-LEDs with each sapphire microlens on top of one micro-LED (MQW structure).<sup>83</sup> The lens acted as a hemispherical dome for each micro-LED. The results showed a more pronounced change in directionality of the emitted light than enhancement in extraction which was around 23%. Khizar et al. used integrated microlens on sapphire substrate of an AlGaIn UV LED.<sup>84</sup> The 12  $\mu\text{m}$  diameter microlenses with a height of 1  $\mu\text{m}$  enhanced the out coupling by 55%. Kim et al. fabricated microlens array on GaN based blue LED using photoresist reflow and reactive ion etching.<sup>85</sup> The microlenses with height of 1.2  $\mu\text{m}$  and two different diameters of 10  $\mu\text{m}$  and 5  $\mu\text{m}$  led to approximately 40% and 100% enhancement in efficiency. Sun et al. used monte carlo and finite difference time domain simulations to optimize lens design for a white OLED.<sup>86</sup> Finite difference time domain calculations showed an enhancement by a factor of 1.8 for perfect hemispherical lenses whereas the imprint lithography prepared hexagonal array of microlenses of diameter 6.6  $\mu\text{m}$  and height 2.2  $\mu\text{m}$  resulted in 50% enhancement in light extraction. Huang et al. used micro-contact printing to form microlens arrays.<sup>87</sup> Hydrophilic circular pattern was printed on to substrate by micro-contact. The NOA65 prepolymer spun on to the

substrate, self-assembled in the hydrophilic regions in the shape of microlenses which was then UV cured. Microlens array increased the overall light output by 24.5% where as it increased light output by as much as 60% at a view angle of 80°. Ee et al. used silica particles embedded into polystyrene layer to form microlens topography on top of an InGaN LED.<sup>88</sup> A monolayer of SiO<sub>2</sub> particle of size 1 μm was assembled on top of a monolayer of polystyrene particles of same size. The SiO<sub>2</sub> particles were then semi-buried into polystyrene by heating to 140°C. An improvement of more than 2 fold in output power was observed at an injection current of 100 mA. Lee et al. fabricated stepped microlens array on to GaN/sapphire blue LED by focused ion milling.<sup>89</sup> The microlens array led to 1.6 fold increase in output power. Sun et al. used a combination of microlens arrays on top of glass substrate and low index grids beneath ITO layer in an OLED to improve power efficiency to 68±4 lm/W and an efficiency of 34±2%, which is ~2.3 fold increase over conventional OLED.<sup>90</sup> Lee et al. fabricated randomly arranged SiO<sub>2</sub> hemispherical microlens on GaN LED by liquid phase deposition of SiO<sub>2</sub>.<sup>91</sup> The lens shape and morphology of SiO<sub>2</sub> nuclei was controlled by controlling the deposition temperature. The microlens had a height of 190 nm and diameter of 350 nm with area coverage of 43%. An enhancement of 1.44 fold was observed at a forward current of 20 mA. Apart from microlens of truncated spherical/hemispherical shape, many other microstructures have been fabricated on the top surface to increase light out-coupling. Nakamura et al. formed pyramid shaped microlens of polyethyleneterephthalate (PET) and high index resin on top of an OLED.<sup>92</sup> The base of pyramid was 10 μm with side wall slope of 50°. An improvement of 1.5 times was observed with the use of pyramidal microlenses. Surprisingly no difference in luminous intensity with use of high index resin

was observed in their work. Melpignano et al. fabricated spherical microlens using UV casting on OLED.<sup>93</sup> The fabricated ceiling light illuminator showed an improvement of 70% in far-field emission. Ray tracing simulations on different type of top encapsulant e.g. prism, hemispherical lens, cone, inverted cone, inverted microlens was done by Chang et al.<sup>94</sup> Prisms were shown to be the most efficient structure with extraction efficiency increasing with prism height. The experimental results corroborated the increase in efficiency with increase in aspect ratio. Bao et al. used both 1D and 2D taper like gratings made of PDMS on sapphire substrate of a GaN based LED to enhance efficiency.<sup>95</sup> The 2D gratings showed higher enhancement in out-coupling. It was shown that the enhancement came from out-coupling of rays beyond the critical angle. Lee et al. used micro-pyramidal array of base 5  $\mu\text{m}$  and apex angle from  $20^\circ$  to  $70^\circ$  on three different kind of LEDs (wire bonded, flip chip, and thin GaN) to simulate for the extraction efficiency.<sup>96</sup> Micro-pyramids with an apex angle of  $30^\circ$  gave the maximum efficiency. Simulations showed that texturing both sides of sapphire substrate increases the efficiency further. Greiner through ray tracing simulations on microlens, micro-pyramid arrays and scattering layer of nano-particles showed the reflectance of the back layer/active layer stack to be of primary importance and the type of out-coupler secondary as long as it redirects light.<sup>13</sup> It was shown that the aspect ratio of out-couplers increases the efficiency as does the increase in the area coverage.



A



B

Figure 2-1. LED chip shaping to increase light out-coupling A) vertical walls of a conventional LED replaced by 50° inclined wall [Reprinted with permission from C. H. Chiu, H.C. Kuo, C. F. Lai, H. W. Huang, W. C. Wang, T. C. Lu, S. C. Wang, and C. H. Lin, J. Electrochem. Soc., 154, H944 (2007).] B) triangular shaped LED chip instead of a conventional rectangular chip [Reprinted with permission from J. Y. Kim, M. K. Kwon, J. P. Kim, and S. J. Park, IEEE Photon. Technol. Lett., 19, 1865 (2007).]

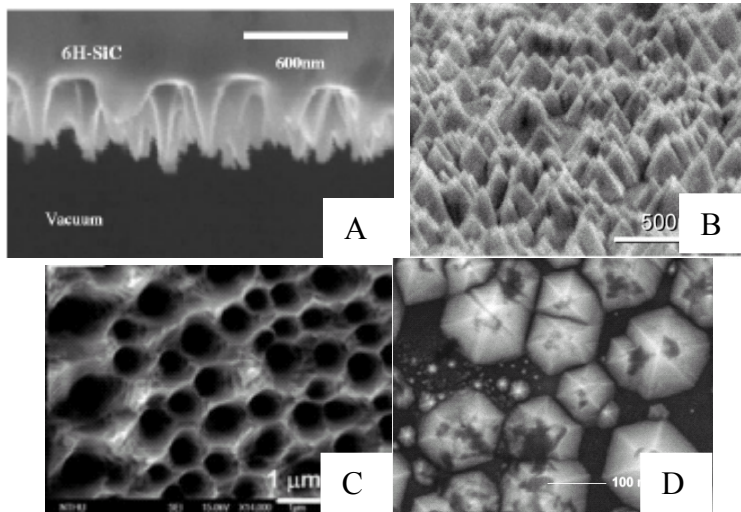


Figure 2-2. Photon randomization by surface roughening A) SiC roughened by dry etching using naturally grown Au mask [Reprinted with permission from H. Kasugai, Y. Miyake, A. Honshio, S. Mishima, T. Kawashima, K. Iida, M. Iwaya, S. Kamiyama, H. Amano, I. Akasaki, H. Kinoshita, and H. Shiomi, *Jpn. J. Appl. Phys.*, 44, 7414 (2005).] B) N-face GaN roughened by photochemical etching in KOH [Reprinted with permission from T. Fujii, Y. Gao, R. Sharma, E. L. Hu, S. P. DenBaars, and S. Nakamura, *Appl. Phys. Lett.*, 84, 885 (2004).] C) nano-porous n-GaP surface formed by electrodeless photo-electrochemical etching [Reprinted with permission from J. M. Hwang, W. H. Hung, and H. L. Hwang, *IEEE Photon. Technol. Lett.*, 20, 608 (2008).] D) photo-enhanced chemical etching of n-GaN [Reprinted with permission from H. Fang, X. N. Kang, C.Y. Hu, T. Dai, Z. Z. Chen, Z. X. Qin, B. Zhang, and G. Y. Zhang, *J. Crystal Growth*, 298, 703 (2007).]

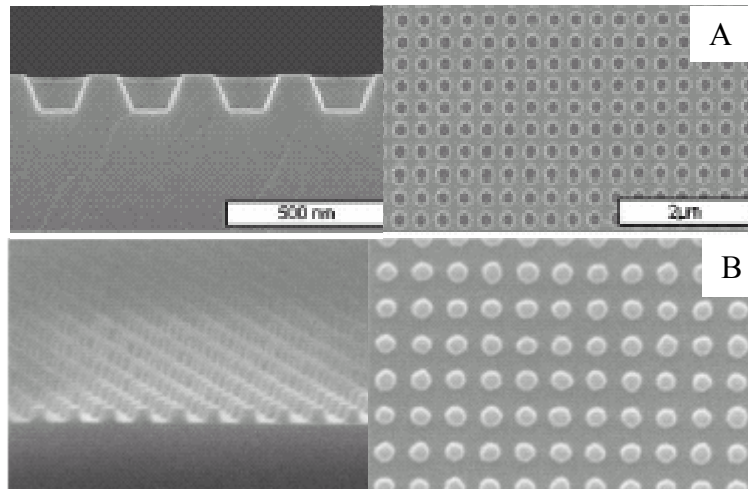


Figure 2-3. Types of two-dimensional photonic crystals A) cylindrical air holes arranged in a square pattern [Reprinted with permission from J. Y. Kim, M. K. Kwon, K. S. Lee, S. J. Park, S. H. Kim, and K. D. Lee, *Appl. Phys. Lett.*, 91, 181109 (2007).] B) cylindrical pillars of SiO<sub>2</sub> in a square pattern [Reprinted with permission from Y. R. Do, D. H. Park, Y. C. Kim, and Y. D. Huh, *J. Electrochem. Soc.*, 150, H260 (2003).]

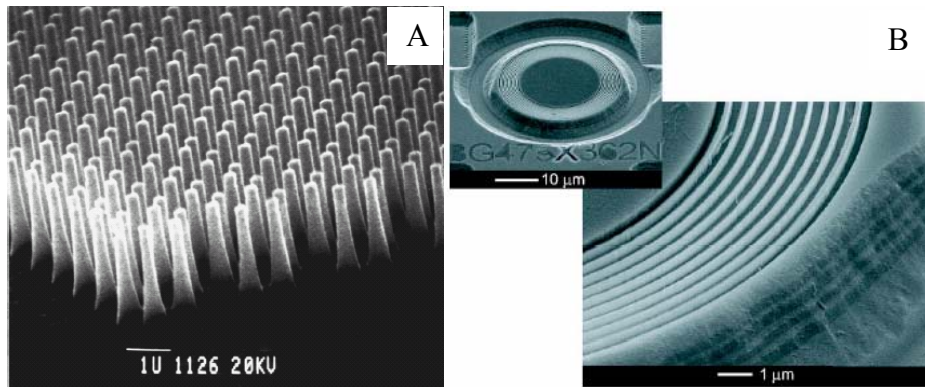


Figure 2-4. Other periodic patterns used to enhance light extraction. A) cylindrical pillars in honey comb arrangement [Reprinted with permission from T. Baba, K. Inoshita, H. Tanaka, J. Yonekura, M. Ariga, A. Matsutani, T. Miyamoto, F. Koyama, and K. Iga, *J. Light Tech.*, 17, 2113 (1999).] B) circular Bragg gratings [Reprinted with permission from M. Y. Su, and R. P. Mirin, *Appl. Phys. Lett.*, 89, 033105 (2006).]

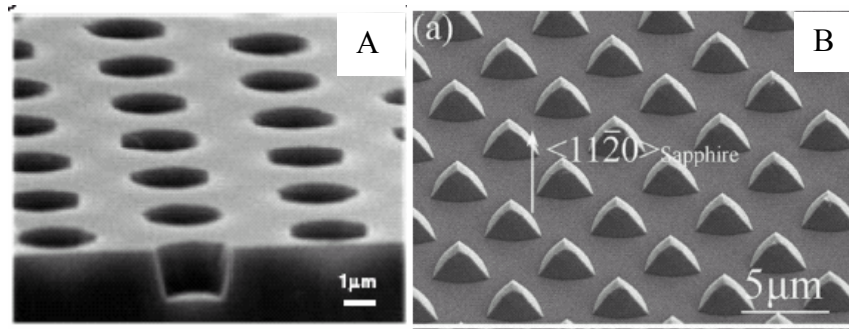


Figure 2-5. Patterned sapphire substrates for epi-layer growth A) most common patterned substrate with cylindrical holes in a square arrangement [Reprinted with permission from W. K. Wang, D. S. Wu, W. C. Shih, J. S. Fang, C. E. Lee, W. Y. Lin, P. Han, R. H. Horng, T. C. Hsu, T. C. Huo, M. J. Jou, A. Lin and Y. H. Yu, *Jpn. J. Appl. Phys.*, 44, 2512 (2005).] B) sapphire with protruding prismatic patterns [Reprinted with permission from H. Gao, F. Yan, Y. Zhang, J. Li, Y. Zeng, and G. Wang, *J. Appl. Phys.*, 103, 014314 (2008).]

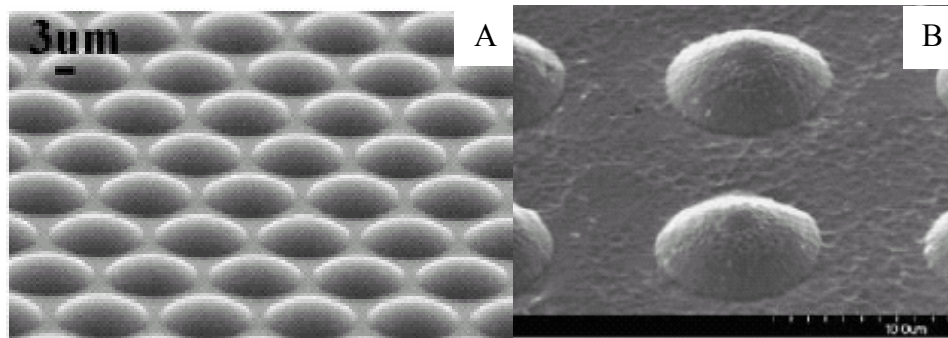


Figure 2-6. Microlens as external out-coupler for enhanced light extraction A) polydimethyl-siloxane (PDMS) microlens formed by photoresist reflow method [Reprinted with permission from H. Peng, Y. L. Ho, X. J. Yu, M. Wong, and H. S. Kwok, *J. Display Tech.*, 1, 278 (2005).] B) GaN microlens formed by photoresist reflow followed by dry etching [Reprinted with permission from D. Kim, H. Lee, N. Cho, Y. Sung, and G. Yeom, *Jpn. J Appl. Phys.*, 44, L18 (2005).]

## CHAPTER 3 OUTLINE OF RESEARCH

This work focuses on the enhancement of light extraction through surface modification using surface structures like arrays of microlens, micro-pyramids, micro-cones etc. These external out-couplers particularly array of microlenses on the front surface has been shown to enhance the light extraction efficiency between 120 - 300%. In many of these studies, microlens arrays and other structures were fabricated using polymeric materials which not only degrade with time but also have issues with its low refractive index, limiting its efficacy. Though this method has recently received some attention, there is a need to thoroughly understand the ray dynamics involved with enhancement of light out-coupling by these structures and also of a fabrication technique particularly for microlens arrays, versatile in its applicability to many substrate materials and compatible with semiconductor/IC fabrication processes. The ray dynamics in the presence of these regular periodic structures can be expected to be more than simple photon randomization and has been investigated using geometrical optical analysis and ray tracing simulations. A new method for fabrication of microlens array has also been demonstrated. This new fabrication method uses chemical mechanical polishing to form microlens arrays and can fabricate microlenses directly onto a wide variety of substrate materials with a very high accuracy and is fully compatible with the current semiconductor/IC fabrication processes.

In this dissertation, Chapter 4 discusses the ray tracing simulations, experimental procedure and characterization techniques that were used for the investigation. Chapter 5 presents the two-dimensional geometrical analysis of ray dynamics of a surface with triangular features on the top surface. The changes in ray dynamics with change in the

inclination of sides are discussed. The effect on out-coupling has been corroborated by ray tracing simulations. Chapter 6 presents the ray tracing analysis of ray dynamics upon use of microlens arrays. The effect of different lens parameter like diameter, height, area coverage and the effect of substrate refractive index have been evaluated. Chapter 7 presents chemical mechanical polishing (CMP) as a new technique for creation of various topographies. The effect of various CMP variables particularly polishing pad and down pressure has been studied. Chapter 8 shows the fabrication and characterization of microlens array on glass substrate using chemical mechanical polishing. Chapter 9 presents the experimentally measured light out-coupling and the angular distribution of intensity from substrates with conical and microlens array on top. The advantages of using these structures over simple surface roughening have been established. Chapter 10 summarizes the conclusions from both the ray tracing simulations and experimental measurements of light out-coupling. It also presents the advantages of CMP, which till now has only been looked at as a planarization technique, for topographic shaping.

## CHAPTER 4 EXPERIMENTAL PROCEDURE

### Ray Tracing Simulations

#### Simulation Software

LightTools from Optical Research Associates is an illumination design software package based on 3D solid modeling and combines full optical accuracy with powerful analysis features. It can be used to create virtual prototypes of optical systems for a wide range of applications. The illumination analysis in LightTools is based on a Monte Carlo trace. This method traces a desired number of rays from randomly selected points in the source and with random directionality within the user defined constraints. Each ray starts with a specific amount of power which is then modified by various surfaces in the ray path. These rays after passing through material layers and surfaces with user defined properties, are then collected on specified receiver surface for statistical analysis and graphical display. The ray tracing is non-sequential i.e. the rays follow the laws of optics representing the physical reality of the system.

#### Device Simulated

Figure 4-1 shows the schematic of the device simulated in our study. It consist of a high refractive index active layer (thickness,  $t \sim 2 \mu\text{m}$ , refractive index,  $n \sim 1.93$ ) on a glass substrate ( $t=1 \text{ mm}$ ,  $n=1.515, 1.7, 1.93$ ). The device size was  $2 \text{ mm} \times 2 \text{ mm}$  with reflecting sides. The top surface of the glass substrate was textured with conical, pyramidal, prismatic, and microlens arrays of base width/diameter  $20 \mu\text{m}$  with different aspect ratios. The bottom surface of active layer was assumed to have a reflective contact with different absorptions. Fresnel losses were considered for both the substrate-air and substrate-active layer interface. Out-coupling was measured by placing large detectors close to the surfaces, whereas angular distribution of intensity was determined by placing a far-field detector centered on the glass substrate.

## **Simulation Parameters**

Monte Carlo ray tracing simulations were done for a million rays isotropically generated in the active layer. It is generally agreed that photon generation in the active layers of LEDs, OLEDs and thin film phosphors is isotropic. All simulations were done for light with wave length 593 nm. Absorption at the back surface was realized by reducing the power of rays after every incidence. Fresnel losses were taken into account for interaction at the surfaces. There was no noticeable difference in the results when the number of rays was increased to ten million.

## **Microstructure Formation**

### **Lithography**

Hexagonal array of circular dots with 20  $\mu\text{m}$  diameter and 5  $\mu\text{m}$  spacing was patterned in a 1  $\text{cm}^2$  area on 1  $\text{inch}^2$  glass (Corning 2496) coupons. 2000  $\text{\AA}$  Cu was deposited on top of 50  $\text{\AA}$  Cr adhesion layer on these glass coupons to form a hard mask. Microposit S1813 photoresist and standard UV photolithography using a Karl Suss MA6 Aligner with a 365 nm Hg i-line radiation was used to develop the pattern. Microposit S1813 photoresist was spun on the glass coupons at 5000 rpm to form  $\sim 1\mu\text{m}$  thick photoresist layer. The photoresist was soft baked at 105°C for 30 min before exposure. The exposed photoresist was dissolved using AZ-300 MIF developer. The developed pattern was dry etched with 20 sccm  $\text{O}_2$  in a Uniaxis Shuttlelock RIE-ICP reactor under 100 W DC and 600 W RF power for 10-20 s to remove any residual photoresist in the exposed part of the pattern.

### **Etching**

Both dry etching (Uniaxis Shuttlelock RIE-ICP) and wet etching were used in this work. The etching recipes of various materials are given below:

Silica: PECVD silicon oxide, 1  $\mu\text{m}$  thick was deposited by flowing nitrous oxide ( $\text{N}_2\text{O}$ ) and silane (2%  $\text{SiH}_4/\text{N}_2$ ) gases at a flow rate of 1420 and 400 sccm, respectively, at a temperature of  $300^\circ\text{C}$  while the chamber pressure was maintained around 550 mTorr. Power was kept at 60 W at a frequency of 187 kHz for formation of low stress silicon oxide. PECVD silica was dry etched in Uniaxis Shuttlelock RIE-ICP reactor in 15 sccm  $\text{SF}_6$ , 5 sccm Ar at 5 mTorr pressure and 100 W DC and 600 W RF power to form cylindrical pillar-type patterns.

Cooper: Copper was removed by wet etching using Transene APS 100 Cu etchant containing Ammonium persulfate. The 2000  $\text{\AA}$  of Cu layer exposed after lithography was removed by 20% (vol./vol.) APS 100 solution in 40-60s. A significant lateral Cu removal was also observed during etching of copper. Any further exposure to APS 100 solution led to delamination of the photoresist layer.

Chromium: Chromium was removed by dry etching using Uniaxis Shuttlelock RIE-ICP reactor. 20 sccm Ar and 5 sccm  $\text{O}_2$  under 5 mTorr pressure, 200 W DC and 600 W RF power was used for 60-90 s to remove 50-100  $\text{\AA}$  of Cr adhesion layer from the exposed portion of the pattern.

The above recipe is for physical removal of Cr atoms by bombardment with high energy Ar ions. Wet etching of Cr using Cyantek ES 1 Chromium etchant was found to also etch copper and to be too harsh for the photoresist.

Glass: Wet etching using hydrofluoric acid was used to etch soda lime glass. After removing Cu by wet etching and Cr by reactive ion etching, the patterns were etched in 5% HF solution for 4-5 mins to form 20  $\mu\text{m}$  diameter cone shaped structures of glass. The Cu layer was observed to delaminate after  $\sim$ 4-5 mins of etching in 5% HF solution. The height of the conical structure obtained was around 2.5-3.0  $\mu\text{m}$ . The lateral etch rate was found to be higher than vertical etch

rate. Lowering of lateral etch rate would result in higher aspect ratio of conical features which can be achieved by better mask/substrate interface properties.

### **Chemical Mechanical Polishing**

The patterned and etched samples with conical or cylindrical arrays were polished using Struers Co. TegraPol-35 with TegraForce-5 tabletop polisher at different down pressures. Polishing was done using both soft Politex™ and harder IC 1000/Suba IV pads with both the polishing head and pad rotating in the same direction and at 100 rpm. Politex™ pad is among the softest CMP pads used for final polishing of wafers compared to Suba™ and IC™ series harder pad which are used to achieve better planarity in wafers. 5 wt% SiO<sub>2</sub> slurry made from dilution of Levasil 50cK (nominal particle size ~80 nm) at pH 4.0 and a flow rate of 50 mL/min was used during polishing. The surface was characterized using a Veeco Dimension 3100 Atomic force microscope using contact mode.

### **Out-Coupling Measurements**

After formation of conical and microlens array on glass coupons using lithography and etching, the substrates were backed by a polished aluminum disk with a 2 mm diameter hole in the center. A 2 mm diameter LED (SunLED XSUG62D) was inserted through the center opening for light generation. The LED and aluminum disk were attached to the glass coupons using an index matching adhesive (Norland Optical adhesive 65). Two types of measurement were taken, one with a completely absorbing back ensured by having a thick graphite coating on the back of the glass substrate and second for a reflective back surface accomplished by sputter coating Al on the back side of glass. In both cases, a 2 mm diameter area at the center was kept clear for LED attachment. The LED was operated with a constant current source (10 mA) to keep the

intensity of generated photons constant for every measurement. Figure 4-2 shows emission characteristic and spatial distribution of the LED.

### **Total Out-coupling: Integrating Sphere**

Figure 4-3 shows the experimental setup to measure the total out-coupling efficiency of the substrates. The substrate with a LED attached at the back was inserted into an integrating sphere. Constant current (5, 10, 15, 20 mA) was supplied using Instek Laboratory DC power supply (Model PS-1830D) where as the Keithley multimeter was used to measure the current accurately. An optical fiber for detection was inserted into an orthogonal port of the integrating sphere for intensity measurement. The optical fiber was fed to an Ocean optics solid state spectrometer USB S2000 from which data was acquired through a computer. An integrating sphere consists of a hollow cavity with its interior coated for high diffuse reflectivity having small holes as needed for entrance and exit ports. Light rays incident on any point on the inner surface are, by multiple scattering reflections, distributed equally to all other such points. The effects of the original directionality of incident beam are minimized. It preserves the effect of power while totally destroying the effects of spatial distribution of a source; it can thus be used to measure total out-coupling efficiency.

### **Angular Intensity Measurement**

Figure 4-4 shows the experimental arrangement for measurement of angular intensity distribution. The textured substrate was mounted on a rotatable jig with fiber optic aligned with the center of the substrate at a distance of 3 inch. The substrate was illuminated by a backing LED (SunLED XSUG62D) driven by constant current of 10 mA. The angular intensity was measured by rotating the jig along an axis through the center of the substrate. Ocean optics USB

S2000 spectrometer was used to measure the light intensity. The measured intensity represents the far-field spatial distribution of photons from the textured substrates.

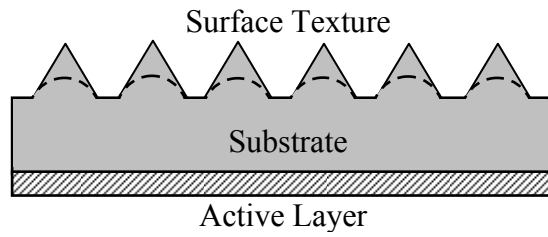


Figure 4-1. Schematic of the devices simulated in this study

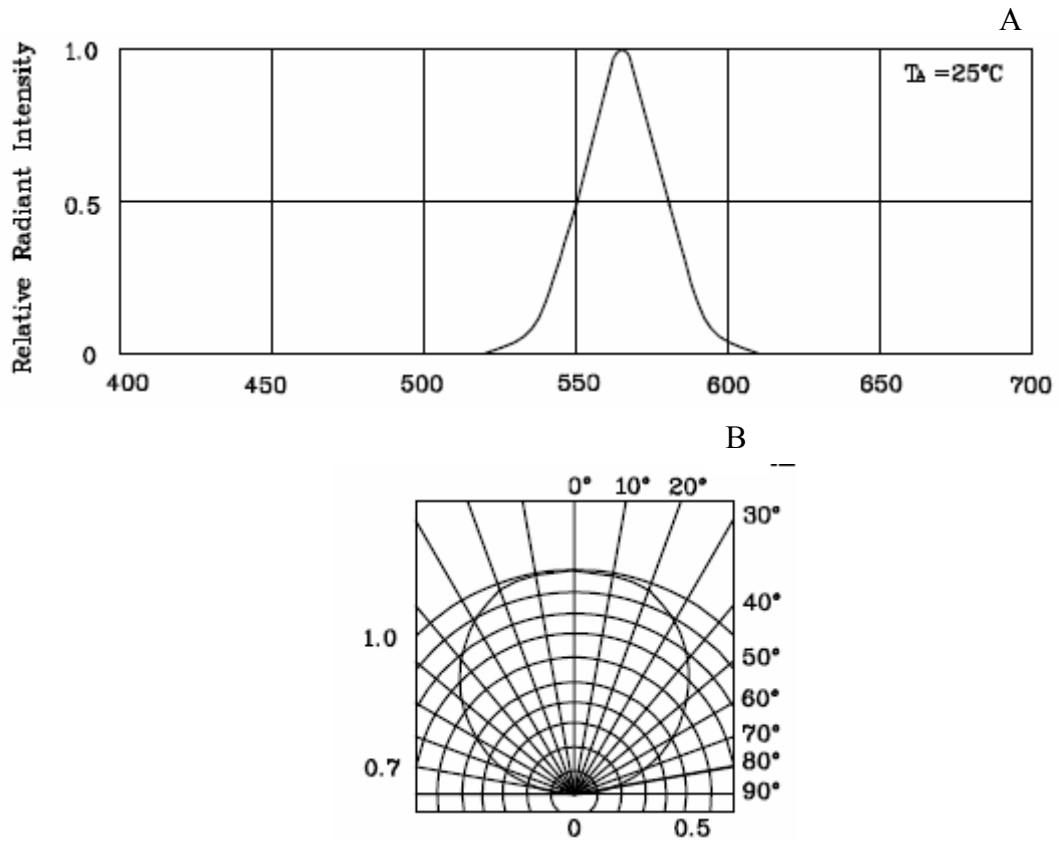


Figure 4-2. Characteristics of red light emitting SunLED XSUG62D LED used for out-coupling measurements A) emission characteristic and B) spatial distribution of intensity.

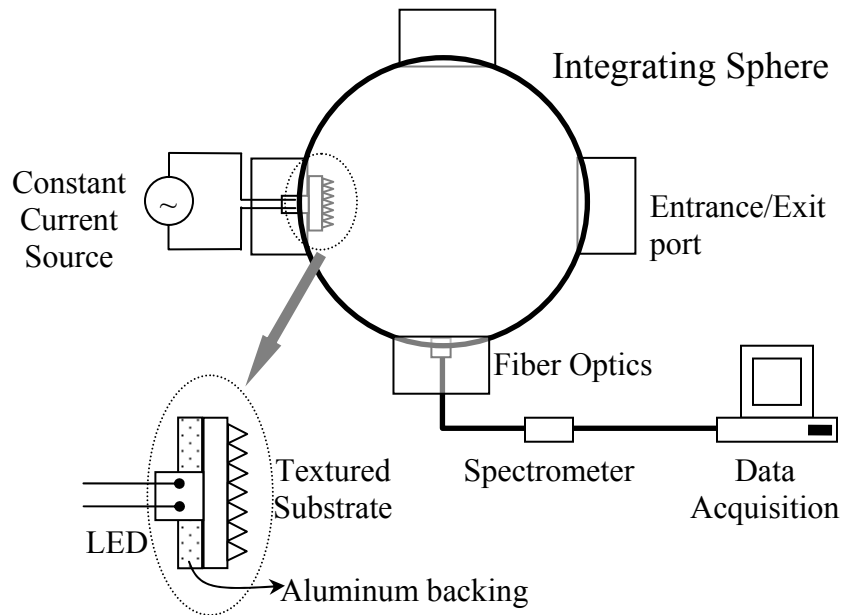


Figure 4-3. Integrating sphere setup for measurement of total out-coupling efficiency.

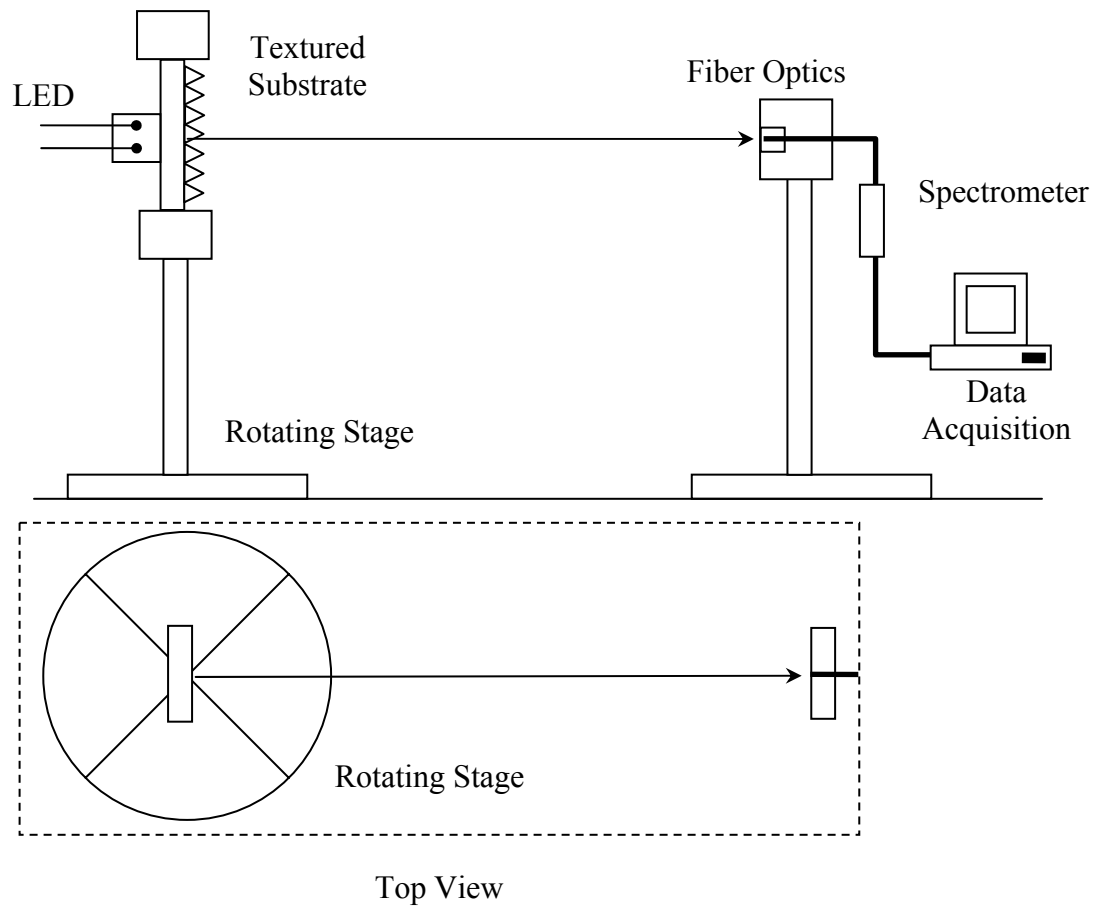


Figure 4-4. Measurement set-up for angular distribution of emission from various substrates.

CHAPTER 5  
ANALYTICAL TREATMENT OF LIGHT EXTRACTION FROM TEXTURED  
SURFACES USING CLASSICAL RAY OPTICS

**Introduction**

The primary reason for low external efficiency of solid state lighting devices e.g. LEDs, OLEDs is the poor light extraction or out-coupling efficiency. Large differences in the optical density of active material and surrounding media gives rise to total internal reflection and wave-guiding of generated photons. The larger the difference in refractive indices the smaller is the critical angle for total internal reflection, consequently a large portion of generated photons are repeatedly reflected into the material and finally absorbed by non-emissive processes. Critical angle defines the escape cone for a pair of media, only a small fraction of the total light, those within the escape cone couple out of the device. Out-coupling efficiency can be increased by increasing the number of escape cones or by reduction of wave-guiding. In an LED chip, this has been achieved by opening of bottom and lateral cones, tilting of side walls and shaping (e.g. rhombohedral) of chip.<sup>17-24</sup> Wave-guiding has been reduced by introduction of varying degree of randomization in the photon dynamics.<sup>25-49</sup> Randomization reduces wave-guiding by changing the angle of propagation of photons after each reflection and thus providing multiple chances to photons to escape. Photon randomization is achieved by modification of various interfaces in the device. One of the simplest techniques for randomization is surface roughening. Had it not been for the absorption of photons in various layers, randomization can theoretically provide infinite chances to photons to escape leading to eventual extraction of all photons in the layer. Apart from surface roughening, various regular and periodic structures e.g. Bragg gratings,<sup>9</sup> micro-rings,<sup>10</sup> photonic crystals,<sup>11</sup>

microlens,<sup>12</sup> pyramids,<sup>13</sup> etc. has been used to introduce varying degree of randomization. These regular structures (micro-textured) work both ways, photons beyond the critical angle are reflected back at a different angle hence getting another chance to escape, on the other hand some of the rays which otherwise would have escaped from a planar surface are also reflected back hence increasing its chances of absorption. The mechanism through which these structures enhance extraction is not well understood. In this work we have attempted to analytically understand the changes in ray dynamics that lead to enhancement in light extraction when the surface is non-planar. The analysis is done for a 2D device with regular triangular structures on top surface as shown in Figure 5-1(A). The change in ray dynamics with increase in the inclination of the side (decrease in ' $\alpha$ ') has been studied using classical ray optics. Out-coupling enhancement by other structures is discussed based on this analysis.

### **Analysis of Ray Dynamics**

Figure 5-1(A) shows the structure of the surface and device been analyzed in this work. The triangular features with an inclination of ' $\alpha$ ' are on top surface of the substrate where as a light emitting thin active layer is assumed on the other side. This structure is similar to that of an OLED, a thin film phosphor device and LEDs with light emission through the substrate (flip chip), where there is a difference in refractive index of active and substrate layers. In such a case there will be lambertian distribution of rays in the substrate layer. If the refractive index of top layer is same as that of active layer as in case of front emitting LEDs, there will be an isotropic angular distribution of rays. Rays incident on the inclined walls of the triangular features has been divided into two regions

one on each side of the surface normal as shown in Figure 5-1(B). The ray dynamics upon incidence to the surface in these regions are discussed separately.

### Ray Incidence in Region I

The angle of incidence  $\beta$  of rays can vary from 0 to  $\pi/2$ . Rays with incident angle less than  $\theta_c$  to the surface will out-couple at the first incidence. This gives

$$0 < \beta < \theta_c : \text{Out-couple at 1}^{\text{st}} \text{ incidence}$$

Rays incident at an angle between  $\theta_c < \beta < \pi/2$  will experience internal reflection. Depending on the direction of propagation after reflection, the reflected ray may travel towards the active layer or be incident on surface with opposite inclination. The angle of incidence to the surface after 1<sup>st</sup> reflection i.e. at 2<sup>nd</sup> incidence point is given by

$$\beta_2 = |(2\alpha - \beta)|$$

Rays with  $(2\alpha - \beta) > 0$  would lie in region II, where as those with  $(2\alpha - \beta) < 0$  would lie in region I at 2<sup>nd</sup> incidence. Figure 5-2 schematically illustrates the angle of incidence at 2<sup>nd</sup> incident point. After 1<sup>st</sup> internal reflection ray 1 lies in region II (1') where as ray 2 in region I (2'). Rays with  $0 < \beta_2 < \theta_c$  will out-couple after 2<sup>nd</sup> incidence.

The range of  $\beta$  for out-coupling at 2<sup>nd</sup> incidence is given by

$$(2\alpha - \theta_c) < \beta < 2\alpha: \text{Out-couple at 2}^{\text{nd}} \text{ incidence from Region II}$$

$$2\alpha < \beta < (2\alpha + \theta_c): \text{Out-couple at 2}^{\text{nd}} \text{ incidence from Region I}$$

This leaves two range of  $\beta$  in region I not out-coupled after 2<sup>nd</sup> incidence.

$$\theta_c < \beta < (2\alpha - \theta_c) \text{ and } (2\alpha + \theta_c) < \beta < \pi/2$$

The various range of  $\beta$  in region I are schematically shown in Figure 5-3(A).  $\beta$  in the range  $\theta_c < \beta < (2\alpha - \theta_c)$  lie in region II at 2<sup>nd</sup> incidence and is reflected back towards the

active layer. Rays in the range  $(2\alpha + \theta_c) < \beta < \pi/2$  lie in region I at 2<sup>nd</sup> incidence with its angle of incidence reduced by  $2\alpha$ . The rays in this range can be out-coupled if it avoids the range between  $\theta_c$  and  $(2\alpha - \theta_c)$  at subsequent incidences. In such an event rays will either out-couple or will move up the structure with reduced angle of incidence until extracted. Ray incident in the range  $\theta_c < \beta < (2\alpha - \theta_c)$  should be minimized after every reflection, since in this range the rays are internally reflected back towards the active region where not only the absorption is high but also the probability of absorption at contacts are high. The limits on  $\beta$  in the above analysis can overlap or become unrealistic depending on the values of  $\alpha$  and  $\theta_c$ . In such an event, the limits will need adjustment considering that the lower limit has to be positive,  $\beta$  less than  $\theta_c$  out-couple and upper limit can't exceed  $\pi/2$ . Figure 5-3(B) and (C) illustrates the cases of over-exceeding limits of  $\beta$ . When  $\alpha$  is large i.e. for a surface with low inclination, angular zone between  $\theta_c$  and  $(2\alpha - \theta_c)$  is large. In such a case, large portion of light will be reflected back towards the active layer. This zone reduces as inclination is increased ( $\alpha$  decreased). For small values of  $\alpha$  i.e. for steep structures,  $(2\alpha - \theta_c)$  may become less than  $\theta_c$  as shown in Figure 5-3(C). The minimum inclination needed to out-couple maximum rays in this region without back reflection is when either  $2\alpha - \theta_c = \theta_c$  or  $2\alpha + \theta_c = \pi/2$  i.e.  $\alpha$  lies between  $\theta_c$  and  $\frac{1}{2}\left(\frac{\pi}{2} - \theta_c\right)$  as can be seen from Figure 5-3. It also ensures out-coupling with the minimum possible number of reflections. Now let's look at the ray dynamics in region II.

## Ray Incidence in Region II

Light emitted from active region will have an angular spread of  $\pi/2$ . Light coming from active layer will make an incident angle in the range  $0 < \beta < \alpha$ . Those beyond this range will come from the reflections from region I. We have considered the whole range of  $0 < \beta < \pi/2$  in region II.

Again rays with incident angle within  $\theta_c$  will out-couple.

$0 < \beta < \theta_c$ : Out-couple 1<sup>st</sup> incidence

Rays at higher angle of incidences will be internally reflected towards active layer. After reflection from the back surface it will emerge with an unchanged angle to vertical. These rays might incident on the face with similar inclination or with opposite inclination as shown in Figure 5-4. Upon incidence on the face with opposite inclination it will be in region I and subtend same incident angle  $\beta$ . These rays will behave as if it were 1<sup>st</sup> incident in region I of the surface. Rays incident on face with same inclination will subtend a different angle and are discussed below. These rays will make an angle of  $\beta_2 = |\pi - 2\alpha - \beta|$  at 2<sup>nd</sup> incidence on the top surface. A closer look reveals that these rays are behaving as if it were reflected from surface with an inclination of  $(\pi/2 - \alpha)$ . Similar treatment of these rays as with rays in region I gives the range of out-coupling as shown in Figure 5-5(A).

$\theta_c < \beta < \pi - 2\alpha - \theta_c$ : Rays in this range will be reflected in region I with  $\beta_2$  lying in the same range  $\theta_c < \beta_2 < \pi - 2\alpha - \theta_c$ .

$\pi - 2\alpha - \theta_c < \beta < \pi - 2\alpha + \theta_c$ : These rays will be out-coupled after reflection.

$\pi - 2\alpha + \theta_c < \beta < \pi/2$ : These rays will be reflected in region II but will have an incident angle greater than  $\theta_c$  and hence reflected again but subtending a lower angle of

incidence this time. Figure 5-5(A) schematically shows the various zones in Region II. Similar to the analysis of Region I, the limits on  $\beta$  in analysis of Region II can also overlap or become unrealistic. In such an event, the limits will need adjustment as pointed out in the previous section. In this region, maximum rays will be out-coupled when either  $\pi - 2\alpha + \theta_c = \pi/2$  or  $\pi - 2\alpha = 2\theta_c$  i.e.  $\alpha$  lies between  $\left(\frac{\pi}{2} - \theta_c\right)$  and

$$\frac{1}{2}\left(\frac{\pi}{2} + \theta_c\right).$$

### Discussion of Ray Dynamics

It should be noted that for Region I rays within  $\pm\theta_c$  of  $\beta=2m\alpha$  will out-couple after  $m^{\text{th}}$  reflection ( $m = 0, 1, 2, \dots$ ). Those lying outside this zone are alternately reflected in Region I and II and a portion of these rays are wave-guided. For optical materials with high refractive index e.g. SiC ( $n = 2.8, \theta_c \sim 21^\circ$ ), the maximum value of  $m$  of any significance is just 2. Ray dynamics as analyzed and shown in Figure 5-3 is sufficient for most materials. The incident angle of rays in region I previously reflected from both region I and II and after back reflection is given by  $\pi-2\alpha-\gamma$  where  $\gamma$  is the incident angle at previous incidence in region II or  $\pi-4\alpha-\beta$  where  $\beta$  is the incident angle at previous incidence in region I ( $\gamma=2\alpha-\beta$ ). It can be seen from above that for  $\alpha > 45^\circ$ , the angle of incidence decreases for subsequent reflection bringing it closer to the out-coupling region of 0 and  $\theta_c$  where as for  $\alpha < 45^\circ$ , the angle of incidence increases for subsequent reflection bringing it closer to the out-coupling region of  $2\alpha \pm \theta_c$ . For  $\alpha = 45^\circ$  incident angle in region I remains unchanged and would lead to wave-guiding of photons. For  $\alpha < 45^\circ$  rays after every back reflection comes towards  $2\alpha \pm \theta_c$  region, which is the region for out-coupling from the opposite face (Figure 5-3). Thus for  $\alpha < 45^\circ$  these structures somewhat act as a

light entrapping structures. Figure 5-5(B) schematically summarizes the ray dynamics in both the regions. Figure 5-6 shows the different regions of out-coupling for surface inclined towards left from the perspective of angular distribution in the substrate layer. The figure shows the directionality of photons incident on one face of the triangle structure. If the angular distribution in the substrate layer is lambertian, the intensity is maximum in the forward direction and decreases at higher angles. In such cases out-coupling of photons in forward direction is important for overall efficiency. As can be seen from Figure 5-6, for  $\alpha = 45^\circ$  one of the out-coupling zones lies exactly on either side of forward direction. But  $\alpha = 45^\circ$  also leads to redirection of reflected photons at same angles and thus wave guiding of photons. Inclination larger or smaller than  $45^\circ$  is better for reduction of wave-guiding. It should be noted that some of the rays that out-couple from region II would travel below horizontal and reenter the device. The triangular structures cause bending of photons towards the device. This effect would be higher for steeper structures i.e. for smaller values of  $\alpha$  and would lead to loss of some of the out-coupled rays back in the device.

### **Ray Tracing Simulations**

2D and 3D monte carlo simulation was done using LightTools<sup>®</sup> to study the light extraction enhancement using inclined walls. Figure 5-7 shows the schematic of the substrate simulated in our study. The substrate had 2D (prism) and 3D (conical and pyramidal) structure with  $20\ \mu\text{m}$  base on the top surface. Light rays were isotropically generated in a  $2\ \mu\text{m}$  thick layer near the bottom of the substrate. The emission source was immersed in the substrate and had the same material properties and refractive index as the substrate. The side surfaces were 100% reflective to simulate an infinite substrate where

as the bottom surface was 80% reflective to realize absorption in devices. Simulations were done for substrate with three refractive indices, 1.5, 2.0 and 2.92 with critical angles of  $41^\circ$ ,  $30^\circ$ , and  $20^\circ$  respectively. For 2D simulations the light source was planar with emission only in the x-z plane where as for 3D simulations source emission was in all directions. All simulations were done for light with 593 nm wave length. Out-coupling was measured by placing large detectors close to the top surfaces.

Figure 5-8 shows the out-coupling from a 1D prismatic structure with a planar light source. This simulation represents the 2D geometrical optical analysis done in the previous sections. The out-coupling efficiency in planar 2D devices would be equivalent to the fraction of its critical angle. The lower values seen in the figure is because of some absorption at the back surface of the substrate. The out-coupling efficiency increases with increase in the inclination ( $90^\circ - \alpha$ ) of the surface. It should be noted that the maximum in efficiency is achieved when the inclination of the triangular faces equals the critical angle of the substrate i.e. when  $(90^\circ - \alpha) = \theta_c$ . At this inclination, the direct out-coupling from region I at 1<sup>st</sup> incidence is low and most of the rays beyond the critical angle is reflected to region II for 2<sup>nd</sup> incidence. The ray dynamics is similar to that shown in Figure 5-3(B). After subsequent reflection from region II and from the back surface maximum rays are out-coupled. If the ray dynamics of region II is resolved, maximum out-coupling coverage will be seen when  $(90^\circ - \alpha) = \theta_c$ . At this surface inclination, most of the rays are out-coupled only after reflection from the absorptive back surface. The decrease in out-coupling at surface inclination of  $45^\circ$  is because of the wave-guiding caused by the redirection of rays in same direction after reflections as discussed previously. Though the out-coupling increases for higher inclinations, the reentry of rays

back into the device by ray bending from the triangular structure again entraps the rays and keeps the out-coupling efficiency low. It can also be seen that this re-entrapment of rays is higher in steeper structures.

Figure 5-9 shows the simulation done using a 3D isotropic emission source on a substrate with conical, pyramidal and prismatic array on the top surface. The effect of three dimensionality of the emission source is strikingly visible from the figure. Only the 1D array of prismatic structure showed wave guiding specific to  $45^\circ$  inclination where as in conical and pyramidal arrays, there is no wave-guiding specific to surface inclination of  $45^\circ$ . The out-coupling efficiency initially increases with increase in inclination till  $30^\circ$ , and then rate of increase flattens out till  $\sim 50^\circ$  inclination after which the out-coupling decreases. The decrease at higher inclinations is again because of ray redirection back into the device. There is no evident dependence of inclination for maximum efficiency on the critical angle of the substrate. For all the substrates, inclination of  $\sim 50^\circ$  showed the highest efficiency. Both the conical and pyramidal array showed similar out-coupling efficiencies at same inclination and area coverage. Similar simulation results were obtained by Lee et al. for GaN based LED with pyramidal array on top.<sup>96</sup> In their work, the decrease in efficiency was observed for pyramidal array with side inclination greater than  $70^\circ$ . Similar to 2D simulations (Figure 5-8), the out-coupling efficiency decreases with increase in the refractive index of the substrate. As mentioned earlier the back surface of the substrate was 80% reflective, this was realized in simulation by reducing the energy of all rays incident on the back surface. It was noticed during simulations that almost same number of rays are incident on the receivers with most of the surfaces, though the energies of these rays were different. Lower energy of out-coupled rays is

what resulted in lower extraction efficiency. Since multiple reflection leads to lowering of ray energy, the total number of reflections needed for out-coupling must be lowest for maximum efficiency structures.

### **Summary**

Surface texture has been regularly used in LEDs and OLEDs to improve light extraction. Numerous photon randomization or scattering techniques e.g. surface roughening through various techniques, deposition of a layer with particles to act as light scatterer etc. have been used previously. The above geometrical analysis and simulations show that there is a regular ray dynamics and not just photon randomization behind the increased out-coupling from periodic inclined structures. The ray dynamics of inclined wall structures enhances the probability of escape after every reflection, making it a better alternative to surface roughening which completely relies on photon randomization. Our work shows that inclination of  $45^\circ$  should be avoided for one-dimensional structures on the surface where as for two-dimensional conical or pyramidal structures maximum out-coupling will be achieved with an inclination of  $\sim 50^\circ$ . In an absorption-less device, all the rays will be out-coupled after multiple reflections. In real devices, the absorptions in the device, in the active layer, substrate or at the contacts limits the out-coupling efficiency. The surface structure which reduces the total number of back reflections will give the highest out-coupling efficiency.

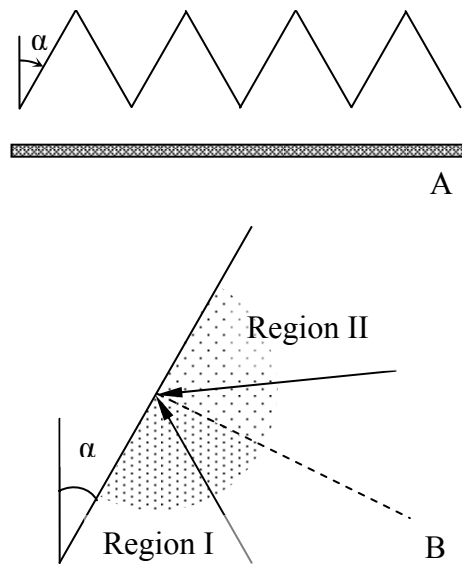


Figure 5-1. Surface texture analyzed by geometrical optics in this work A) triangular inclined wall structure B) two regions of photon incidence for the convenience of geometrical arguments in the analysis.

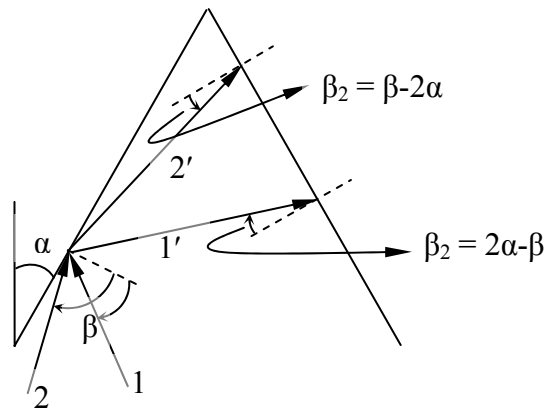


Figure 5-2. Ray dynamics after 1<sup>st</sup> reflection from region I. Rays in region I beyond  $\theta_c$  to surface normal being internally reflected to surface with opposite inclination. The reflected rays can lie in both region I and II with an incident angle of  $|2\alpha - \beta|$ .

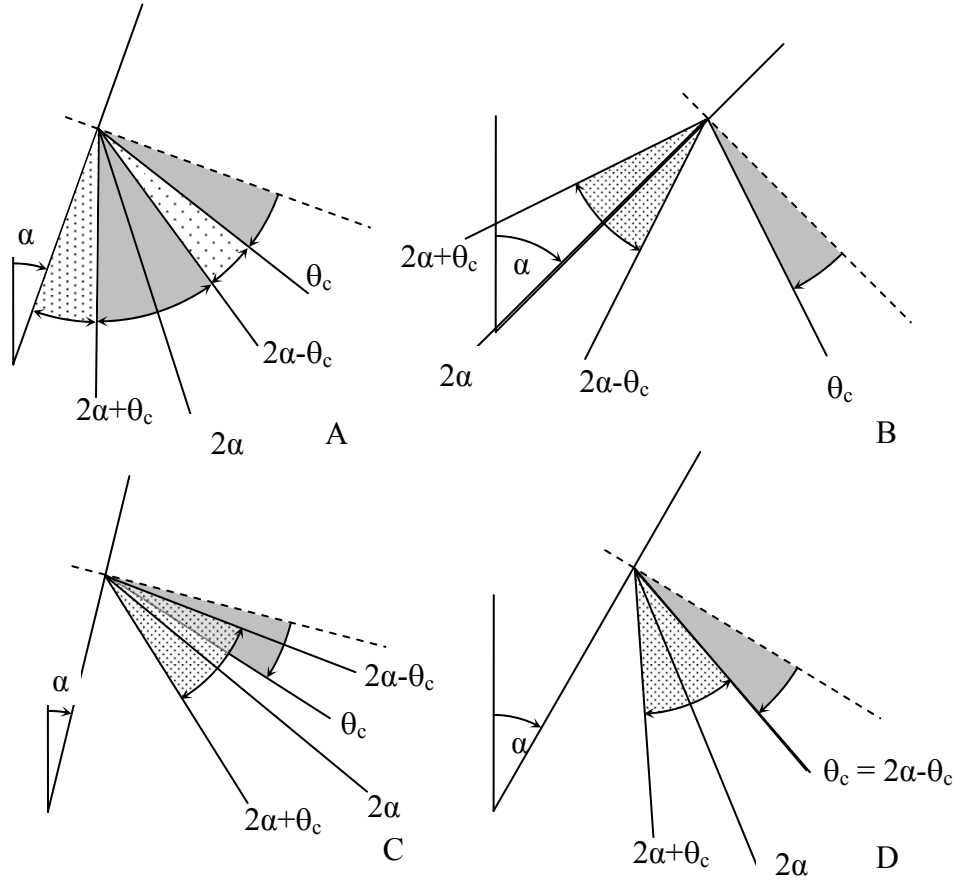


Figure 5-3. Various out-coupling zones in region I A) schematic showing various out-coupling zones in region I B) out-coupling zones when  $\alpha$  is large, the angular coverage can be observed to decrease C) out-coupling zones when  $\alpha$  is small, the angular coverage decreases in this case because of overlap of two out-coupling zones D) maximum angular coverage achieved when  $\theta_c = 2\alpha - \theta_c$  or  $2\alpha + \theta_c = \pi/2$ , first condition of maximum angular coverage is shown in figure.

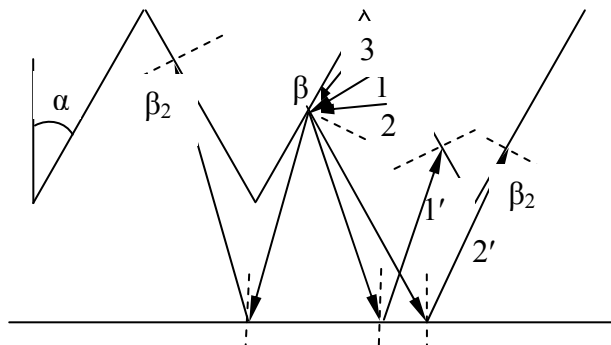


Figure 5-4. Ray dynamics after reflection from region II. Rays after reflection from back surface can incident on both faces. Ray 1 and 3 after reflection is incident on face with opposite inclination where as Ray 2 is incident on face with same inclination.

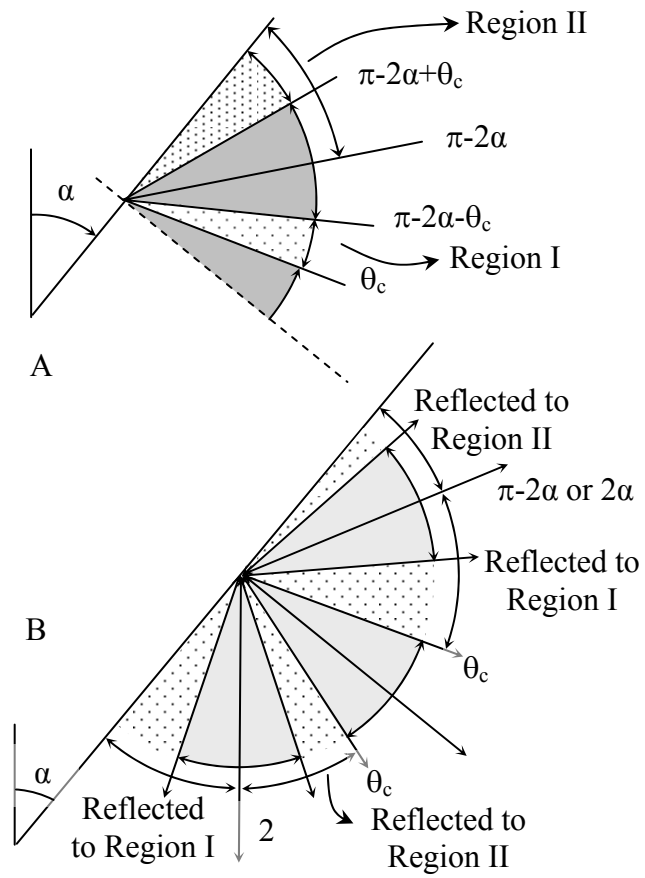


Figure 5-5. Various out-coupling zones in region I and II A) out-coupling zones in region II B) out-coupling zones from both Regions I and II.

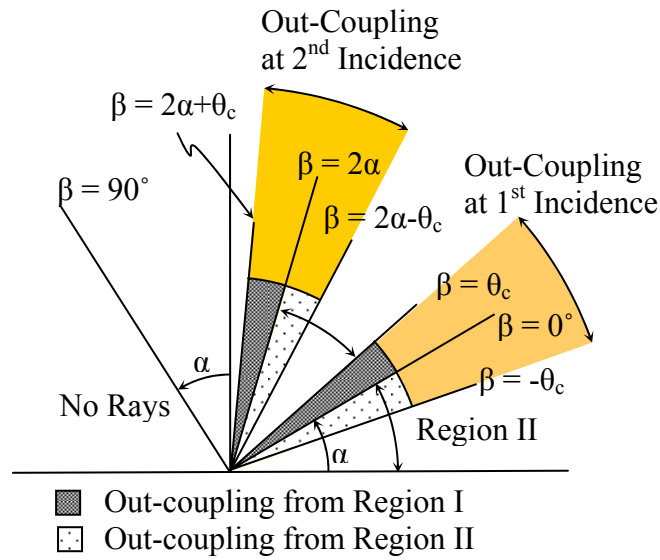


Figure 5-6. The different regions of out-coupling for surface inclined towards left from the perspective of angular distribution in the substrate layer.

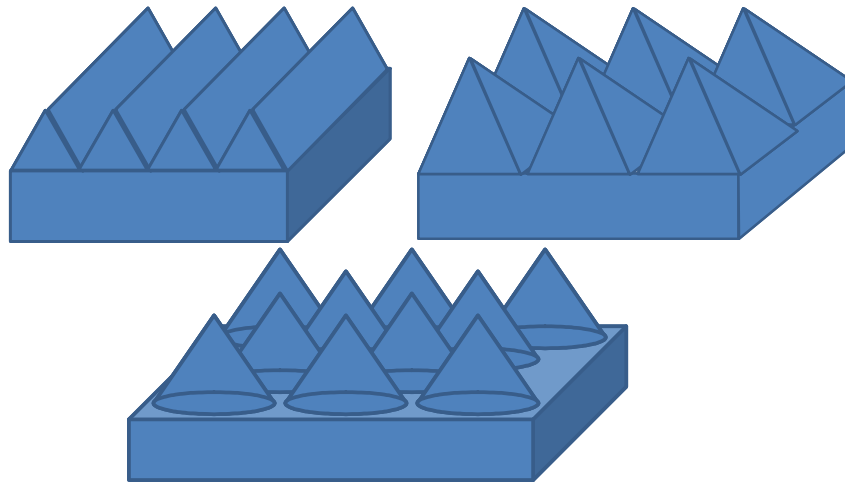


Figure 5-7. Substrates with different top surface textures simulated in our study.

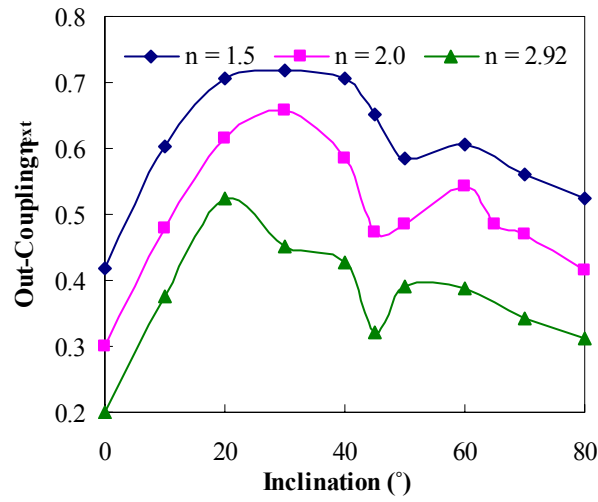


Figure 5-8. Two dimensional ray tracing simulation on a substrate with prismatic structure on top and an isotropic planar light source.

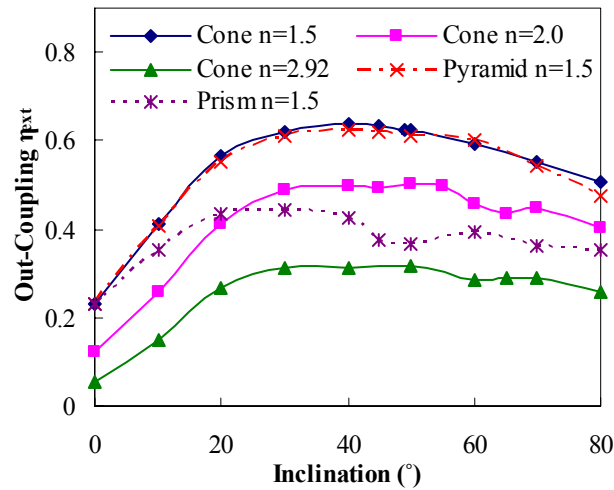


Figure 5-9. Three-dimensional ray tracing simulation on substrates with conical, pyramidal and prismatic structures on top surface. All the textures had area coverage of 91% with base diameter/length of 20 $\mu$ m.

## CHAPTER 6 ANALYSIS OF LIGHT OUT-COUPLING FROM MICROLENS ARRAY

External efficiency of LEDs, OLEDs and other thin film light emitting devices is limited primarily by the out-coupling efficiency of the device. High refractive index of the active layer causes total internal reflection and wave-guiding of a major portion of generated light. Microlens array has been known to be effective in enhancing the out coupling efficiency. In this work we have studied the efficacy of microlens arrays of different aspect ratios, the effect of absorption and substrate refractive index using ray tracing simulation. Microlens arrays leads to extraction of a portion of photons outside the escape cone at the cost of reduced extraction from within the escape cone. Multiple reflections from the back surface increase the overall out-coupling. Increase in aspect ratio of microlenses reduces the number of back reflections required for out-coupling hence reducing the absorption and enhancing efficiency. Microlens arrays give better uniformity in angular distribution of intensity. High index substrates have huge potential to enhance out-coupling but can only be realized in low absorption conditions.

### **Introduction**

External efficiency of LEDs, OLEDs and other thin film light emitting devices is limited by the out-coupling efficiency or extraction efficiency. The high refractive indices of the active layer lead to total internal reflection and wave-guiding of a major portion of generated light. The higher the refractive index the smaller is the escape cone defined by the critical angle for total internal reflection. Out-coupling efficiency has been improved by opening of higher number of the six escapes cones for each direction (lateral and vertical) by use of thick transparent substrates, shaping of LED chips or by reducing wave-guiding through modification of various interfaces in the device.<sup>17-52</sup> Interface

modification induces photon randomization there by giving multiple chances to photons to escape upon subsequent reflections. Photon randomization has been achieved by simple interface roughening<sup>5</sup> or by having regular patterned structures at various interfaces e.g. bragg gratings,<sup>9</sup> micro-rings,<sup>10</sup> photonic crystals,<sup>11</sup> microlenses,<sup>12</sup> micro-pyramids,<sup>13</sup> etc.

Microlens array has been shown to increase the efficiency by 1.5 to 3 folds in LEDs and OLEDs.<sup>12, 80-96</sup> Microlens of different diameter, aspect ratio, and area coverage has been applied to improve the out-coupling efficiency. Reportedly, the out-coupling efficiency improves with increase in aspect ratio of microlenses and is largely independent of the microlens diameter for same aspect ratio and area coverage.<sup>82</sup> The mechanism of efficiency enhancement by use of microlens array is ambiguous, apart from suggestions that it leads to randomization of photons and out-couples some wide angle rays from the substrate layer. Photon randomization, be it through surface structures like microlens array or surface roughening, all rely on photon redirection and reflection from the back surface. Surface roughening has the advantage of the availability of numerous techniques to roughen surfaces of most materials. Surface roughening has been applied to a wide variety of LED and OLED surfaces, e.g. AlGaAs, AlGaN, InGaP, GaN, SiC, sapphire etc. But the total random nature of photon dynamics imposes a limit on its efficacy. Regular periodic structures particularly microlens arrays suffer with the disadvantage of not having a versatile fabrication technique applicable to a wide variety of materials. Most of the research with microlens array has been done on OLEDs where the microlens arrays were fabricated from polymeric materials using some molding techniques. These polymeric microlenses works well with OLEDs because of similar

refractive index of glass substrate but are of limited effectiveness in LEDs where substrates have much higher refractive indices. Formation of microlens array whether polymeric or inorganic is more challenging and costly than most surface roughening techniques. The advantage of microlens arrays over surface roughening is not clear though the systematic dependence of out-coupling enhancement on lens parameter does indicate towards a more organized ray dynamics. The mechanism of out-coupling by microlens arrays needs to be explored to establish its efficacy over other randomization techniques. The use of microlens array not only enhances the light out-coupling but also changes the angular intensity distribution which otherwise is lambertian for a planar device. In this work we have studied the out-coupling and angular distribution of intensity as a function of lens parameter, substrate refractive index and absorption in the device through ray tracing simulations upon use of microlens arrays as external out-coupler.

### **Device and Simulation Parameters**

Figure 6-1 shows the schematic of the device simulated in our study. It consist of a high refractive index active layer (thickness,  $t \sim 2 \mu\text{m}$ , refractive index,  $n \sim 1.93$ ) on a glass substrate ( $t = 1 \text{ mm}$ ,  $n = 1.515$ ). The device size was  $2 \text{ mm} \times 2 \text{ mm}$  with reflecting sides. The top surface of the glass substrate was textured with microlens arrays of diameter  $20 \mu\text{m}$  with different aspect ratios. The bottom surface of active layer was assumed to have a reflective contact with different absorptions. The substrate-active layer interface was optically smooth with 100% transmittance. Fresnel losses were considered at the substrate-air interface. In LEDs, OLEDs and thin film phosphor devices, there is a substrate with an active layer grown on it. In most cases substrate has a lower refractive

index than the active layer. Typically, the substrate/active layer interface is smooth due to the requirements of thin film growth. A reflector, either a metallic mirror or a Bragg reflector is put at the bottom of the device. Usually, the emission from the active layer is believed to be isotropic. The device in simulation represents a simplified LED/OLED structure. The refractive index, absorption and other material properties will vary with different devices but the fundamentals and ray dynamics will remain similar to that explored using the simulations. Monte Carlo ray tracing simulations were done for a million rays generated with random directionality in the active layer. All simulations were done for light with 593 nm wave length. Out-coupling was measured by placing large detectors close to the surfaces, whereas angular distribution of intensity was determined by placing a far-field detector centered on the glass substrate. Absorption at the interface was realized by proportionally reducing the power of all rays incident on the surface. Both planar and far-field detectors measured the power of the out-coupled rays. Aspect ratio of the microlenses was varied by varying the contact angle between 0 to 90°. Refractive index of the substrate was changed to 1.7 and 1.93 to study the effect of substrate refractive index.

## **Results and Discussion**

### **Effect of Microlens contact angle and substrate refractive index**

Classically the amount of light transferring from one medium to another has been calculated as the fraction of solid angle subtended by the escape cone at the interface provided the light generation is isotropic in the optically dense medium. It is given by

$$\eta = \frac{1}{2} \left( 1 - \sqrt{1 - \left( \frac{n_2}{n_1} \right)^2} \right) \quad (6-1)$$

where  $n_1$  and  $n_2$  are refractive indices of the medium. Accordingly, a planar device with  $n_{\text{sub}}/n_{\text{act}}=1.5/1.93$  would have 14.4% light out-coupling from top and bottom, 61.9% light wave guiding in the active layer where as the rest 23.7 % wave-guided in the glass substrate. The out-coupling efficiency increases with the use of external out-couplers and the cumbersome nature of ray dynamics necessitates simulation and experimental studies instead of an analytical approach. Figure 6-2 shows the out-coupling efficiency of the device with increase in the contact angle of the microlenses. Initially there is a steep increase in the out-coupling from planar to microlens surface, there after the out-coupling was found to increase linearly with contact angle. As previously reported, maximum out-coupling enhancement was observed for hemispherical microlenses, approximately an increase of 1.35 fold. Möller et al. observed experimentally an increase of 1.5 fold where as their 1D simulation predicted 2.3 times increase. The lower experimental enhancement was reportedly because of the imperfect nature of microlenses. We believe that the 1D nature of simulation led to an overestimation of enhancement in efficiency. The experimental enhancement otherwise is close to our result with some effect of imperfect microlenses. The increase in enhancement came from reduction in wave-guiding in the substrate layer where as the wave-guiding in the active layer remained constant. In LEDs and OLEDs, the active layer has the largest refractive index and hence leads to a major portion of wave-guiding losses. Among possible ways of reducing wave-guiding in the active layer is to either modify the substrate/active layer interface or by use of a high refractive index substrate. The high refractive index substrate would increase the substrate mode from where the light can be out-coupled by use of external out-couplers e.g. microlenses. The increase in out-coupling with different substrates ( $n=1.7, 1.93$ ) is

shown in Figure 6-2. The use of substrate with a refractive index of 1.7 significantly increased the light out-coupling over lower index substrate for same contact angle microlenses. High refractive index substrate reduces the wave-guiding in the active layer. Out-coupling was increased further when the refractive index of the substrate matched with that of the active layer. There would be no wave-guiding specific to the active layer in such a case and the angular intensity at the microlens surface would be isotropic, instead of lambertian in case of a refractive index mismatch. Nakamura et al. studied the effect of substrate refractive index on out-coupling with micro-pyramidal array as external out-coupler.<sup>92</sup> Contrary to our result, enhancement with increase in substrate refractive index was not observed. In a planar device the higher amount of rays in the substrate will not result in any efficiency enhancement because of the reduced critical angle (escape cone) at the substrate/air interface. For non-planar substrate/air interface, out-coupling depends on multiple reflections; the decrease in escape cone at the substrate/air interface is more than compensated by multiple reflections from bottom surface. The lack of enhancement with the use of high refractive index substrate was most likely due to high absorption of the reflected rays particularly by the absorptive metal contact in their device.

Figure 6-3 shows the ratio of out-coupled power to that of total power in the substrate mode ( $\eta_{\text{ext}}/\eta_{\text{sub}}$ ) for different microlenses and substrates. Since an external out-coupler only helps in extraction of substrate mode rays, the ratio  $\eta_{\text{ext}}/\eta_{\text{sub}}$  is a better way to determine the efficiency of microlens array. It is interesting to note that higher proportion of substrate mode rays are out coupled when substrate refractive index is low, though the overall out-coupling is higher for high refractive index substrates. Higher

percentages of substrate mode rays are getting absorbed with increase in substrate refractive index. Use of high refractive index substrates increases both the out-coupling and absorption of substrate mode photons at the cost of active layer mode. Since the absorption is only occurring at the back surface it can be inferred that with increase in refractive index more reflections per photon is needed for out-coupling. Higher number of reflections required is probably because of the small substrate/air critical angle and hence smaller escape cone for high refractive index substrates. This is in contrast to planar devices, where out-coupling is only dependent on the refractive index of the active layer, the refractive index of substrate layer being immaterial. The increase in out-coupling with increase in the microlens contact angle also implies fewer reflections towards active layer for out-coupling. Hemispherical microlens gives highest out-coupling by having fewer back reflections. This control of the number of back reflection is not possible in case of photon randomization techniques like surface roughening. The curves in Figure 6-3 also shows that there is an overall limit to the efficacy of microlens arrays dependent on the reflectance from the active layer.

Our simulation work shows the sensitivity of efficiency increases with increase in back absorption. Since microlens array work on multiple reflections, efficiency was found to be less sensitive to area coverage for a reflective active layer stack. The enhancement of efficiency with increase in diameter (area coverage) reported by Peng et al.<sup>82</sup> indicates to highly absorptive back contact in their device.

### **Angular Distribution of Intensity**

Figure 6-4 shows the variation in far-field angular distribution of intensity with different microlens arrays on the device. The intensity distribution has changed

drastically compared to the lambertian intensity profile of a planar device. Angular distribution of rays from a microlens covered surface has not been studied in detail previously, particularly its variation with lens parameters. For surfaces with microlens contact angles of  $25^\circ$  and  $45^\circ$  the enhancement mostly comes from extraction of rays from higher angles, but with increase in contact angle the intensity in forward direction also increases. The inset figure shows a uniform intensity in forward direction from microlens covered surface. The extent of this circular symmetry, also reported by Greiner<sup>13</sup>, decreases with increase in the contact angle of the microlenses. The intensity increase from angles closer to the lateral direction is not as prominent as reported by Moll er et al.<sup>80</sup> It is the enhancement from intermediate and forward angles which mostly enhances out-coupling. To better understand the ray dynamics when microlenses are used, the back reflector was replaced with a smooth, transparent optical surface in the model. Figure 6-5 shows the far-field angular distribution of intensity from both the front and back surfaces of such a device. The figure shows (i) increase in out-coupling from both sides with increase in microlens contact angle and (ii) dominant increase in intensity from microlens surface at intermediate angles in forward direction which varied with the contact angle. The intensity distribution from the microlens surface is seemingly a superposition of a peak intensity at intermediate angle over a lambertian distribution. Microlens with a lower contact angle of  $25^\circ$  has angular distribution similar to planar device in the angle range  $0-50^\circ$ , beyond  $50^\circ$  it shows a spike in intensity. As the contact angle increases the maximum intensity progressively moves closer to vertical as seen in the inset figure. The emission from the back surface consists of rays generated within  $\theta_{c \text{ active/air}}$  and rays reflected back by the microlenses within  $\theta_{c \text{ sub/air}}$  in the substrate layer.

Apart from rays out-coupled at first incident, the emission from front surface consists of rays reflected back but outside  $\theta_{c \text{ sub/air}}$  from the microlens surface. The spike in intensity seen in the emission from microlens surface is from the extraction of rays traveling outside  $\theta_{c \text{ sub/air}}$  in the substrate layer. The rays out-coupled from back surface when directed upward using a reflector enhances the out-coupling primarily in the forward direction (Figure 6-4), drowning the spike in intensity and providing the circular symmetry to the intensity distribution.

### **Photon Dynamics**

The mechanism of enhancement through surface texturing has mostly been said to be photon randomization. The random reflection from textured surfaces provides multiple chances to photons to escape. As seen from Figures 6-2 – 6-4 microlens array covered surface shows a systematic out-coupling enhancement and angular dependence on the contact angle not likely for a total randomization process. To study the mechanism of light extraction from microlens arrays, photons were incident on the microlens surface from within the substrate at different angles. Figure 6-6 shows the percentage out-coupling for various incident angles on different microlens surfaces when no reflection from the bottom surface was allowed (100% absorption). Within the escape cone, from where rays are out-coupled in a planar device, the percentage of rays extracted decreases with increase in the contact angle of the microlens. Whereas for rays outside the escape cone the portion extracted is increasing with increase in contact angle of the microlenses. It can also be seen from the figure that when absorption of the back side was reduced from 100% to 50% to 20% for hemispherical microlens array, the intensity of photons extracted from within the escape cone increasingly came closer to that of a planar

surfaces. The rays outside the escape cone are also largely extracted. It indicates that the reduction in extraction of light from within the escape cone compared to planar device is mostly compensated by multiple reflections from the back side whereas the enhancement is coming from the extraction of rays outside the escape cone. The increase in efficiency with contact angle, shown in Figure 6-2, shows that fewer reflections are needed for out-coupling as the contact angle is increased. It is also clear that the extraction efficiency of photons within the escape cone is higher than rays outside the escape cone even for microlens covered surface. It can be implied that microlens apart from directly extracting high angle rays, also focus rays from outside the escape cone within the escape cone.

### **Effect of Absorption**

Figure 6-7 shows the enhancement in out-coupling from hemispherical microlens array with different absorptions at the back surface. It should be noted that when the back surface is 100% absorbing the increase in out-coupling efficiency is nominal, implying that the decrease in the out-coupling of rays within the escape cone is almost equivalent to the extraction of high angle rays for all the substrates. As the absorption at the back surface is reduced (reflectance increased) the out-coupling starts to increase. The increase in out-coupling with decrease in absorption is much steeper for substrates with high refractive index. High refractive index substrates having lower critical angle at the air/substrate interface reflects back a higher proportion of rays towards the active layer. The high reflection from microlens surface, hence higher absorption is compensated by the higher number of rays in the substrate mode and leads to an overall increase in efficiency. The difference in out-coupling efficiency with refractive index of substrate is increasing with decrease in absorption. It shows high absorption to severely impair the

effectiveness of high refractive index substrates. Simulation work done on external out-couplers like microlens and micro-pyramids by Greiner<sup>13</sup> showed that in external out-couplers the efficiency of direct emission decreases and is compensated by increase in efficiency of high angle emission and by enhancement due to multiple reflections. Our simulation support the finding of Greiner<sup>13</sup> that the reflectance from the active layer stack is paramount, since these structures depend on multiple reflections to enhance out-coupling.

### **Conclusions**

Light out-coupling from devices using microlens array as external out-coupler was analyzed. Microlens array enhance efficiency both by extracting rays lying outside the escape cone and also by redirecting a portion within the escape cone at subsequent reflection. The number of back reflection required for out-coupling reduces with increase in the aspect ratio of microlenses. The reduced reflection leads to less absorption of rays and hence increased efficiency for hemispherical microlenses. Microlens array give better uniformity in angular distribution of intensity. High index substrates have huge potential to enhance out-coupling but can only be realized in low absorption devices.

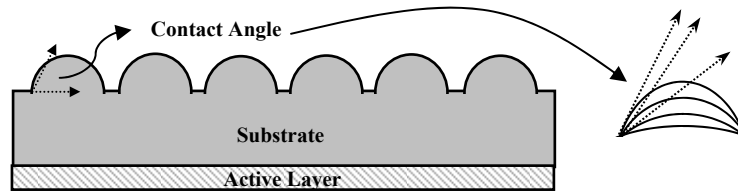


Figure 6-1. Device used for ray tracing simulations. The active layer was 2  $\mu\text{m}$  thick where as the substrate was 1 mm in thickness. Top surface of the substrate was covered with microlens array of various contact angles, 20  $\mu\text{m}$  diameter and 58% area coverage.

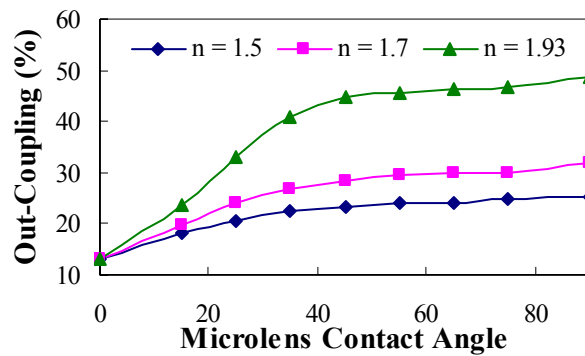


Figure 6-2. Out-coupling efficiency with increase in microlens contact angle for different substrate refractive index. Hemispherical microlens array shows maximum efficiency for all substrates.

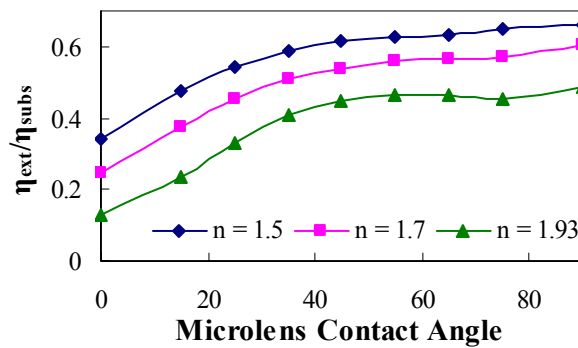


Figure 6-3. Enhancement relative to the substrate mode photons for different refractive index substrates. With increase in substrate refractive index, more photons are extracted from active layer mode to substrate mode from where out-coupling is possible because of microlens array.

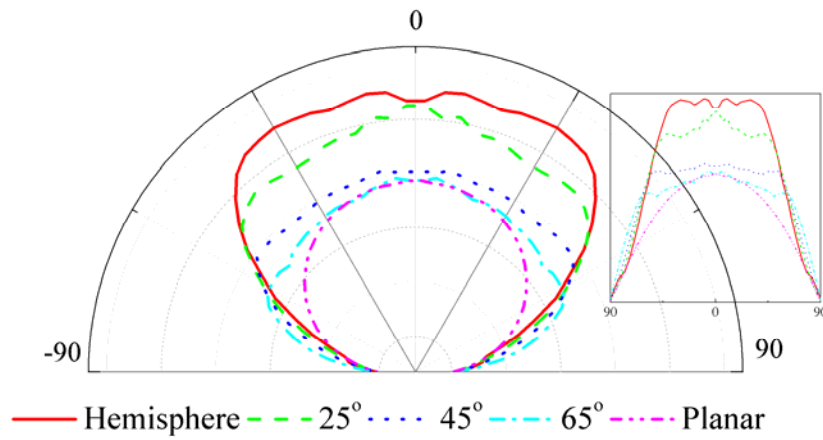


Figure 6-4. Angular distribution of intensity for a device with 80% back surface reflectance. Uniformity in angular distribution in forward direction which reduces with increase in contact angle can be seen from the figure.

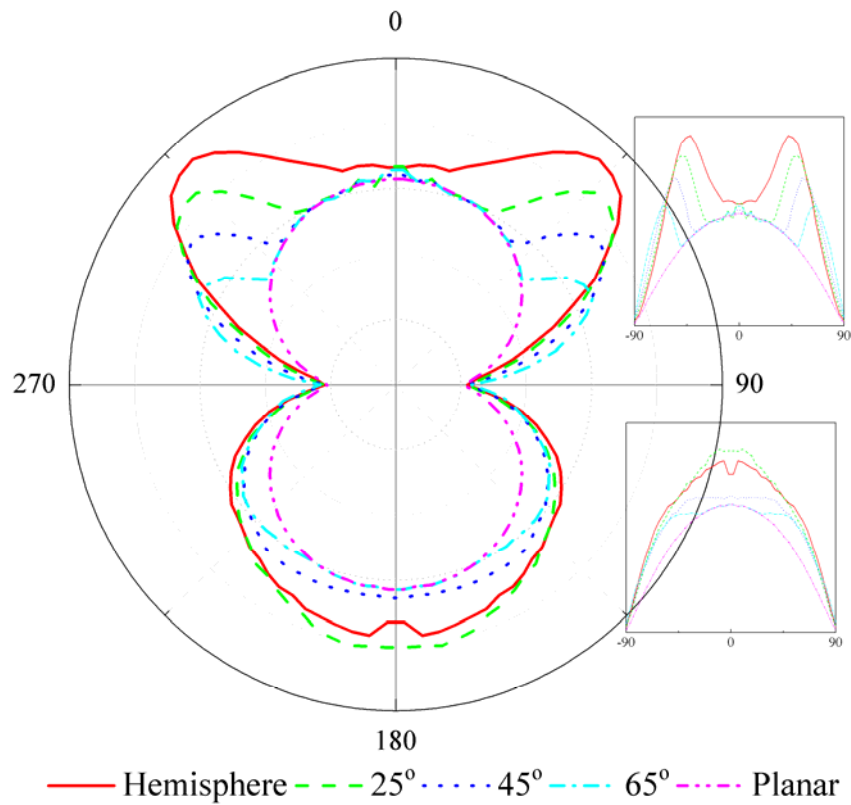


Figure 6-5. Angular distribution of intensity when the back surface is optically transparent.

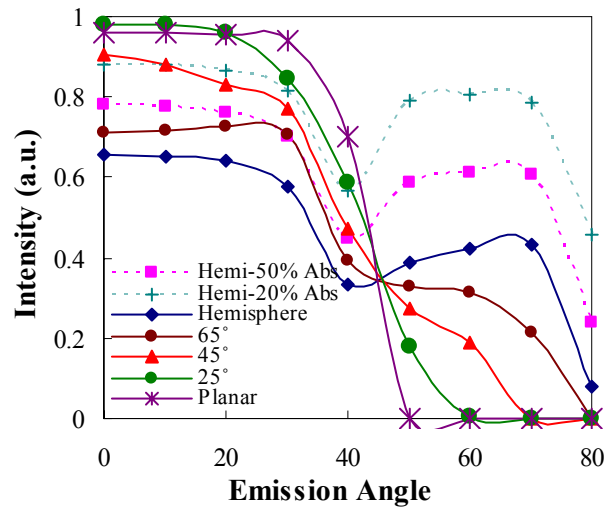


Figure 6-6. Out-coupling efficiency vs. directionality of photons in the substrate. For solid curves the back surface was 100% absorbing. Absorption was then reduced to 50% and 20% for hemispherical microlenses to study the effect of multiple reflections on out-coupling of directional photons.

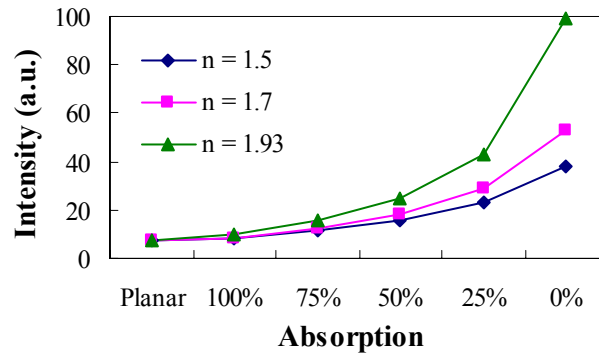


Figure 6-7. Out-coupling efficiency for hemispherical lens as a function of back absorption for different substrate refractive index.

## CHAPTER 7 TIME DEPENDENT CURVATURE CONTROL USING CHEMICAL MECHANICAL POLISHING

Chemical mechanical polishing (CMP) is a standard IC fabrication technique used in both front-end and back-end of line for planarization of wafers. Up till now research has been focused on reducing the non-planarizing aspects of CMP such as edge rounding, dishing etc. In this study we have investigated the phenomena of edge rounding for its potential for creation of different topographies. The effect of CMP variables: pad and pressure were studied by polishing patterned wafers with Politex™ (soft) and IC1000/Suba IV stacked (hard) pad at different pressures. The surface evolution dynamics during polishing has been discussed based on contact mechanical model for CMP.

### **Introduction**

In the last couple of decades CMP has grown from a glass polishing technology to a standard IC fabrication technique. Chemical Mechanical polishing ensured the miniaturization of integrated circuits by providing an appropriate copper removal technique and also providing flatter wafer surfaces for next generation lithographic tools. CMP technology is used in both front-end and back-end processes, in shallow trench isolation (STI), inter-level dielectric planarization, local tungsten interconnects, and copper damascene.<sup>97</sup> It is finding application in wafer planarization of non-silicon semiconductor materials e.g. wide band gap semiconductors like SiC, GaN for providing damage free substrates.<sup>98-100</sup> Research and development in CMP has almost totally been towards achieving a better local and global wafer planarity, lower defectivity and damage-free surface, which are the fundamental needs of the semiconductor industry.

Owing to this, chemical-mechanical polishing has become synonymous with chemical-mechanical planarization. Non-planarizing phenomenon such as dishing and edge rounding are categorized as defects and efforts have been made to reduce or eliminate these defects. These non-planarizing phenomenons have the possibility of creating curved surfaces, which would open a new avenue for chemical mechanical polishing, that of a surface shaping process.

The material removal rate during CMP depends on the applied pressure, linear velocity, the characteristic of the polishing medium (pad and slurry) and the wafer material. Among these, applied pressure and the properties of the pad are the parameters which affect the contact pressure during CMP. Material removal at any location in the wafer is directly proportional to the contact pressure it experiences.<sup>101</sup> Contact pressure is uniform for a feature-less flat wafer whereas for a wafer with high and low elevation features it varies along the wafer.<sup>102-106</sup> Polishing pad and wafer when brought together under an applied pressure leads to deformation of the pad along the features on the wafer. The local deformation of the pad determines the local contact pressure and hence the local removal rate. It has been observed that the initial removal rate at the edges/corners of a step feature during chemical mechanical polishing is high leading to the rounding of edges. Patrick et al. observed the polishing rate of a step feature (rate of height reduction) to progressively decrease during a CMP process.<sup>102</sup> The decrease in polishing rate was more prominent at the edge of the step and reduces towards the center. It can be inferred that as the corners were progressively rounded, the pressure at the edges decreased, leading to decrease in the polishing rate. The contact pressure was dynamic and changed continuously during polishing with change in the topography of the surface. Chekina et

al.<sup>103</sup> and Saxena et al.<sup>104</sup> based on two dimensional contact mechanical model for CMP of a step feature predicted a reduction in variation in contact pressure with the progression of CMP, until a steady state was reached. The surface shape reached equilibrium in their model where further polishing did not change the surface topography.

It is generally agreed that the above phenomena is due to the conformal nature of the polishing pad, and that softer pads lead to more edge rounding than harder pads.<sup>103,104</sup> In literature, various other reasons have been attributed to higher polish rate at the edge of a step feature. Runnels, on his flow based feature scale model reasoned the rounding to occur because of high stress generated at the corners by the flowing slurry.<sup>105</sup> Patrick et al. attributed it to the pressure enhancement at the leading edges of the step feature due to the relative motion of the wafer and pad.<sup>102</sup> Chekina et al. based on contact mechanics model suggested that the high initial contact pressure at the corners due to bending of the pad causes edge rounding.<sup>103</sup> In this work we have studied surface shaping using edge rounding phenomena and the effect of CMP variables on the dynamics of surface evolution. Non-planarizing aspects of CMP, steady state as well as non-steady state, can be used to shape surfaces with applications in opto-electronics, tribology etc.

### **Experimental Procedure**

Plasma enhanced chemical vapor deposition (PECVD) silicon oxide, 1  $\mu\text{m}$  thick was deposited on 1 inch<sup>2</sup> coupons of soda lime glass. Silicon dioxide was deposited by flowing nitrous oxide ( $\text{N}_2\text{O}$ ) and silane (2%  $\text{SiH}_4/\text{N}_2$ ) gases at a flow rate of 1420 and 400 sccm, respectively. The glass coupons were heated to 300°C while the chamber pressure was maintained around 550 mTorr. Power was kept at 60 W at a frequency of 187 kHz for formation of low stress silicon oxide. The  $\text{SiO}_2$  layer was patterned using Microposit

S1813 photoresist and standard UV photolithography using a Karl Suss MA6 Aligner with a 365 nm Hg i-line radiation. The pattern consisted of hexagonal arrangement of circular dots of 20  $\mu\text{m}$  diameter and 1  $\mu\text{m}$  spacing. The samples were etched in 15 sccm  $\text{SF}_6$  and 5 sccm Ar in a Uniaxis Shuttlelock RIE-ICP reactor under 100 W DC and 600 W RF power to form cylindrical pillar-type patterns. Struers Co. TegraPol-35 with TegraForce-5 tabletop polisher was used for polishing the samples at a down pressure of 2.5, 3.6, 5.4, and 8.2 psi. Two types of pads: Politex (soft) pad and IC1000/Suba IV (hard) stacked pad supplied by Rodel Inc. were used for polishing.  $\text{SiO}_2$  slurry with 5 wt% loading and pH 4 made from dilution of Levasil 50cK with nominal particle size of 80 nm was used for polishing. Slurry flow rate of 50 mL/min was used during all CMP. The surface was characterized using a Veeco Dimension 3100 Atomic force microscopy using contact mode.

## **Results and Discussion**

Figure 7-1(A) shows the AFM image of initial surface profile of glass coupons. The cylindrical pillars were of diameter 20  $\mu\text{m}$  and  $\sim 700$  nm height with inter-pillar spacing of 1  $\mu\text{m}$ . Figure 7-1(B) shows the image of surface after polishing with soft Politex pad for 2 min. The non-planarizing phenomenon during CMP has led to formation of rounded surface profile. CMP of the above pattern was performed under different conditions to study the effect of CMP variables and the dynamics of surface evolution.

### **Effect of Pressure**

Figure 7-2(A) shows the line profile of the feature obtained after 1 min CMP using soft politex pad at different pressures. To analyze the nature of surface profiles,

parameter R has been defined. It is the radius of the circle passing through the top of the feature and point (x,y) along the profile calculated as  $R = (h^2 + r^2) / 2h$ . R is loosely related to the radius of curvature of the profile. Definition of parameter R was necessitated because of wide variations observed in the differential radius of curvature ( $R = (1 + f')^{3/2} / f''$ ) of the AFM line profiles. The corresponding variation of parameter R along the step for various line profiles is shown in Figure 7-2(B). For simplicity only one-half of the R vs. distance plot is shown. The R values are decreasing outwards from the center at all pressures. The decrease in the value of R towards the edge indicates rounding of edges. The anomalous low pressure curve is due to flatness at the top of feature caused by lower polish rate (seen in Figure 7-2(A)). It can be observed that both the best fit linear slope and the R values are decreasing with increase in polishing pressure. At higher polishing pressure the removal rate is higher, the decrease in slope and R value indicates that as more and more material is removed the rounding moves from the edge towards the center.

Figure 7-3(A) and 7-3(A) shows the line profile and the corresponding R plot after 2 min of polishing with the politex pad. There is a significant difference in the plots compared to that obtained after 1 min of polishing (Figures 7-2(A) & (B)). Significant lateral material removal can be observed in all the profiles with the initial vertical walls mostly polished away. The R curves (Figure 7-3(B)) for profiles obtained for sample polished at low pressures are horizontal where as the R values of profiles at high pressure is increasing away from the center of the feature. The slope of the linear fit to the R curves is decreasing with decrease in pressure till it becomes approximately horizontal at a pressure of less than 5.4 psi indicating a spherical curvature. The horizontal R curve of

samples polished at lower pressure is lower than those polished at higher pressures. The spherical surface profiles obtained at lower pressure has smaller radius of curvature than those polished at higher pressures. High pressure polishing would lead to curved surfaces faster but better curvature (smaller radius of curvature) and high aspect ratio structures is obtained at low pressures.

### **Effect of Pad**

Figure 7-4(A) and (B) shows the line profile and the R plot of the step feature polished using harder polyurethane IC 1000/Suba IV stacked pad for 2 min at different pressures. The slope of the R curves is negative for profiles obtained at all pressures with surface showing higher curvature at low pressures as evident from decreasing values of R with decrease in pressure. As pointed out in previous studies, softer pads being more conformal lead to more edge rounding than harder pads.<sup>102-104</sup> After 2 min of polishing using hard pad, the R curve shows similarity with 1 min polishing using softer pads with its negative slopes. Also, in contrast to Figure 7-3(A), the vertical walls remain intact when hard pad is used, only a small portion at the top of the pillar shows some curvature. It is evident that for the purpose of surface shaping a softer pad is more desirable.

### **Effect of Time**

A closer look at Figures 7-2(B) and 7-3(B) suggests that the slope of R curves starts with being negative at the start of the polishing process then slowly it becomes horizontal and then switches to being positively sloped. The time required for reaching these different stages varied with pressure. As can be observed, at a high pressure of 8.2 psi the R curve changes the slope within 2 min where as at lower pressures the R curves only became horizontal after 2 min. The increase in R value outward is probably because

of reduction of step height to an extent where the bottom surface of the step is also being polished. Further polishing in both cases reduced the step height further and eventually led to a smooth surface. The increase in the overall value of R and also the positive slope of R curve of the profile polished at high pressure (8.2 psi) for 2 min using politex pad, indicates towards this smoothening of surface after an over-polish. Surface shaping as seen above is more prominent at low pressures with softer pad where as the exact nature of the surface, i.e. the variation of R along the feature (spherical, elliptical) can be controlled by the duration of polishing.

### Discussion

Chekina et al. developed a numerical formulation for surface evolution with the progress of CMP based on contact mechanics.<sup>103</sup> According to 2D contact mechanics, the surface displacement of the pad when it is pressed in contact with a rigid wafer with step features is given by

$$w(x) = \frac{-2(1-\nu^2)}{\pi E} \sum_{i=1}^N \int_{a_i}^{b_i} p(s) \ln |x-s| ds + Const \quad 7.1$$

where  $\nu$  is the Poisson's ratio and E the elastic modulus of the pad,  $p(s)$  the contact pressure,  $a_i, b_i$  are the boundary points of the contact domain.<sup>103</sup> The surface displacement of the pad when pressed against a step feature is, as expected, dependent on the elastic properties of the pad, its elastic modulus and Poisson's ratio i.e. the conformal nature of the pad. The model steady state surface profile for a single step can be derived by integrating Equation 7.1. At steady state the removal rate at every point of the feature is same which implies a uniform contact pressure ( $p(s)$  constant) along the feature. Equation 7.1 upon integration under constant contact pressure ( $p(s)$ ) gives

$$w(x) = \frac{-2(1-\nu^2)}{\pi E} p^* a \left[ \left(1 - \frac{x}{a}\right) \ln\left(1 - \frac{x}{a}\right) + \frac{x}{a} \ln\left(\frac{x}{a}\right) + \ln a \right] + Const \quad 7.2$$

where  $p^*$  is the contact pressure which is constant through out the step,  $a$  is the width of the step. Figure 7-5(A) shows the plot of the function  $(y - 1) \ln(1 - y) - y \ln y$ ,  $0 < y < 1$  for various values of the pre-function coefficient  $K \left( \frac{2(1-\nu^2)}{\pi E} p^* a \right)$ . The pre-function

coefficient  $K$ , represents the effect of CMP variables: pad properties (elastic modulus and Poisson's ratio), down pressure and pattern width on the surface profile during CMP.

Theoretically, the possibility of achieving different steady state profiles for a particular step width by changing the CMP variables can be seen from Figure 7-5(A). Decrease in the value of  $K$ , which can be caused by high elastic modulus (hard pad) or low pressure polishing, reduces the rounding effect. Figure 7-5(B) shows the variation of parameter  $R$  along the model steady state profile for various values of  $K$ . When  $K$  is low (high elastic modulus of pad, low pressure),  $R$  decreases from the center of the step outwards. Higher  $R$  in the center region indicates a relatively flatter step polish. For a particular value of  $K$ ,  $R$  is constant throughout, which indicates a spherical curvature. At lower  $K$  values (low elastic modulus, high pressure),  $R$  is lower at the center indicating a more curved surface at the center of the step. Figure 7-5 shows a variety of surface that the modeling work predicts can be obtained by CMP at steady state. Equation 7.2 and the pre-function constant can be used to get an insight into the surfaces obtained after polishing with politex and IC1000 pads. In Figure 7-2(B), the decrease in  $R$  values outward from the center after 1 min of polishing using politex pad resembles the curves for lower values of  $K$  (Figure 7-5(B)). The lowering of  $R$  values at high pressure polishing is consistent with the fact that high  $K$  at high pressure gives more curvature. In Figure 7-3(A) the surface

after 2 min of polishing at different pressures looks similar to modeled profiles obtained for decreasing values of K (Figure 7-5(A)). This will seem like an anomaly particularly because increase in pressure increases the value of K which is opposite of what the modeled curve depicts. The similarity arises from the high removal rate at high pressures which has reduced the step height. R plots, which are a better way of comparing the nature of surface profiles, are horizontal at low pressures where as it is increasing outward at high pressures. This is similar to the trend with decreasing value of K shown in Figure 7-5(B), thus the nature of surface profile is similar to that predicted by the model. The IC1000 pad has higher modulus than the politex pad which gives a lower value of the pre-function coefficient K. Low value of K implies higher R values meaning low curvature surface. It can be observed from Figure 7-4(B) that the R values are comparatively higher when polished with hard pad than that obtained after polishing with politex pad.

The pre-function co-efficient K, along with the polishing period determines the surface obtained during CMP. The Poisson's ratio of both the pads is similar  $\sim 0.2$  where as the elastic modulus of IC1000 pad (29 MPa) is  $\sim 6$  fold higher than that of Politex Pad (5 MPa).<sup>104,106</sup> The K value for Politex will always be  $\sim 6$  fold larger than IC1000 pad for all pressures and pattern width. The pre-function coefficient (K) for a step width of 20  $\mu\text{m}$  and pressure of 2.5 psi was calculated to be 0.007 and 0.042 for IC1000 and Politex pad respectively. It should be noted that though the K value of the Politex pad is lower than those plotted in Figure 7-5, different curvatures including spherical were attained. Equation 7.2 is based on two-dimensional contact mechanics. It defines the steady state profile after CMP of a 2D step feature with equal elevated and recess width. The width of

recess in a patterned wafer would effect the deformation of the polishing pad and hence would alter the polishing dynamics. Overall, the dynamics of the polishing process, the effect of CMP variables, pad and pressure, seems to follow the modeling trends. The surface, changes throughout polishing and an intermediate state would give the desired surfaces under appropriate CMP conditions.

### **Conclusions**

We studied the non-planarizing phenomena of edge rounding for creation of surfaces with different curvatures. A softer pad with low elastic modulus at low pressures is most suited for shaping of surfaces. The dynamics of the polishing process seems to follow the contact mechanical modeling trends. The various CMP variables; pad, pressure, affect the profiles as predicted by the modeling work of Chekina et al.<sup>103</sup> Various curvatures including spherical were created by CMP at different stages of polishing. CMP, which till now has been looked at only as a planarization technique, can be used for creating different topographies for applications in tribology, opto-electronics etc.

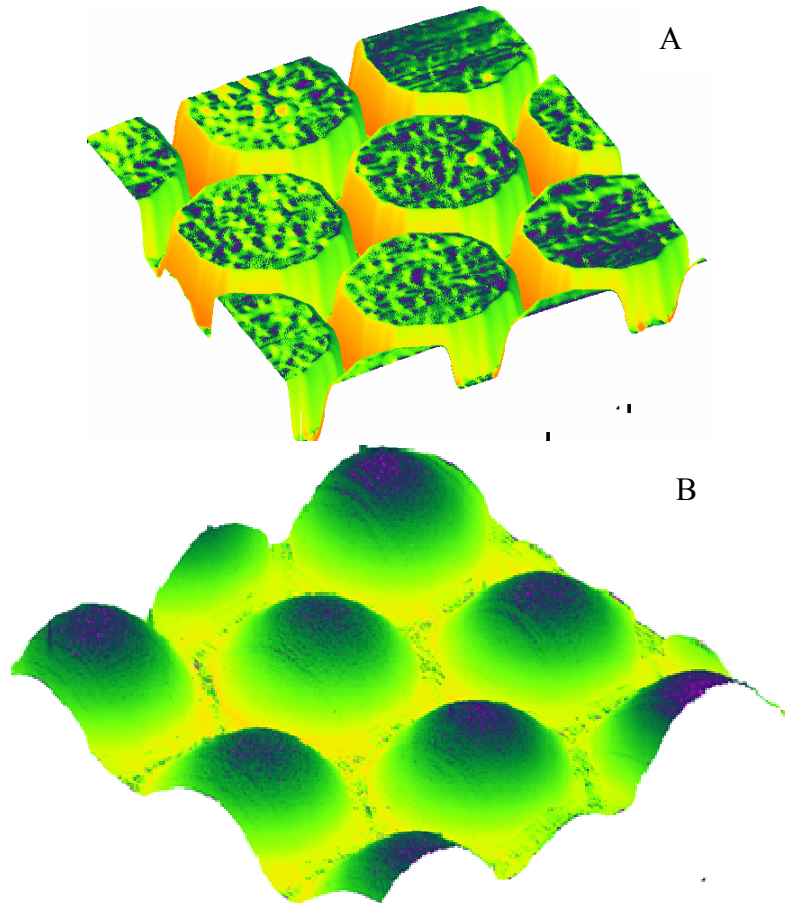


Figure 7-1. AFM image of the surface before and after CMP A) initial profile before polishing and B) after polishing with Politex™ pad for 2 min at 2.5 psi.

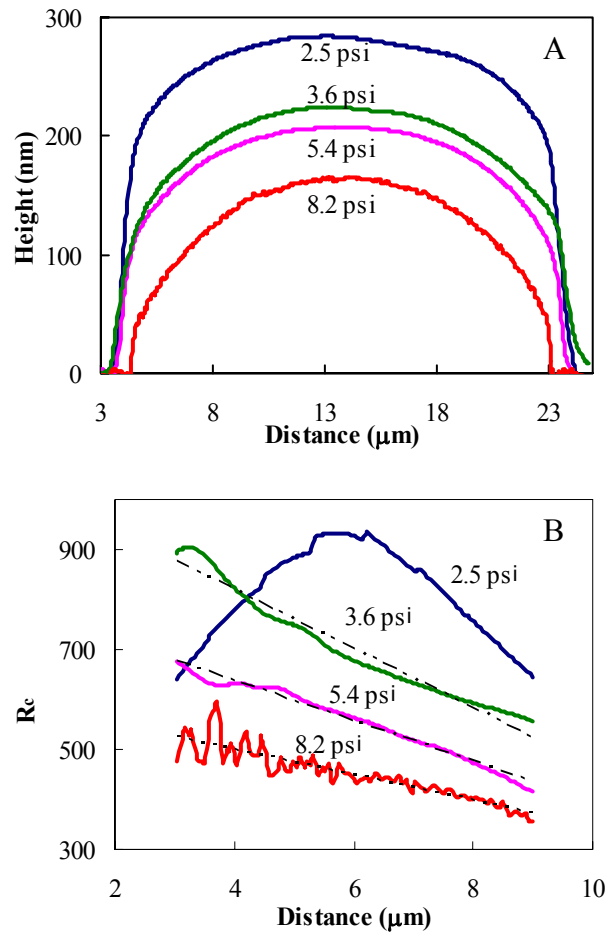


Figure 7-2. Surface profile and corresponding radius of curvature after 1 min of CMP using Politex™ pad A) surface profile obtained at different down pressures B) the corresponding R curves along with the best fit lines.

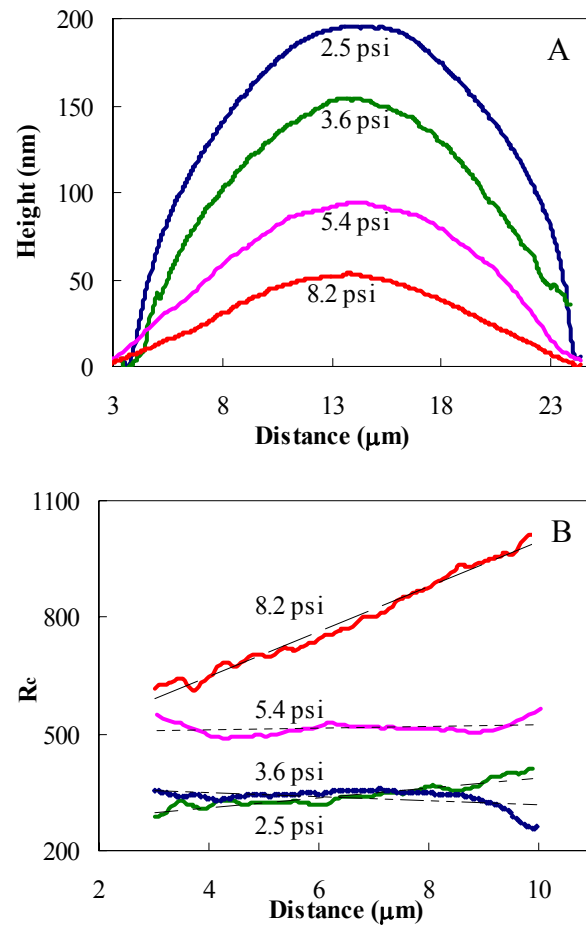


Figure 7.3. Surface profile and corresponding radius of curvature after 2 min of CMP using Politex™ pad A) surface profile obtained at different down pressures B) the corresponding R curves along with the best fit lines.

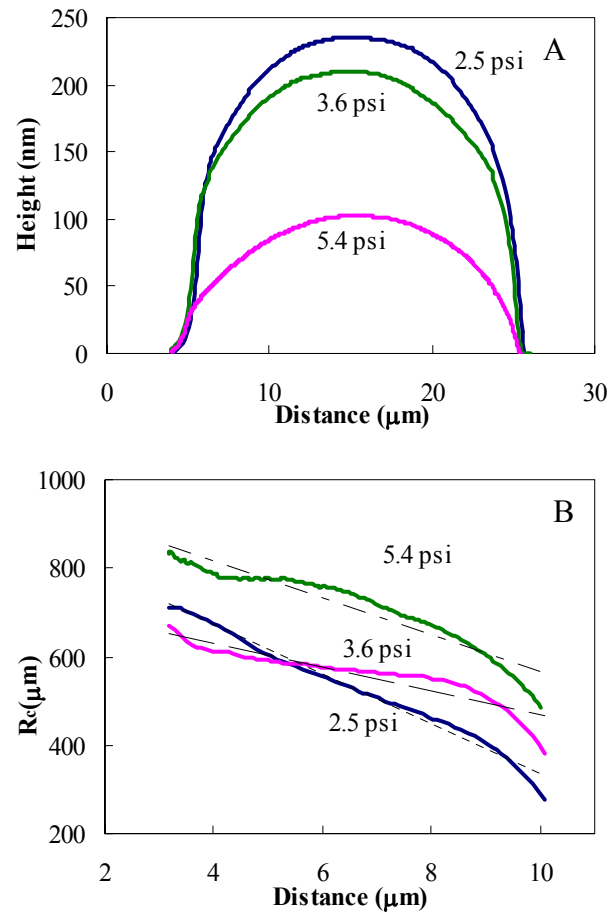


Figure 7-4. Surface profile and corresponding radius of curvature after 2 min of CMP using IC1000/Suba IV stacked pad A) surface profile obtained at different down pressures B) the corresponding  $R_c$  curves along with the best fit lines.

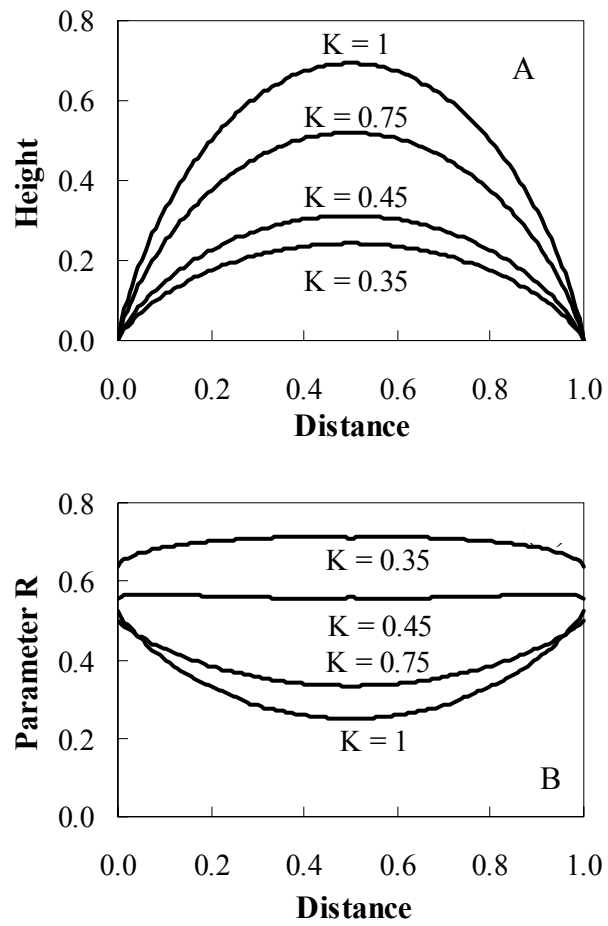


Figure 7-5. Theoretical steady state curve derived from the contact mechanics model A) theoretical steady state curves for different values of pre-function coefficient K B) the corresponding R curves.

## CHAPTER 8 MICROLENS ARRAY FABRICATION BY CHEMICAL MECHANICAL POLISHING

Chemical Mechanical polishing(CMP) was used to shape hexagonally arranged 20 $\mu\text{m}$  diameter cone shaped structures, prepared by wet etching of Corning 2496 glass, into microlenses. Edge rounding which occurs during CMP due to higher removal rate at the edges was utilized for shaping of microlenses. Microlenses with H/D ratio of  $\sim 1/10$  and radius of curvature of 27.5 $\mu\text{m}$  were obtained. CMP variables that affect the contact pressure and material removal rate are down pressure, linear velocity, slurry and properties of the pad. These variables being external to substrate provide great flexibility and hence suitability of the process for a wide range of materials.

### **Introduction**

Microlens array is used in detector and sensor arrays, optical fiber interconnects, switches, amplifiers, isolators, multiplexers, attenuators and imaging.<sup>106</sup> Microlenses are also an integral part of flat panel display systems and photocopiers.<sup>106</sup> Microlenses are fabricated in a wide range of sizes varying from 5  $\mu\text{m}$  to 1000  $\mu\text{m}$  with even submicron lenses reported in literature. It is finding new applications in light extraction and machine vision.<sup>106,107</sup> The development of microlens fabrication technique over the past three decades has been closely related to the development in semiconductor/IC fabrication technology. A summary of various fabrication methods can be found in ref. 106. Photoresist reflow method<sup>108</sup>, UV curable resins<sup>109</sup> and ink jet fabrication<sup>110</sup> method forms microlenses of polymeric materials and uses surface tension for shaping of the lenses. Inorganic microlenses are formed by engraving these polymeric lenses onto the inorganic substrate using reactive ion etching (RIE) where the etch rate of photoresist and

glass/substrate material is tailored to be same. Molding and hot embossing are used for fabricating larger microlenses of glass. A microlens fabrication process should be versatile in its applicability to different substrate materials, size and shape of created microlenses. Most of the current fabrication techniques have limitations in some of these areas, restricting its applicability.

In this communication, we report the possibility of using chemical mechanical polishing (CMP) as a technique for fabrication of microlens arrays. Chemical mechanical polishing is a standard technique used for planarization of wafers in the IC/semiconductor industry. In CMP, mechanical polishing assisted by chemical action is used for planarization of high elevation features. The material removal rate in a CMP process is proportional to the contact pressure and velocity as given by the Preston's equation<sup>101</sup>.

$$\frac{\partial f}{\partial t} = kPV$$

where  $f$  is the thickness of the film,  $P$  is the contact pressure,  $V$  is the linear velocity and  $k$  is the wear coefficient. The higher the contact pressure the higher is the material removal rate. Contact pressure depends not only on the applied down pressure but also on the shape and properties of the contacting surfaces i.e. it is a function of dimensions of surface features, the structure and surface condition of the polishing pad. Contact pressure will be uniform for a feature-less flat wafer whereas for a wafer with high and low elevation features it will vary along the wafer. Contact pressure at high elevation feature is typically greater than that at the low lying areas. Modeling and experimental work done on the dynamics of planarization of a step feature (Figure. 8-1) have shown the variation in material removal rate and contact pressure along various patterns with different step sizes and pattern density.<sup>102-104,111</sup> Figure 8-1 (A)-(B) shows the linear

profile of the step and its corresponding contact pressure distribution with progression of the CMP process.<sup>103,104</sup> The sharp edges in the initial feature results in high contact pressure at the edges leading to high removal rate. The resultant edge rounding reduces the contact pressure at the edges. As seen in Figure 8-1, the progressive rounding of the edge results in reduction of the pressure difference between the center and edge of the step. Further polishing leads to a rounded surface with uniform pressure distribution across the feature. Contact pressure being dynamic changes continuously during polishing with change in the topography of the surface. Chekina et al.<sup>103</sup> and Saxena et al.<sup>104</sup> in their modeling work predicted reduction in variations in contact pressure with the progression of CMP, until a steady state is reached after which surface topography does not change with further polishing. The shape tended towards equilibrium where material removal at every point is same. It was shown that the final steady state surface topography might or might not be a planarized surface depending on the properties of the contacting surfaces mainly the elastic modulus of the pad. It is known that CMP pads with higher elastic modulus (hard) result in better planarity whereas softer pads lead to more edge rounding. Though the phenomenon of edge rounding has been known for a long time, we have studied the possibility of using it as a means for shaping conical/cylindrical features into microlenses.

### **Experimental Procedure**

Hexagonal array of circular dots with 20  $\mu\text{m}$  diameter and 5  $\mu\text{m}$  spacing was patterned in a 1  $\text{cm}^2$  area on 1  $\text{inch}^2$  glass (Corning 2496) coupons. 2000  $\text{\AA}$  Cu was deposited on top of 50  $\text{\AA}$  Cr adhesion layer on these glass coupons to form a hard mask. Microposit S1813 photoresist and standard UV photolithography using a Karl Suss MA6

Aligner with a 365 nm Hg i-line radiation was used to develop the pattern. After removing Cu by wet etching and Cr by reactive ion etching, the patterns were etched in 5% HF solution to form 20  $\mu\text{m}$  diameter cone shaped structures of glass. Figure 8-2(A) shows the patterned substrate after wet etch process. The patterned samples were polished using Struers Tegra Force 5 at a down pressure of 2.5 psi. Polishing was done using softer Politex™ pads at 50 rpm with both the polishing head and pad rotating in the same direction and at same rpm. Politex™ pad is among the softest CMP pads used for final polishing of wafers compared to Suba™ and IC™ series harder pad which are used to achieve better planarity in wafers. 5 wt% SiO<sub>2</sub> slurry made from dilution of Levasil 50cK (nominal particle size ~80 nm) at pH 4.0 and a flow rate of 50 mL/min was used during polishing. The surface was characterized using a Veeco Dimension 3100 Atomic force microscope (AFM) using contact mode.

### **Results and Discussion**

Figure 8-2 shows the atomic force microscope image of (B) an individual microlens and (C) microlens array formed after 1 min of chemical mechanical polishing. Figure 8-3 shows a line profile along the center of the lens taken from AFM before and after polishing. The rounding of the surface upon polishing can be observed from the curves. Around 1  $\mu\text{m}$  in height was polished in 1 min at 2.5 psi. It can be argued that the polishing rate will initially be high for conical features and would drop subsequently as the contact area increases due to rounding of the structures. Figure 8-4 shows the line profile of a feature after chemical mechanical polishing and its theoretical fit to a circular profile. The coefficient of determination (R-squared) between the line profile and circular fit was calculated using the formula

$$R^2 \equiv 1 - \frac{\sum_i (y_i - \bar{y})^2}{\sum_i (y_i - f_i)^2}$$

where  $y_i$  is the line profile data,  $\bar{y}$  is the mean and  $f_i$  is the theoretical circular profile.

The best fit circular profile was obtained by iteratively changing the radius and center of the theoretical circular profile to maximize the value of the fitting parameter (R-squared).

The radius of curvature of the best fit circular profile was 27.5  $\mu\text{m}$  with R-squared value of 0.995, indicating a good fit with the AFM profile. Figure 8-5 shows the line profile

across the centre of feature from the deflection image of AFM before and after polishing.

It is known that deflection image is the derivative of height variations at higher integral

and proportional gains. The deflection scan of the conical feature is linear except in three

small regions where slope change occurs. In comparison to this the deflection scan of a

microlens shows a continuous change in slope along the profile as should be the case for

derivative of a circular profile near the top of the sphere. The curve fitting along with the

deflection scan shows that the curvature obtained after chemical mechanical polishing

under the conditions was close to a spherical profile needed for a microlens. Also, the

variation in the height to diameter (H/D) ratio of the microlens both within an array and

from coupon to coupon was found to be within 1.5% under similar CMP conditions

showing a good control and repeatability of the process.

Surface roughness is an important concern for optical surfaces. The fabrication being based on a planarization process can be expected to produce a very low roughness surface. In the current process shaping of microlens is mostly dependent on the mechanical aspects of CMP; where as the surface roughness will be dependent on the

slurry content namely abrasive particles and chemistry which can be readily tuned to a particular substrate material. Figure 8-6 shows the scanning electron microscope image of the microlens array formed after chemical mechanical polishing.

### **Conclusions**

This work demonstrated the feasibility of using chemical mechanical polishing for formation of microlenses by gradual shaping of features. It is fully compatible with the current semiconductor/IC fabrication processes. The formation of microlenses by CMP is due to high contact pressure developed at edges hence it is equally applicable to other inorganic optical materials. The variables in a CMP process that affect the material removal/polishing rate are the down pressure, linear velocity, the slurry and the properties of the pad. These variables being external to substrate provide great flexibility and hence suitability of the process for a wide range of materials.

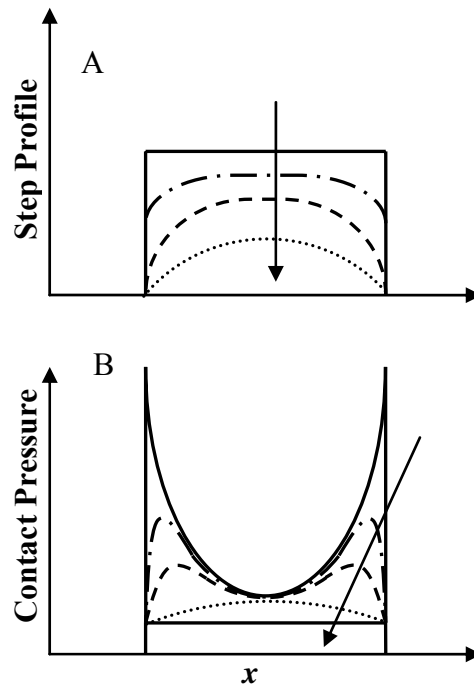


Figure 8-1. Evolution of a step feature and contact pressure along a step profile with progression of CMP A) step feature and the corresponding B) contact pressure. The arrow indicates the changes in curves with polishing.

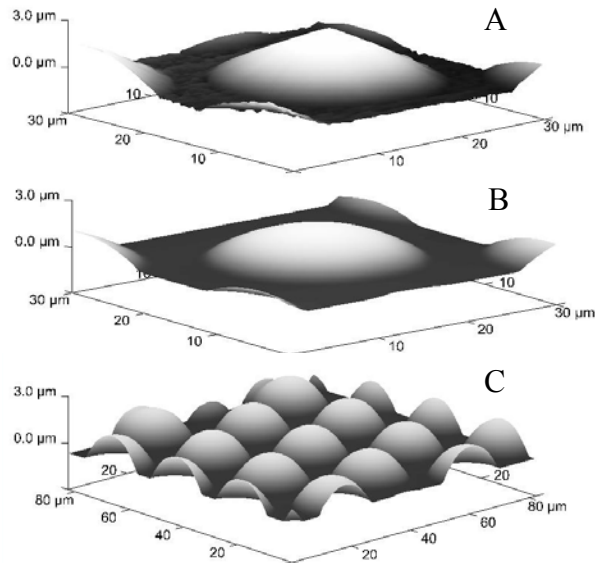


Figure 8-2. AFM image of features before and after CMP A) conical feature after wet etching B) individual microlens and C) microlens array after CMP.

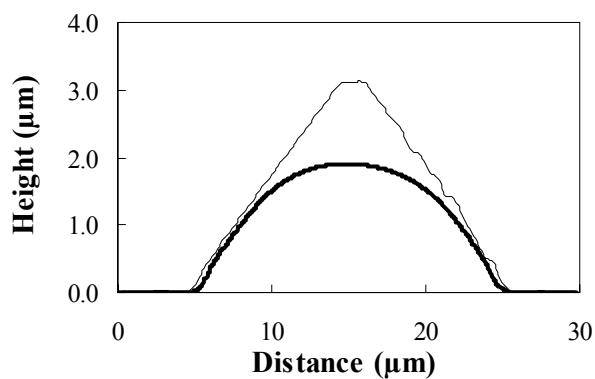


Figure 8-3. AFM line profile along the center of feature before and after CMP.

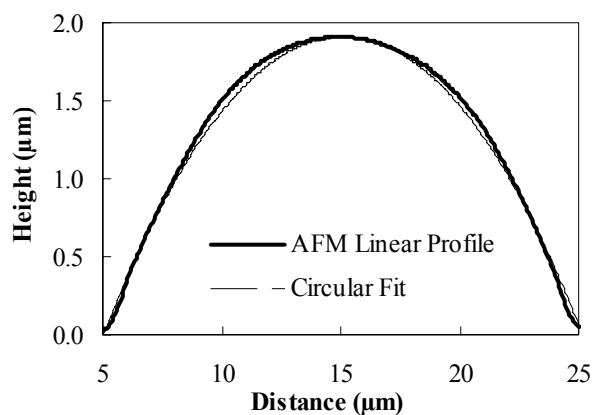


Figure 8-4. AFM line profile and theoretical circular fit of CMP fabricated microlens.

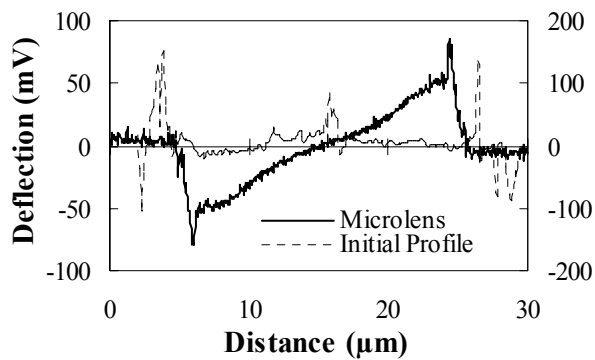


Figure 8-5. AFM line profile obtained from deflection image of initial feature and feature after CMP.

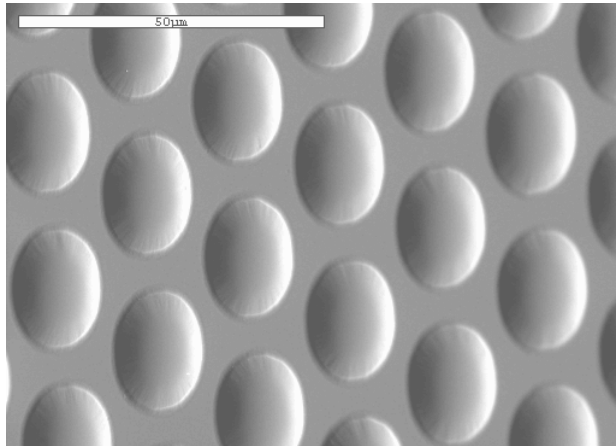


Figure 8-6. SEM image of microlens array formed after CMP.

## CHAPTER 9 ENHANCED LIGHT OUT-COUPLING FROM CONICAL, PYRAMIDAL AND MICROLENS ARRAY

### **Introduction**

Recently there has been a lot of interest in solid state lighting because of its potential to drastically reduce the energy consumption for general lighting purposes. The application of light emitting diodes (LEDs) and Organic-LEDs for generation of white light generally involves two approaches: a combination of red, blue and green emission devices or a UV or blue device in conjunction with a phosphor material for conversion to white light. These devices could potentially have very high efficiencies arising from the very high internal quantum efficiency i.e. the efficiency of conversion of electron-hole pairs to photons. The internal quantum efficiency which depends mostly on the material quality is close to 90% in many of these devices. The main hurdle to a high light output is the total internal reflection of photons within the device and the subsequent wave-guiding and absorption. The high refractive index of the active layer results in a small critical angle for internal reflection at the interfaces and defines a small escape cone. Photons outside the escape cone are repeatedly reflected in the device and are finally lost to absorption. This is among the major challenges in the realization of solid state lighting.

Many techniques have been researched to increase the light output from solid state lighting devices. Among these are opening of higher number of the six escapes cones for each direction (lateral and vertical) by use of thick transparent substrates, shaping of LED chips or by reducing wave-guiding through modification of various interfaces in the device.<sup>17-52</sup> Wave-guiding occurs mainly because of the planar structure of the device which preserves the incident angle upon internal reflection. Interface modification changes the incident angle for subsequent incidences, thereby giving multiple chances to photons to escape. Photon randomization has been achieved by simple interface roughening<sup>5</sup> or by having regular patterned structures at various

interfaces e.g. bragg gratings,<sup>9</sup> micro-rings,<sup>10</sup> photonic crystals,<sup>11</sup> microlenses,<sup>12</sup> micro-pyramids,<sup>13</sup> etc. We saw in the previous chapters that regular patterned structures with inclined walls like cones, pyramids and microlens array at the interface leads to a methodic change in directionality of photons after every internal reflection from the interface, thereby increasing its chances of out-coupling. These structures not only increase light out-coupling but also improves the uniformity in angular distribution of out-coupled photons. Most previous work on microlens array has been done on Organic-LEDs with polymeric microlens array on glass substrates. Polymeric microlenses are effective in out-coupling light from the substrate mode in OLEDs because of similar refractive index of glass substrates and polymeric lenses. Polymeric microlens array is of limited use in LED with much higher substrate refractive index. Few attempts have been made to form microlens array of both sapphire and GaN, using resist reflow and plasma etching, though with limited dimensions and aspect ratios. Other structures like conical and pyramidal have been less commonly researched, apart from some simulation work of Greiner,<sup>13</sup> Chang et al.<sup>94</sup> and Lee et al.<sup>96</sup> which studied conical and pyramidal structures on different types of devices. There is a need of a comparative study of these structures to ensure maximum light out-coupling from devices. In this work we have done both simulation and experimental studies of light out-coupling using microlens, conical and pyramidal arrays.

### **Simulations**

Figure 6-1 shows the schematic of the device simulated in our study. It consists of a high refractive index active layer (thickness,  $t \sim 2 \mu\text{m}$ , refractive index,  $n \sim 1.9$ ) on a substrate ( $t = 1 \text{ mm}$ ,  $n = 1.5, 1.7, 1.9$ ). The device size was  $2 \text{ mm} \times 2 \text{ mm}$  with reflecting sides. The top surface of the substrate was textured with conical, pyramidal or microlens arrays of diameter/base  $20 \mu\text{m}$  with different aspect ratios. The area coverage was kept constant at 58% for all structures. The bottom

surface of the active layer was assumed to have a reflective contact with different absorptions. In LEDs, OLEDs and thin film phosphor devices, there is a substrate with an active layer grown on it. Typically the substrate/active layer interface is smooth due to the requirements of thin film growth. A reflector, either a metallic mirror or a Bragg reflector is put at the bottom of the device. In most cases, the emission from active layer is believed to be isotropic. The device in simulation represents a simplified LED, OLED structure. Monte Carlo ray tracing simulations were done for a million rays generated with random directionality in the active layer. All simulations were done for light of 593 nm wave length. Absorption at the interface was realized by proportionally reducing the power of all rays incident on the surface. Aspect ratio of the structures (cone/pyramid/microlens) was varied by varying the contact angle between 0 to 90° as shown in Figure 6-1.

Figure 9-1 shows the light out-coupling from the devices when different structures were used. Devices with conical and pyramidal arrays shows similar out-coupling for same contact angle and area coverage of the array. These structures show maximum out-coupling around ~45-50° with minor variations on the refractive index of the substrates. Conical and pyramidal structures cause bending of rays, similar to that observed in prisms and known as angle of deviation. Out-coupled rays experience bending towards the device when encountered with these structures along the way. These rays would reenter the device and have to be out-coupled again, experiencing further absorption. The reentry is higher for high aspect ratio structures and hence the small decrease in efficiency for high contact angle structures. This decrease it seems is higher for high refractive index substrates, which is because of higher bending power of the structures. The out-coupling from microlens array increases with contact angle showing maximum for

hemispherical lenses. It should be noted that for similar contact angles, till 45 - 50°, conical and pyramidal array shows better out-coupling where as beyond it, microlens shows better efficiency.

Figure 9-2 shows the variation of out-coupling from conical array on different refractive index substrates as a function of back absorption in the device. The out-coupling increases with decrease in back absorption, more so for high refractive index substrates. Figure 9-3 shows the normalized far-field angular intensity distribution from conical and microlens array of 15° contact angle and substrate refractive index of 1.5 for different back absorptions. Pyramidal array which shows total out-coupling similar to conical array, show a four-fold symmetry in angular intensity corresponding to each pyramidal face as pointed by Greiner<sup>13</sup> in contrast to circular symmetry from conical array. The use of conical and microlens array leads to increase in intensity at higher angles, the magnitude of which is dependent on the absorption at the back surface. Comparison of the angular intensity of absorptive and reflective back surface indicates to internally reflected rays being extracted at higher angles after subsequent reflections. Based on the simulation studies we can say, pyramidal and conical arrays are similar from the point of light extraction where as microlens arrays enjoys an advantage when the lens shape is hemispherical.

## **Experimental Procedure**

### **Sample Preparation**

Conical and microlens array was prepared by a combination of lithographic, wet etching and chemical mechanical polishing (CMP) techniques. Hexagonal array of circular dots with 20 μm diameter and 5 μm spacing was patterned in a 1 cm<sup>2</sup> area on 1 inch<sup>2</sup> glass (Corning 2496) coupons. 2000 Å Cu was deposited on top of 50 Å Cr adhesion layer on these glass coupons to form a hard mask. Microposit S1813 photoresist and standard UV photolithography using a Karl

Suss MA6 Aligner with a 365 nm Hg i-line radiation was used to develop the pattern. After removing Cu by wet etching and Cr by reactive ion etching, the patterns were etched in 5% HF solution to form 20  $\mu\text{m}$  diameter cone shaped structures of glass. Figure 8-2(A) shows the patterned substrate after wet etch process. Microlens array was formed by chemical mechanical polishing of conical array using soft politex pad and at low pressure. The patterned samples were polished using Struers Tegra Force 5 at a down pressure of 2.5 psi with both the polishing head and pad rotating in the same direction at 50 rpm. 5 wt%  $\text{SiO}_2$  slurry made from dilution of Levasil 50cK (nominal particle size  $\sim 80$  nm) at pH 4.0 and a flow rate of 50 mL/min was used during polishing. Microlens array formation using chemical mechanical polishing and its characterization has been described in chapter 8. Figure 8-2 (B-C) shows the microlens array formed on the glass substrate.

### **Out-Coupling Measurements**

After formation of conical and microlens array on glass coupons using lithography and etching, the substrates were backed with an aluminum disk with a 2 mm diameter hole in the center. A 2 mm diameter LED (SunLED XSUG62D) was inserted through the center opening for light generation. The LED and aluminum disk were attached to the glass coupons using an index matching adhesive (Norland Optical adhesive 65). Two types of measurement were taken, one with a completely absorbing back ensured by having a thick graphite coating on the back of the glass substrate and second with a reflective back surface accomplished by sputter coating Al on the back surface of glass. In both cases, a 2 mm diameter area at the center was kept clear for LED attachment. Total out-coupling from the substrate was measured using an integrating sphere by driving the attached LED at different constant current values. Out-coupling intensity was measured from an orthogonal port using an optical fiber and Ocean optics USB 2000

spectrometer. Integrating sphere minimizes the effects of the original directionality of incident beam but preserves the effect of power; it can thus be used to measure total out-coupling efficiency. Angular intensity was measured by mounting the textured substrate on a rotatable jig with fiber optic aligned with the center of the substrate at a distance of 3 inch. The substrate was illuminated by a backing LED (SunLED XSUG62D) driven by constant current of 10 mA. Figure 4-3 and Figure 4-4 shows the experimental setup to measure the total out-coupling efficiency and angular intensity distribution of the substrates.

### **Results and Discussion**

Figure 9-4 shows the total out-coupling measured for all the substrates planar, conical and microlens array with increase in LED drive current where as figure 9.5 summarizes these enhancement observed for various substrates. The out-coupling for all substrates increased linearly with LED drive current. The angular distribution of photons within the planar glass substrate would be similar to that in the epoxy encapsulant, since the refractive index of LED encapsulant epoxy ( $n=1.47$ ), the index matching gel ( $n=1.52$ ) and the glass substrate ( $n=1.51$ ) was similar. The slight higher index of glass substrate would ensure the in-coupling of all rays from the epoxy into the glass substrate. The 2 mm LED port would be source of some error in measurement of out coupling in microlens and conical arrays which would reflect back some rays through the port. In planar substrates, all rays would be either out-coupled or reflected outside the LED port. Since the structures studied have lower contact angle of  $15^\circ$ , there will be minimal reentry of rays into the epoxy and hence would not lead to much error in measurements. The conical array showed higher efficiency than microlens array as predicted by the simulation studies for substrates with reflective backing. Ideally, planar substrate with both Al coating and graphite coating should show similar out-coupling since in planar substrates rays get only one

chance to out-couple, once reflected it is wave-guided and finally absorbed. The higher efficiency for Al coated planar substrate during measurements is probably because of the rough edges at the substrate end and to some extent diffuse scattering from the back surface. The out-coupling efficiency of Al coated planar substrate is  $\sim 5\%$  higher than graphite coated planar substrate. The conical and microlens array substrates with graphite absorber at the back showed slightly less out-coupling compared to the planar substrate with an absorbing back. The simulation work too did not predict any increase in efficiency when the back surface was 100% absorbing. Multiple reflection and reduction in wave-guiding is the primary source of enhancement obtained from textured surface. Upon use of an Al back reflector, conical array showed as much as 23% enhancement where as microlens array showed an improvement of 18% over planar substrates with graphite backing.

Figure 9.6 shows the angular distribution of intensity from absorbing planar substrate and conical and microlens array substrates at a LED drive current of 10 mA. It also shows angular distribution from an LED without a substrate. The curves were normalized to the maximum intensity of bare LED in forward direction and to the total out-coupling. It should be noted that the output from bare LED is not lambertian; it seems to decrease linearly with angle. The lowest intensity in forward direction was observed for planar substrate. The intensity in forward direction is enhanced in the case of textured substrates due to multiple reflections. Conical array was observed to show higher intensity than microlens array for most angles. Figure 9-7 shows the normalized angular intensity from conical and microlens array with both reflective (sputtered Al) and absorptive (graphite) back surface. The conical substrate with reflective back shows a progressive increase in intensity with increase in angle relative to the absorptive substrate. On the other hand, microlens substrate with reflective back shows a similar enhancement for a broad

angular range. Figure 9-8 shows the variation of angular enhancement, defined as the ratio of angular intensity from reflective and absorptive substrate, for conical and microlens array. The figure also shows the angular enhancement obtained from ray tracing simulations for structures with  $15^\circ$  contact angle and 40% back absorption. It should be noted that simulations were done for devices with a lambertian intensity profile in the substrate. Though the intensity in the substrate from light emission from LED is not lambertian, the experimental enhancement matches the simulation results. The angular enhancement increases with angle indicating higher extraction at higher angles compared to forward directions.

### **Conclusions**

Surface texturing using conical array is an efficient way of light extraction compared to microlens array for structures with contact angle less than  $50^\circ$ . Though pyramidal array show out-coupling similar to conical array, conical arrays show better angular distribution. Conical array with contact angle of  $17^\circ$  showed an enhancement of 23% compared to 18% from microlens array. Very high absorption in textured substrates was found to be completely ineffective in increasing light out-coupling. Angular intensity measurements showed that the increase in enhancement came from extraction of rays at higher angles.

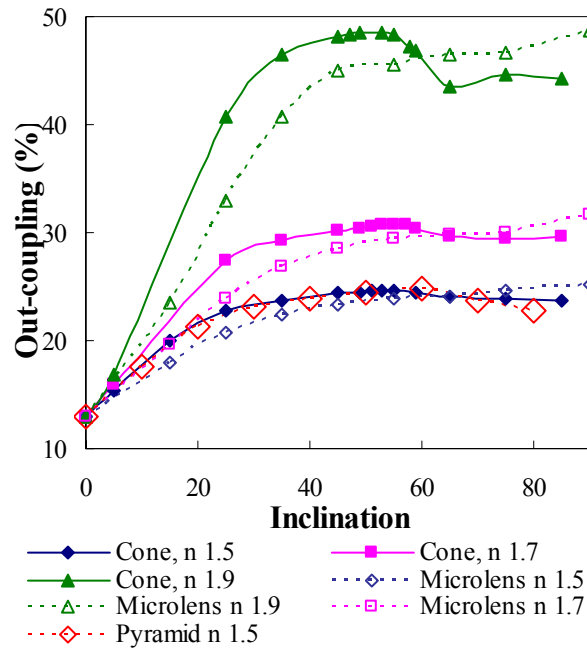


Figure 9-1. Simulated out-coupling from conical, pyramidal and microlens array with increase in contact angle and substrate refractive indices. The base diameter/width of structure was 20  $\mu\text{m}$  with 58% area coverage and 80% back absorption.

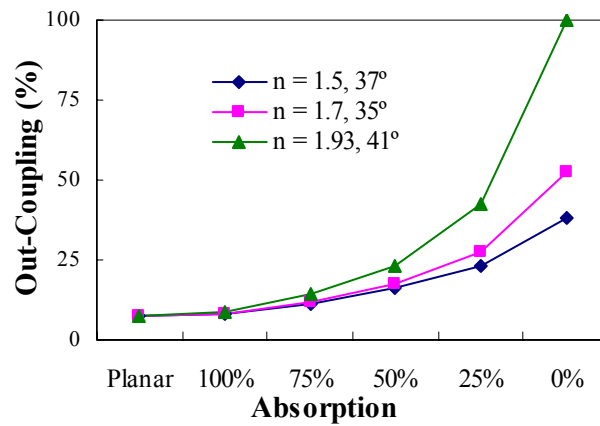


Figure 9-2. Variation in out-coupling with back absorption from conical array.

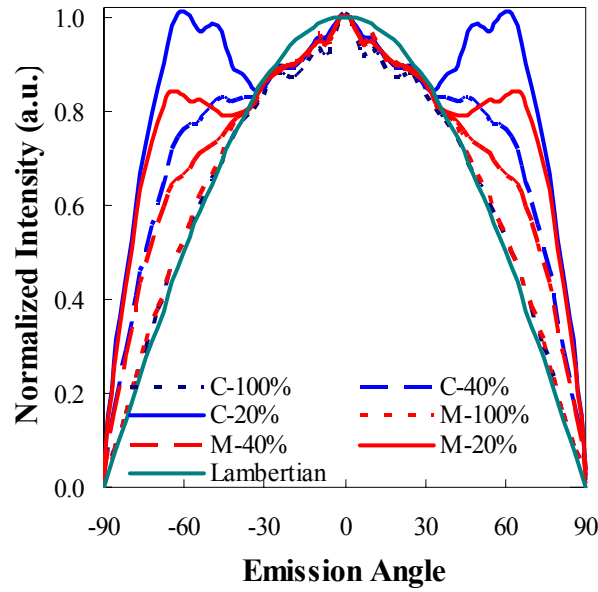


Figure 9-3. Angular intensity distribution from conical and microlens array of contact angle 15° and back absorption of 20%, 40% and 100%. The figure also shows a lambertian intensity profile.

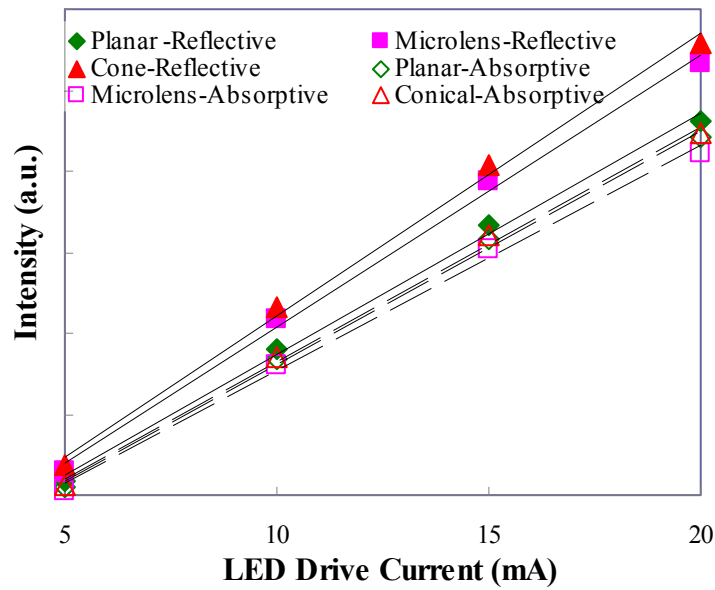


Figure 9-4. Measured out-coupling from planar, conical and microlens array with increase in LED drive current. The substrates were made reflective by sputtered Al coating and absorptive by a thick graphite coating at the back.

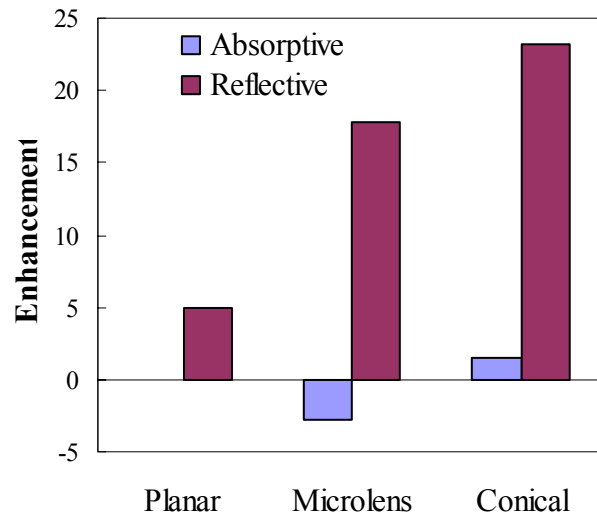


Figure 9-5. Summary of measured out-coupling enhancement from different substrates.

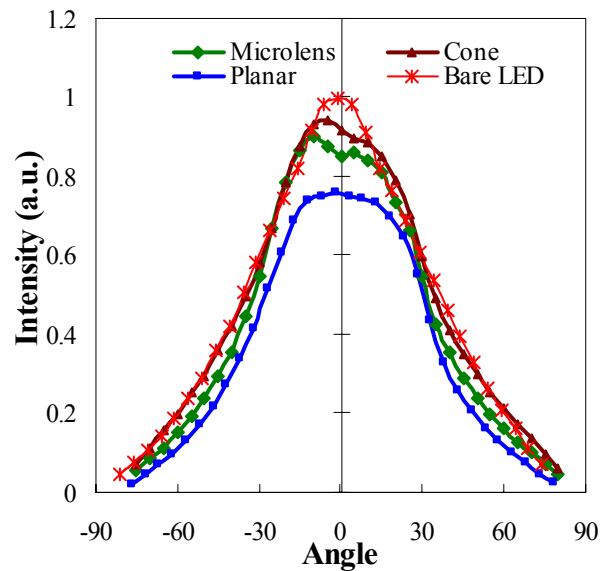


Figure 9-6. Measured angular intensity distribution from different reflective substrates normalized to maximum intensity from a bare LED. Reflective substrates show enhancement in both forward direction and at higher angles.

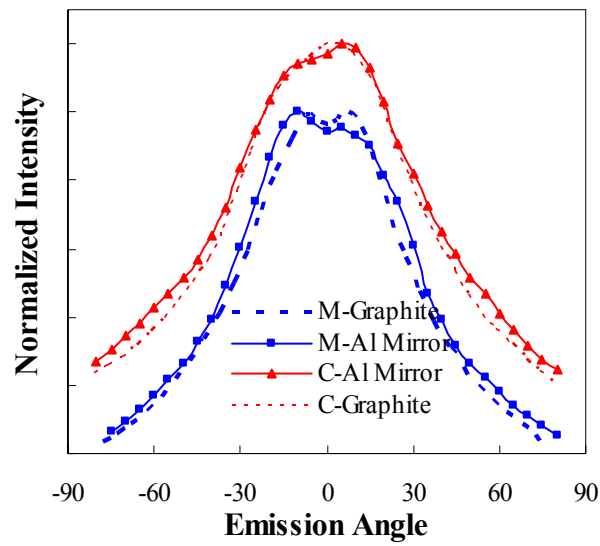


Figure 9-7. Comparison of measured angular intensity distribution of reflective and absorbing substrates.

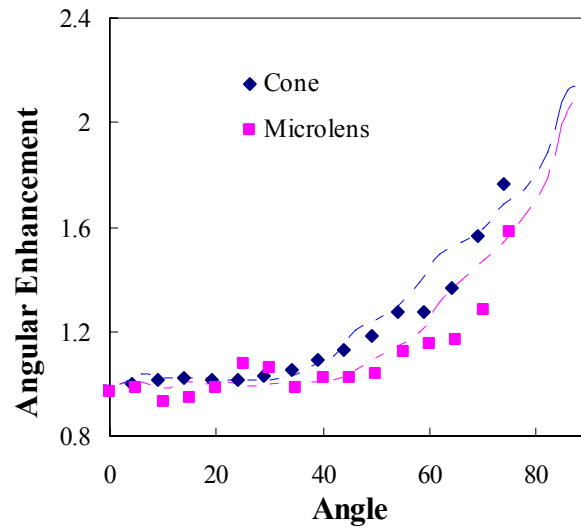


Figure 9-8. Ratio of angular intensity of reflective and absorbing substrates along with the simulation curve for a device with structures of contact angle  $15^\circ$  and 40% back absorption.

## CHAPTER 10 CONCLUSIONS

The two-dimensional geometrical analysis and both 2D and 3D simulations show that there is a regular ray dynamics and not just photon randomization behind the increased out-coupling from periodic inclined structures. The ray dynamics of inclined wall structures enhances the probability of escape after every reflection, making it a better alternative to surface roughening which completely relies on photon randomization. Surface inclination of  $45^\circ$  leads to wave guiding and should be avoided for one-dimensional structures, whereas for two-dimensional conical or pyramidal structures maximum out-coupling would be achieved with an inclination  $\sim 50^\circ$ . Absorptions in the device, in the active layer, substrate or at the contacts limit the out-coupling efficiency. Had it not been for absorption, all the rays will be out-coupled after multiple reflections. The surface structure which reduces the total number of back reflections will give the highest out-coupling efficiency.

Light out-coupling from LEDs and OLEDs using microlens arrays as external out-coupler was analyzed. Microlens arrays enhance efficiency both by extracting rays lying outside the escape cone and also by redirecting a portion within the escape cone at subsequent reflection. The number of back reflection required for out-coupling reduces with increase in the aspect ratio of microlenses. The reduced reflection leads to less absorption of rays and hence increased efficiency for hemispherical microlenses. Microlens arrays give better uniformity in angular distribution of intensity. High index substrates have huge potential to enhance out-coupling but can only be realized in low absorption devices.

Chemical mechanical polishing is a standard IC fabrication technique used in both front-end and back-end of line for planarization of wafers. Up till now research was focused on reducing the non-planarizing aspects of CMP such as edge rounding, dishing etc. We studied the

non-planarizing phenomena of edge rounding for creation of surfaces with different curvatures. A softer pad with low elastic modulus at low pressures is most suited for shaping of surfaces. The dynamics of the polishing process followed the contact mechanics based CMP model. The various CMP variables (pad, pressure) affect the profiles as predicted by the contact mechanical model. Various curvatures including spherical were created by CMP at different stages of polishing.

Chemical Mechanical polishing was used to shape hexagonally arranged 20 $\mu$ m diameter cone shaped structures, prepared by wet etching of Corning 2496 glass, into microlenses. Edge rounding which occurs during CMP due to higher removal rate at the edges was utilized for shaping of microlenses. Microlenses with H/D ratio of  $\sim 1/10$  and radius of curvature of 27.5 $\mu$ m were obtained. The work demonstrated the feasibility of using chemical mechanical polishing for formation of microlenses by gradual shaping of features. It is fully compatible with the current semiconductor/IC fabrication processes. The variables in a CMP process that affect the material removal/polishing rate are the down pressure, linear velocity, the slurry and the properties of the pad. These variables being external to substrate provide great flexibility and hence suitability of the process for a wide range of materials.

Surface texturing using conical arrays is an efficient way of light extraction compared to microlens arrays for similar contact angle structures below contact angle of  $\sim 50^\circ$ . Though pyramidal arrays show out-coupling similar to conical arrays, conical arrays show better spatial distribution. Conical arrays with contact angle of  $17^\circ$  showed an enhancement of 23% in comparison to 18% from microlens arrays. Very high absorption in textured substrates was found to be completely ineffective in increasing light out-coupling. Angular intensity measurement showed the increase in enhancement to come from extraction of rays at higher angles.

## LIST OF REFERENCES

1. “Energy Savings Potential of Solid State Lighting in General Illumination Applications”, Building Technologies Program, Office of Energy Efficiency and Renewable Energy, U.S. Department of Energy, November 2003.
2. E. F Schubert, Y. H. Wang, A. Y. Cho, L. W. Tu and G. J. Zydzik, *Appl. Phys. Lett.*, **60**, 921 (1992).
3. A. Köck, W. Beinstingl, K. Berthold and E. Gornik, *Appl. Phys. Lett.*, **52**, 1164 (1988).
4. T. Baba, R. Watanabe, K. Asano, F. Koyama and K. Iga, *Jpn. J. Appl. Phys.*, **35**, 97 (1996).
5. A. A. Bergh, and R. H. Saul, “Surface roughening of electroluminescent diodes”, U.S. Patent No. 3,739,217 (1973).
6. H. W. Deckman, and J. H. Dunsmuir, *Appl. Phys. Lett.*, **41**, 377 (1982).
7. J. Choi, PhD Dissertation, University of Florida (2003).
8. K. G. Cho, D. Kumar, S. L. Jones, D. G. Lee, P. H. Holloway and R. K. Singh, *J. Electrochem. Soc.*, **145**, 3456 (1998).
9. J. M. Lupton, B. J. Matterson, I. D. W. Samuel, M. J. Jory, and W. L. Barnes, *Appl. Phys. Lett.*, **77**, 3340 (2000).
10. H. W. Choi, M. D. Dawson, P. R. Edwards, and R. W. Martin, *Appl. Phys. Lett.*, **83**, 4483 (2003).
11. T. Krauss, Y. P. Song, S. Thoms, C. D. W. Wilkinson, and R. M. De La Rue, *Electron. Lett.*, **30**, 1444 (1994).
12. C. F. Madigan, M. H. Lu, and J. C. Sturm, *Appl. Phys. Lett.*, **76**, 1650 (2000).
13. H. Greiner, *Jpn. J. Appl. Phys.*, **46**, 4125 (2007).
14. K. Bao, X. N. Kang, B. Zhang, T. Dai, C. Xiong, H. Ji, G. Y. Zhang and Y. Chen, *IEEE Photon. Technol. Lett.*, **19**, 1840 (2007).
15. N. Holonyak Jr. and S. F. Bevacqua, *Appl. Phys. Lett.*, **1**, 82 (1962).
16. W. N. Carr and G. E. Pittman, *Appl. Phys. Lett.*, **3**, 173 (1963).
17. W. N. Carr, *Infrared Phys.*, **6**, 1 (1965).
18. K. Kurata, Y. Ono, M. Morioka, K. Ito, and M. Mori, *IEEE J. Quantum Electron.*, **13**, 525 (1977).

19. W. N. Carr, *Infrared Phys.*, **6**, 1 (1966).
20. S. J. Lee, and S. W. Song, *Proc. SPIE*, **249**, 3621 (1999).
21. C. H. Chiu, H.C. Kuo, C. F. Lai, H. W. Huang, W. C. Wang, T. C. Lu, S. C. Wang, and C. H. Lin, *J. Electrochem. Soc.*, **154**, H944 (2007).
22. J. Y. Kim, M. K. Kwon, J. P. Kim, and S. J. Park, *IEEE Photon. Technol. Lett.*, **19**, 1865 (2007).
23. H. Masui, S. Nakamura, and S. P. DenBaars, *Applied Optics*, **47**, 88 (2008).
24. C. E. Lee, H. C. Kuo, Y. C. Lee, M. R. Tsai, T. C. Lu, S. C. Wang and C. T. Kuo, *IEEE Photon. Technol. Lett.*, **20**, 184 (2008).
25. A. A. Bergh, and R. H. Saul, "Surface roughening of electroluminescent diodes", U.S. Patent No. 3,739,217 (1973).
26. I. Schnitzer, E. Yablonovitch, C. Caneau, T. J. Gmitter, and A. Scherer, *Appl. Phys. Lett.*, **63**, 2174 (1993).
27. M. Boroditsky, and E. Yablonovitch, *Proc. SPIE*, **119**, 3002 (1997).
28. H. W. Deckman and J. H. Dunsmuir, *Appl. Phys. Lett.*, **41**, 377 (1982).
29. S. J. Lee, *Jpn. J. Appl. Phys.*, **37**, 509 (1998).
30. R. Windisch, P. Heremans, P. Kiesel, G. H. Döhler, B. Dutta, and G. Borghs, *Appl. Phys. Lett.*, **74**, 2256 (1999).
31. R. Windisch, P. Heremans, B. Dutta, M. Kuijk, S. Schoberth, P. Kiesel, G. H. Döhler, and G. Borghs, *Electronic Lett.*, **34**, 1153 (1998).
32. R. Windisch, C. Rooman, M. Kuijk, B. Dutta, G. H. Döhler, G. Borghs, and P. Heremans, *Electronic Lett.*, **36**, 351 (2000).
33. R. Windisch, B. Dutta, M. Kuijk, A. Knobloch, S. Meinschmidt, S. Schoberth, P. Kiesel, G. Borghs, G. H. Döhler, and P. Heremans, *IEEE Trans. Electron Devices*, **47**, 1492 (2000).
34. R. Windisch, C. Rooman, S. Meinschmidt, P. Kiesel, D. Zipperer, G. H. Döhler, B. Dutta, M. Kuijk, G. Borghs, and P. Heremans, *Appl. Phys. Lett.*, **79**, 2315 (2001).
35. C. Huh, K. S. Lee, E. J. Kang, and S. J. Park, *J. Appl. Phys.*, **93**, 9383 (2003).
36. T. Fujii, Y. Gao, R. Sharma, E. L. Hu, S. P. DenBaars, and S. Nakamura, *Appl. Phys. Lett.*, **84**, 885 (2004).

37. H. Kasugai, Y. Miyake, A. Honshio, S. Mishima, T. Kawashima, K. Iida, M. Iwaya, S. Kamiyama, H. Amano, I. Akasaki, H. Kinoshita, and H. Shiomi, *Jpn. J. Appl. Phys.*, **44**, 7414 (2005).
38. K. Kim, J. Choi, T. S. Bae, M. Jung, and D. H. Woo, *Jpn. J. Appl. Phys.*, **46**, 6682 (2007)
39. H. Kim, J. Cho, J. W. Lee, S. Yoon, H. Kim, C. Son, Y. Park, and T. Y. Seong, *Appl. Phys. Lett.*, **90**, 161110 (2007).
40. J. M. Hwang, W. H. Hung, and H. L. Hwang, *IEEE Photon. Technol. Lett.*, **20**, 608 (2008).
41. H. Fang, X. N. Kang, C.Y. Hu, T. Dai, Z. Z. Chen, Z. X. Qin, B. Zhang, and G. Y. Zhang, *J. Crystal Growth*, **298**, 703 (2007).
42. M. K. Lee, C. L. Ho, and P. C. Chen, *IEEE Photon. Technol. Lett.*, **20**, 252 (2008).
43. T. S. Kim, S. M. Kim, Y. H. Hee, and G. Y. Jung, *Appl. Phys. Lett.*, **91**, 171114 (2007).
44. K. Bao, X. N. Kang, B. Zang, T. Dai, Y. J. Sun, Q. Fu, G. J. Lian, G. C. Xiong, G. Y. Zhang, and Y. Chen, *Appl. Phys. Lett.*, **92**, 141104 (2008).
45. Y. H. Cheng, J. L. Wu, C. H. Cheng, K. C. Syao, and M. C. M. Lee, *Appl. Phys. Lett.*, **90**, 091102 (2007)
46. R. Bathelt, D. Buchhauser, C. Gärditz, R. Paetzold and P. Wellmann, *Organic Electronics*, **8**, 293 (2007).
47. F. Li, X. Li, J. Zhang, and B. Yang, *Organic Electronics*, **8**, 635 (2007).
48. K. P. Kim, K. S. Lee, T. W. Kim, D. H. Woo, J. H. Kim, J. H. Seo, and Y. K. Kim, *Thin Solid Films*, **516**, 3633 (2008).
49. C. E. Lee, Y. C. Lee, H. C. Kuo, T. C. Lu, and S. C. Wang, *IEEE Photon. Technol. Lett.*, **20**, 659 (2008).
50. S. Fan, P. R. Villeneuve, J. D. Joannopoulos and E. F. Schubert, *Phys. Rev. Lett.*, **78**, 3294 (1997).
51. M. Boroditsky, T. F. Krauss, R. Coccioli, R. Vrijen, R. Bhat, and E. Yablonovitch, *Appl. Phys. Lett.*, **75**, 1036 (1999).
52. T. Baba, K. Inoshita, H. Tanaka, J. Yonekura, M. Ariga, A. Matsutani, T. Miyamoto, F. Koyama, and K. Iga, *J. Light Tech.*, **17**, 2113 (1999).
53. J. J. Wierer, M. R. Krames, J. E. Epler, N. F. Gardner, M. G. Craford, J. R. Wendt, J. A. Simmons, and M. M. Sigalas, *Appl. Phys. Lett.*, **84**, 3885 (2004).
54. H. Y. Ryu, Y. H. Lee, R. L. Sellin, and D. Bimberg, *Appl. Phys. Lett.*, **79**, 3573 (2001).

55. D. S. Han, J. Y. Kim, S. I. Na, S. H. Kim, K. D. Lee, B. Kim, and S. J. Park, *IEEE Photon. Technol. Lett.*, **18**, 1406 (2006).
56. A. A. Erchak, D. J. Ripin, S. Fan, P. Rakich, J. D. Jonnopoulos, E. P. Ippen, G. S. Petrich and L. A. Kolodziejski, *Appl. Phys. Lett.*, **78**, 563 (2001).
57. T. N. Order, J. Shakya, J. Y. Lin, and H. X. Jiang, *Appl. Phys. Lett.*, **83**, 1231 (2003).
58. T. N. Order, K. H. Kim, J. Y. Lin, and H. X. Jiang, *Appl. Phys. Lett.*, **84**, 466 (2004).
59. C. H. Chao, S. L. Chuang, and T. L. Wu, *Appl. Phys. Lett.*, **89**, 091116 (2006).
60. C. F. Lai, H. C. Kuo, C. H. Chao, H. T. Hsueh, J. F. T. Wang, W. Y. Yeh, and J. Y. Chi, *Appl. Phys. Lett.*, **91**, 123117 (2007).
61. J. Y. Kim, M. K. Kwon, K. S. Lee, S. J. Park, S. H. Kim, and K. D. Lee, *Appl. Phys. Lett.*, **91**, 181109 (2007).
62. A.M. Adawi, R. Kulloock, J.L. Turner, C. Vasilev, D.G. Lidzey, A. Tahraoui, P.W. Fry, D. Gibson, E. Smith, C. Foden, M. Roberts, F. Qureshi, and N. Athanassopoulou, *Organic Electronics*, **7**, 222 (2006).
63. Y. J. Lee, S. H. Kim, J. Huh, G. H. Kim, Y. H Lee, S. H. Cho, Y. C. Kim, and Y. R. Do, *Appl. Phys. Lett.*, **82**, 3779 (2003).
64. Y. R. Do, Y. C. Kim, Y. W. Song, and Y. H. Lee, *J. Appl. Phys.*, **96**, 7629 (2004).
65. Y. R. Do, D. H. Park, Y. C. Kim, and Y. D. Huh, *J. Electrochem. Soc.*, **150**, H260 (2003).
66. Y. R. Do, Y. C. Kim, S. H. Cho, J. H. Ahn, and J. G. Lee, *Appl. Phys. Lett.*, **82**, 4172 (2003).
67. Y. R. Do, Y. C. Kim, S. H. Cho, D. S. Zang, Y. D. Huh, and S. J. Yun, *Appl. Phys. Lett.*, **84**, 1377 (2004).
68. K. S. Sohn, N. Shin, Y. C. Kim, and Y. R. Do, *Appl. Phys. Lett.*, **85**, 55 (2004).
69. Y. R. Do, H. T. Kwak, and M. M. Sung, *Appl. Phys. Lett.*, **86**, 251912 (2005).
70. Y. K. Lee, J. Y. Cho, C. R. Park, Y. D. Huh, Y. C. Kim, and Y. R. Do, *Electrochem. Solid State Lett.*, **10**, H82 (2007).
71. M. Y. Su, and R. P. Mirin, *Appl. Phys. Lett.*, **89**, 033105 (2006).
72. S. Y. Hsu, M. C. Lee, K. L. Lee, and P. K. Weia, *Appl. Phys. Lett.*, **92**, 013303 (2008).
73. J. P. Kottmann, O. J. F. Martin, D. R. Smith, and S. Schultz, *Chem. Phys. Lett.*, **341**, 1 (2001).

74. K. Tadatomo, H. Okagawa, Y. Ohuchi, T. Tsunekawa, Y. Imada, M. Kato, and T. Taguchi, *Jpn. J. Appl. Phys.*, **40**, L583 (2001).
75. M. Yamada, T. Mitani, Y. Narukawa, S. Shioji, I. Niki, S. Sonobe, K. Deguchi, M. Sano and T. Mukai, *Jpn. J. Appl. Phys.*, **41**, L1431 (2002).
76. D. S. Wu, W. K. Wang, W. C. Shih, R. H. Horng, C. E. Lee, W. Y. Lin, and J. S. Fang, *IEEE Photon. Technol. Lett.*, **17**, 288 (2005).
77. W. K. Wang, D. S. Wu, W. C. Shih, J. S. Fang, C. E. Lee, W. Y. Lin, P. Han, R. H. Horng, T. C. Hsu, T. C. Huo, M. J. Jou, A. Lin and Y. H. Yu, *Jpn. J. Appl. Phys.*, **44**, 2512 (2005).
78. H. S. Cheong, M. G. Na, Y. J. Choi, T. V. Cuong, C. H. Hong, E. K. Suh, B. H. Kong, and H. K. Cho, *J. Crystal Growth*, **298**, 699 (2007).
79. H. Gao, F. Yan, Y. Zhang, J. Li, Y. Zeng, and G. Wang, *J. Appl. Phys.*, **103**, 014314 (2008).
80. S. Möller, and S. R. Forrest, *J. Appl. Phys.*, **91**, 3324 (2002).
81. M. K. Wei, and I. L. Su, *Optics Exp.*, **12**, 5777 (2004).
82. H. Peng, Y. L. Ho, X. J. Yu, M. Wong, and H. S. Kwok, *J. Display Tech.*, **1**, 278 (2005).
83. H. W. Choi, C. Liu, E. Gu, G. McConnell, J. M. Girkin, I. M. Watson, and M. D. Dawson, *Appl. Phys. Lett.*, **84**, 2253 (2004).
84. M. Khizar, Z. Y. Fan, K. H. Kim, J. Y. Lin, and H. X. Jiang, *Appl. Phys. Lett.*, **86**, 173504 (2005).
85. D. Kim, H. Lee, N. Cho, Y. Sung, and G. Yeom, *Jpn. J Appl. Phys.*, **44**, L18 (2005).
86. Y. Sun, and S. R. Forrest, *J. Appl. Phys.*, **100**, 073106 (2006).
87. W. K. Huang, W. S. Wang, H. C. Kan, and F. C. Chen, *Jpn. J. Appl. Phys.*, **45**, L1100 (2006).
88. Y. K. Ee, R. A. Arif, N. Tansu, P. Kumnorkaew, and J. F. Gilchrist, *Appl. Phys. Lett.*, **91**, 221107 (2007).
89. M. K. Lee, and K. K. Kuo, *Electrochem. Solid State Lett.*, **10**, H20 (2007).
90. Y. Sun, and S. R. Forrest, *Nature Photonics*, **2**, 483 (2008).
91. M. K. Lee, C. L. Ho, and C. H. Fan, *Appl. Phys. Lett.*, **92**, 061103 (2008).
92. T. Nakamura, N. Tsutsumi, N. Juni, and H. Fujii, *J. Appl. Phys.*, **97**, 054505 (2005).

93. P. Melpignano, V. Biondo, S. Sinesi, M. T. Gale, S. Westenhöfer, M. Murgia, S. Caria and R. Zamboni, *Appl. Phys. Lett.*, **88**, 153514 (2006).
94. M. W. Chang, H. S. Won, H. Kim, and J. M. Lee, *Jpn. J. Appl. Phys.*, **46**, (2007) 6673.
95. K. Bao, X. N. Kang, B. Zhang, T. Dai, C. Xiong, H. Ji, G. Y. Zhang, and Y. Chen, *IEEE Photon. Technol. Lett.*, **19**, 1840 (2007).
96. T. X. Lee, K. F. Gao, W. T. Chien and C. C. Sun, *Optics Express*, **15**, 6670 (2007).
97. J. M. Steigerwald et al., *Chemical Mechanical Planarization of Microelectronic Materials*, Wiley, New York, 1997.
98. X.-F. Chen, X.-G. Xu, X.-B. Hu, J. Li, S. -Z. Jiang, L. -N. Ning, Y. -M. Wang, and M. -H. Jiang, *Mat. Sc. Engg. B*, **142**, 28 (2007).
99. X.-A Fu, C. A. Zorman, and M. Mehregany, *J. Electrochem. Soc.*, **149**, G643 (2002).
100. P. R. Tavernier, T. Margalith, L. A. Coldren, S. P. DenBaars, and D. R. Clarke, *Electrochem. Solid state lett.*, **5**, G61 (2002).
101. F. Preston, *J. Soc. Glass Technol.*, **11**, 247 (1927).
102. W. J. Patrick, W. L. Guthrie, C. L. Standley, and P. M. Schiabile, *J. Electrochem. Soc.*, **138**, 1778 (1991).
103. O. G. Chekina, and L. M. Keer, *J. Electrochem. Soc.*, **145**, 2100 (1998).
104. R. Saxena, D. G. Thakurta, R. J. Gutmann, and W. N. Gill, *Thin Solid Films*, **449**, 192 (2004).
105. S. R. Runnels, *J. Electrochem. Soc.*, **141**, 1900 (1994).
106. S. -H. Chang, *Microelectronic Engineering*, **82**, 136 (2005).
107. F. T. O'Neill and J. T. Sheridan, *Optik*, **113**, 391 (2002).
108. Z. D. Popovic, R. A. Sprague, and G. A. N. Connell, *Appl. Opt.*, **27**, 1281 (1988).
109. T. Okamoto, T. Mori, T. Karasawa, S. Hayakawa, I. Seo, and H. Sato, *Appl. Opt.*, **38**, 2991 (1999).
110. Y. Ishii, S. Koike, Y. Arai, and Y. Ando, *Jpn. J. Appl. Phys.*, **39**, 1490 (2000).
111. J. Warnock, *J. Electrochem. Soc.*, **138**, 2398 (1991).

## BIOGRAPHICAL SKETCH

Purushottam Kumar was born in 1980, in Ranchi, Jharkhand, India. He graduated from the Indian Institute of Technology (IIT), Kharagpur, India with a bachelor's degree in Metallurgical and Materials Engineering in 2002. He was the recipient of Usha Martin award from IIT Kharagpur and Bengal Ingot Silver medal from the Institute of Indian Foundrymen for his senior year work on "Macro-modeling of Heat Transfer in Shape Castings". He received his Master of Science degree in Metallurgical Engineering from University of Utah, Salt Lake City in 2005. His master's work was on magnetostriction in Nickel-Palladium single crystals and the effect of magnetic field on hydrogen diffusion in these alloys. He moved to University of Florida, Gainesville for his doctoral research under the guidance of Prof. Rajiv Singh in the fall of 2005. His doctoral research was in the area of light out-coupling from solid state lighting devices. He was part of the research group, awarded the 2008 R & D 100 award for development of chemical mechanical polishing slurries for wide band gap semiconductors. He also received the MRS Graduate Student award at 2009 MRS spring meeting. He received his PhD from University of Florida in the spring of 2009.